A cold atoms gravimeter for use in absolute gravity comparisons

by

Lingxiao Zhu

A thesis submitted to
The University of Birmingham
for the degree of
DOCTOR OF PHILOSOPHY

Ultracold Atoms Group
School of Physics and Astronomy
College of Engineering and Physical Sciences
The University of Birmingham

January 2018

Abstract

This thesis describes the construction of high precision absolute gravimeter, aiming at realising a comparison with a state-of-the-art gravimeter. The instrument is based on performing Raman atom interferometry on ensembles of laser-cooled ^{87}Rb atoms in an atomic fountain. The highlight of this work is the demonstration of an IQ modulator based optical single-sideband (OSSB) laser system providing a highly coherent light source. The advantage this brings to atom interferometry is the suppression of the unwanted sidebands, eliminating interference effects, especially the spatially dependent Rabi frequency and the interferometric phase shift. Recently 5×10^6 atoms were launched at a rate of 0.5 Hz with a temperature of 10 μK. After improving the vibration isolation, we have observed interference fringes with a sensitivity of 225 $\mu\text{Gal}/\sqrt{\text{Hz}}$. The preliminary accuracy is estimated to be 218 μGal. A study of systematic noise and bias sources has been undertaken, finding that the limitation of the above performance is the vibration noise and Coriolis effect, respectively. The apparatus has been transported to NERC Space Geodesy Facility in Herstmonceux, where a comparison campaign is in preparation.

Dedicated to my parents and my wife

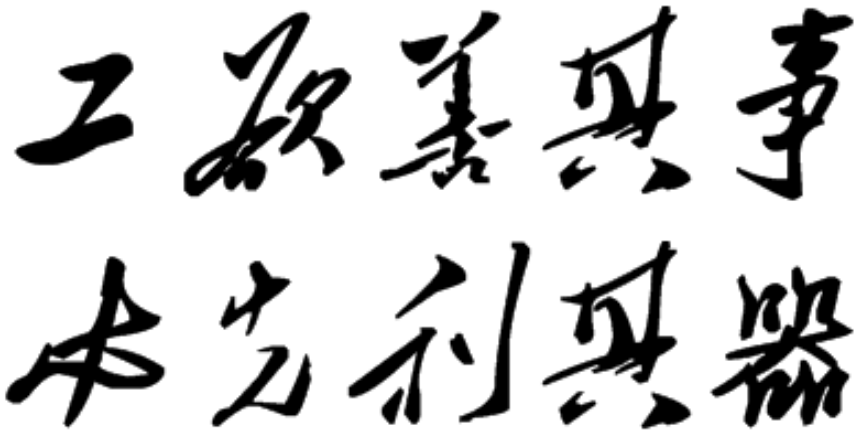

To do a good job,
an artisan needs the best
tools.

ACKNOWLEDGEMENTS

After past a number of defenders, I got to the try line. Touch down successfully! I would like to appreciate a lot of people for the passes in a row before scoring a try. (Rugby rules: https://en.wikipedia.org/wiki/Try).

First of all, thanks to my supervisor, Kai Bongs, who supported, and encouraged me throughout the whole graduate study. I learned so much from his knowledge of science and ambitious ideas.

My gratitude also goes out to Vincent Boyer for his support as my second supervisor and providing clear and insightful explanations to any physics.

I am undoubtedly grateful to Michael Holynski and Yu-Hung Lien for not only leading the development of the experiment, but also kindly guided me how to become a researcher. I am always inspired by their approach to problem-solving.

I am privileged to have worked closely with Tristan Valenzuela, Jonathan Malcolm, Clemens Rammeloo, Andrew Hinton, Alexander Niggebaum and Georgios Voulazeris. Thank you for working alongside me and teaching me some basic experimental skills.

I also want to express heartfelt thanks to Chris Gill, Aisha Kaushik, Anna Kowalczyk, Anthony Rodgers, Alex Wilson, Jonathan Winch, Daniel Benedicto Orenes, Georgina Croft, Luuk Earl, Andrew Lamb, Ben Stray, Wei He, Nadine Meyer, Marisa Perea Ortiz, Simon Plant, Emanuele Rocco, Artur Stabrawa, Dariusz Swierald, Teresa Palubicki and Francesco Colacino. Thank you very much for the important help during my writing of thesis, paper and patent as well as all the joyful time we had at University of Birmingham.

A special thanks to Stephen Brookes and all of the workshop team for their exceptional work building everything that l've asked for without fail and always to extremely high standards.

I also want to express my great appreciation for the staff in NERC Space Geodesy Facility: Victoria Smith, Graham Appleby, Rob Sherwood and Matt Wilkinson. Thank you very much to allow us to work aside the FG5 and support us to operate the comparison campaign.

For all the joyful time in Britain, I give big hugs to my roommates: Biao Yang, Hongchao Liu and Qinghua Guo. Thank you very much for your delicious meal every day. We are the Birmingham F4.

Especially not least of all, I owe my love to my parents and my wife for their constant support and unending encouragement through.

Publications

An overview of the publications during the PhD is given.

Paper

1. L. Zhu et al., Application of optical single-sideband laser in Raman atom interferometry. (Accepted)

2. A. Hinton, L. Zhu et al., A portable magneto-optical trap with prospects for atom interferometry in civil engineering, Philosophical Transactions of the Royal Society of London A: Mathematical, Physical and Engineering Sciences 375 (2099), (2017).

3. K. Bongs, L. Zhu et al., iSense: A Technology Platform for Cold Atom Based Quantum Technologies in Research, Optical Sciences, OSA Technical Digest QTu3B.1, (2014).

Patent Application

L. Zhu, Y. Lien, K. Bongs and M. Holynski, Optical frequency manipulation, GB1712072.6 (2017)

CONTENTS

LIST OF FIGURES

LIST OF TABLES

CHAPTER 1

INTRODUCTION AND MOTIVATION

1.1 Gravity and Gravimetry

1.1.1 Brief History of Gravity

Gravity is a natural phenomenon, which holds us to the surface of the Earth and keeps our atmosphere wrapped around our planet. It is the weakest of the four fundamental interactions in the universe, but acts on all things from subatomic particles to macroscopic masses like planets. Since the ancient times, a lot of scientists have been obsessed by exploring the principle of gravity. One of the most famous anecdotes in the history of science is the story of an apple falling on Isaac Newton's head which inspired him to come up with the theory of gravity. In fact, the history of gravity studies can be traced back to around 350 B.C., when the ancient Greek philosopher Aristotle concluded that the composition of an object determines the degree of a natural desire to fall against the center of the Earth. He believed that heavier objects fall faster. This blurry concept of gravity developed by Aristotle is completely wrong. However it was not until 1632 that Gallileo Galilei brought scientific experiments into the conversation. He discovered that the acceleration of falling bodies is independent of their mass and composition in his famous experiment dropping two spheres from the Leaning Tower of Pisa in 158992 (In 1971, Apollo 15 moonwalker David Scott performed a live demonstration of the experiment by dropping a geologic hammer and a feather at the same time. Eventually both of them hit the lunar surface simultaneously [1]). From then on, people struggled for a philosophical description of the origin of gravity. Initially the mainstream interpretation was governed by the ether theory. This concept was abandoned after Isaac Newton released his universal law of gravity in 1687. In his famous publication *Philosophae Naturalis Principia Mathematica*, Newton proposed mathematically that the force

can be expressed by a terse formalism:

$$F = G\frac{Mm}{r^2} \tag{1.1}$$

where F is the value of the force between two interacting masses M and m at a distance r and G is the gravitational constant. His theory explains the tides and the motions of the planets around the sun. Over a century later, Henry Cavendish obtained the first experimental measurement of gravity between two test masses in the laboratory by using a torsion balance. In his measurement, the density of the Earth was calculated, the value of which is within a few percent of current measurements. However, the fundamental nature of gravity was still mystery. In the early 20th century, Albert Einstein finally came up with an astonishing explanation in his General Theory of Relativity, which claims that gravity is a consequence of the curvature of spacetime, the fabric of the universe. Based on that, his theory succeeded in accurately predicting Mercury's orbit, the gravitational redshift, the existence of black holes, gravitational time delays and gravitational wave. In September 2015, the Advanced LIGO experiment detected a signal formed by a gravitational waves, that appeared to come from the collision of two black holes directly [2]. This achievement marked another milestone in the scientific history of gravity.

1.1.2 Gravity on Earth

On the surface of the Earth, a free-fall mass is accelerated towards the Earth. According to Newton's law of universal gravitation, the acceleration experienced by a mass m_1 is derived

$$g = \frac{F_g}{m_1} = G\frac{m_e}{R^2} \tag{1.2}$$

where F_g is the gravitational force, R and m_e are the radius and mass of the Earth respectively. The symbol g for gravitational acceleration is the so-called 'little g', representing the gravitational force per unit mass. Since the exact gravitational force depends on mass of objects, the gravitational acceleration g is commonly used to specify gravity. We will show later that the explicit value of the 'little g' is dependent upon influences in the local environment.

Gravity Units

In the International System of Units (SI), gravity is measured in N/kg or m/s^2. However, in geophysics for example, the preferred unit is the Gal from the Centimetre-Gram-Seconds (CGS) unit system in honour of Galileo. 1 Gal is a large quantity compared with the terrestrial variations of gravity on the Earth. As a

result, units like mGal and μGal are more frequently adopted. In other fields like the petroleum industry, another unit, known as the gravity unit (g.u.) is also used for gravity measurements [3]. Table 1.1 shows the equivalent units of common parameters used in gravity measurements in both CGS and SI. In this thesis, we specify gravity in μGal or mGal.

Table 1.1: Parameters commonly used in the gravity measurement in equivalent CGS and SI system of units. Other units used in application are also included.

Parameters	CGS	SI	In application
Force of attraction	10^5 dynes	1 kg m/s^2 or newton (N)	
Gravitational acceleration	1 Gal	10^{-2} m/s^2	10^4 g.u.
	1 mGal	10^{-5} m/s^2	10 g.u.
	1 μGal	10^{-8} m/s^2	10^{-2} g.u.
Gravity Gradient	10^{-9} Gal /cm	$10^{-9}/s^2$	1 eotvos (E)

Gravity Variation

The gravity calculated by Equ. 1.2 holds only for homogeneous or radially stratified spherical bodies. In fact, the Earth is more like an oblate ellipsoid with heterogeneous density. The local gravity includes spatial variation due to the size, shape and rotation of the Earth. For example, gravity varies from the equator to the poles of rotation by about 0.5%, changing by slightly more than 5 Gal from approximately 978 Gal at the equator to 983 Gal at the poles. Additionally the cumulative gravitational force of the Moon and Sun on the Earth induces temporal variations of gravity at a given location. The maximum effect of the Moon is approximately $\pm$0.11 mGal and the Sun causes a $\pm$ 0.05 mGal maximum variation, resulting in a maximum total variation within 24 hours of roughly 0.33 mGal [3]. Furthermore the terrestrial terrain also has influences on the gravity. Table. 1.2 lists the sources of the spatial and temporal changes to gravity.

1.2 Gravimeter

High precision gravimeters are essential for gravity research. To some degree, the development of the gravimeter determines our knowledge of the gravity field. Generally gravimeters can be categorised into two basic types: relative and absolute. Relative gravimeters only measure the change in gravity. Compared with absolute gravimeters, relative gravimeters typically have higher sensitive and are easier to make compact in size. However, in order to standardise relative measurements in different locations, relative gravimeters have to be calibrated with a base station. Additionally, due to the instrumental drift, relative gravimeters also require regular calibration.

Table 1.2: Approximate magnitudes of changes in gravitational acceleration at the surface of the Earth from various sources [4, 5].

Source	Magnitude (mGal)
Earth	980000
Latitudinal Variation	5000
Mountain ranges / ocean trenches	200
Mineral anomalies	100
Elevation by 1 m	0.3
Solid earth tides	±0.015
Volcanic/seismic activity	0.2
Sun/Moon Tides	0.1
Mining/large constructions	0.1
Ocean tide loading	±0.01
Ground water level	±0.01
Postglacial rebound	0.01
Polar motion	0.008
Glaciers/Polar ice change	0.005
Atmospheric pressure	0.003-0.02 (0.0003/hPa)
Person at 1m distance	0.0005

The Earth's gravity was first measured using simple pendulums and torsion balances. The pendulum is the most rudimentary of absolute gravimeters, but it is difficult to achieve a better accuracy than mGal. Torsion balances can only be used on relatively flat terrain due to their high sensitivity to irregularities on the ground. Since these instruments also required hours of observations, they were replaced by other instruments during the 20th century [6, 7]. Current commercial gravimeters are summarized below. The terminologies used to assess the performance of the gravimeter are discussed in section 5.1.2 and are consistent throughout the thesis .

1.2.1 Relative Gravimeter

The relative gravimeter is simply a sensitive weighing device, measuring the variations of g. The basic principle is to maintain the test mass suspended in the gravity field and the variations of g are obtained by measuring the counter-reaction force necessary to keep the mass at its equilibrium position. The scaling factor of these instruments needs to be calibrated by an absolute gravimeter.

Typically relative gravimeters are mainly spring-type, meaning the force on a mass due to gravity is balanced by the restoring force of a spring [6]. In the beginning, the gravimeter springs were normally made of metal or fused silica. In 1934, LaCoste made a gravimeter based on a zero length spring, whose force-length graph passes through the origin or, at least, points toward the origin. This gravimeter has an oblique restoring spring which counters the gravity torque. Since these two torques are designed to balance each

other for any angle of the beam in at first, the system will have infinite period. Small change in vertical acceleration (or gravity) will cause a large movement [8]. One of the commercial gravimeters of this type is the gPhoneX gravity meter from Micro-g LaCoste [9]. Another widely used spring-type gravimeter is the CG5 Autograv from Scintrex (the CG-6 Autograv is the latest vesion), which operates by electro-statically stabilising a proof mass attached to a fused quartz spring [10]. The gravity variations are translated into a voltage change of the capacitor plates that keep the mass at the null position. However, the above spring-type gravimeters have fundamental problems such as the elastic variability of the spring, thermal noise in the spring and mass loss from the test-mass, which result in the need for regular calibration. The superconducting gravimeter is a new spring-type gravimeter which has small drift. The test mass is a metallic sphere made from or coated with a layer of superconducting metal, which is levitated by a magnetic field generated by current flowing in a superconducting coil cooled to 4K. Thus variations in gravitational or inertial forces are proportional to the change in current needed to balance the test mass at the reference position. [11, 12]. The iGrav superconducting gravimeter from GWR instruments achieves one of the best sensitivities and long-term stability [13]. Therefore the iGrav is often used to compare and calibrate other gravimeters [14, 15]. The drawback is the gravimeter is hard to transport, bulky and time consuming to set up at new sites. Table 1.3 shows specifications of current commercial relative gravimeters.

Recently new technology has been employed in lab prototype systems to make gravimeters more compact. One of them is the relative gravimeter based on microelectromechanical systems (MEMS) technology. The reported sensitivity is 40 μ Gal/$\sqrt{\text{Hz}}$ with a stability capable of measuring the Earth tide [16]. Due to the compact size and low cost, this MEMS gravimeter is promising for gravimetry in the future. However the significant drifts are a major issue for recent applications.

Table 1.3: Comparison of commercial relative gravimeters with their reported specifications.

Representative	CG5 & CG6 Scintrex	gPhoneX Gravity Meter	iGrav
Principle	Fused quartz spring	Zero-length spring tension	Superconducting
Measurement Frequency	6 Hz		1 Hz
Noise		0.1 to 0.3 μGal/$\sqrt{Hz}$	0.3 μGal/$\sqrt{Hz}$
Precision		1 μGal	
Resolution	1 μGal	0.1 μGal	0.001 μGal
Residual Drift	20 μGal/day	1500 μGal/month	0.5 μGal/month
Range	8000 mGal	7000 mGal	
Power Consumption	4.5W	300 W	1.3 kW
Mass	8.9	58 kg	40 kg
Reference	Datasheet [17]	Datasheet [18]	Datasheet [19]

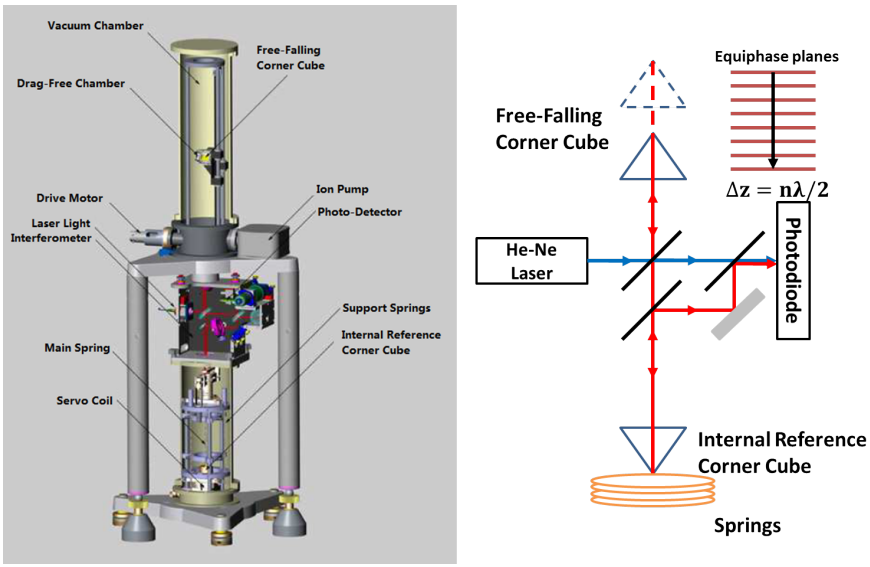

Figure 1.1: Schematic of the FG5 gravimeter.

1.2.2 Absolute Gravimeter

The absolute gravimeters currently used follow the free trajectory in vacuum of a test mass, which then defines an inertial reference. The determination of absolute gravity is based on the measurement of the fundamental acceleration quantities distance and time. The mass may be either launched or catapulted. In order to measure the distance precisely, laser interferometry has been used, providing a transportable and stable standard of length.

According to the ballistic trajectory, the free-fall type gravimeter can be sorted into two types: direct free-fall and symmetrical rise-and-fall. The advantage of the direct free-fall is its greater mechanical simplicity which contributes to a high data rate, while the symmetrical rise-and-fall method is less sensitive to some systematic noise [20]. One of the most representative absolute gravimeters based on direct free-fall is the FG5 from Micro-g LaCoste [21]. The basic principle of this instrument is depicted in Fig. 1.1. Here a Michelson interferometer whose mirrors are corner cubes is used to measure the distance traveled by the test mass during a time T. One of the mirrors is fixed and set as a reference. The other corner cube moves vertically in the gravity field. The counting of the optical interference fringes passing through the free movement of the second corner cube gives a measurement of g. The optical fringes provide a very accurate distance measurement based on absolute wavelength standards, and the accurate and precise timing of the occurrence of these optical fringes are based on an atomic rubidium clock. [22, 23]. In this way, distance and time are directly tied to time and length SI units. Another comparable absolute gravimeter is IMGC, which is based

on the symmetrical rise-and-fall method. This gravimeter mostly works on the same principle as FG5, except that the beam splitter and the mirrors are combined into a monolithic plane-parallel glass plate [24].

These instruments have a very good accuracy, at the level of a few μGal. In a very calm environment, they have a sensitivity of the order of a few μGal and a good long-term stability which makes it possible to achieve sub-μGal resolutions after several hours of integration. However, its mechanical structure for repeated free-falling prevents its use on a mobile platform and limits its cycle time (this is limited by the damping time of the mechanical vibrations generated by the corner cube after each fall). The preferred drop rate of the FG5 is 1 drop every 15 s [25]. In addition, the performance of corner cube gravimeters is subject to long-term mechanical wear of moving parts.

Instead of a macroscopic mass, atoms have been found to be a good candidate to act as the test mass in free-fall gravimeters. A cold atom gravimeter was first demonstrated by Mark Kasevich and Steven Chu in 1991, with a resolution of 30 μGal after 2000 s of integration time [26]. From then on, various institutes around the world have been studying the sensitivity and accuracy of these instruments and are developing their own laboratory prototypes. Due to the improvements in compactness and robustness, atomic gravimeters are promising for field applications. Recently, both AOSense and Muquans have developed commercial gravimeters based on atom interferometry. Compared with corner cube type, atomic gravimeters can not only become more compact but can also reach measurement rates comparable to relative gravimeters. Additionally, the absence of any moving mechanical parts makes these instruments better suited for field applications. Table 1.4 shows specifications of current commercial absolute gravimeters.

Table 1.4: Comparison of commercial absolute gravimeters with their reported specifications.

Specifications	FG5 & FG5X	A10	AQG
Principle	Free-fall corner cube	Free-fall corner cube	Atom interferometry
Accuracy	2 μGal	10 μGal	A few μGal
Precision	15 μGal/$\sqrt{Hz}$	100 μGal /$\sqrt{Hz}$	50 μGal /$\sqrt{Hz}$
Long-term Stability			1 μGal
Measurement Rate	few seconds		2 Hz
Power Consumption	500 W	300 W	300 W
Mass	320 kg	105 kg	100 kg
Refereence	[27]	[28]	[29]

1.2.3 Atom Interferometry Gravimeter

As a stepping-stone to understand the mechanism of the atom interferometry gravimeter, the basic working principle of an atom interferometer is explained here. In fact, there are various approaches to atom

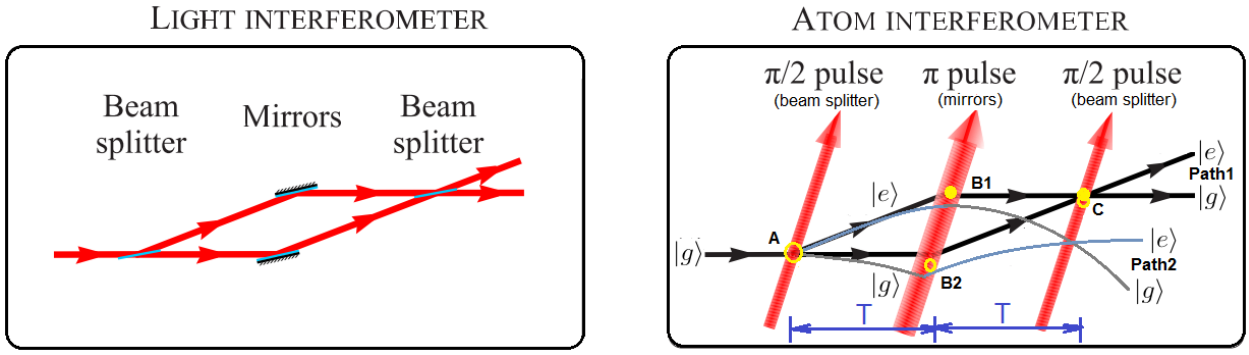

Figure 1.2: The light interferometer (left) and atom interferometer (right) in Mach-Zehnder configuration. Path1 (straight lines) and Path2 (curved lines) in the atom interferometry represent the trajectories of the atom clouds with and without the homogeneous gravity. Modified from [32].

interferometry [30]. Current atom based gravity measurements mainly adopt the scheme of light-pulse atom interferometry [26]. The detailed theory can be found in chapter 2. The construction of an atom interferometer is based on a Mach-Zehnder interferometer as shown in Fig. 1.2. In an optical interferometer, a light beam is first split into two parts by a beamsplitter, redirected by mirrors, and then recombined by a second beamsplitter. Measurement of the intensity at the output ports makes it possible to acquire information on the phase shift accumulated between the arms of the interferometer during propagation [31]. In an atom interferometer, the splitting, reflection and recombining are realised by Raman transitions driven by laser pulses [26, 25].

Principle

A resonant laser can drive the transition of a two level atom, from ground state $|g\rangle$ to excited state $|e\rangle$. The transition probability oscillates sinusoidally as a function of the laser duration, which is called Rabi oscillation. Assume a group of atoms are all in state $|g\rangle$ initially, we denominate a laser pulse which puts the atoms into a superposition state of half $|g\rangle$ and half $|e\rangle$ as a $\pi/2$ pulse while a laser pulse which completely flips the state of the atoms is called a π pulse. In the $\pi/2$-π-$\pi/2$ type atom interferometer, the first $\pi/2$ pulse puts half of the atomic probability distribution into the excited state, creating a superposition. Due to momentum conservation, atoms absorbing or emitting a photon also receive a momentum impulse. Consequently atoms promoted to the excited state split spatially from the ground state atoms. The first $\pi/2$ pulse works as a splitter, introducing a velocity difference $\mathbf{v}=\hbar\mathbf{k}/\mathrm{m}$ between the two states, where $\mathbf{k}$ is the wavevector of the laser and m is the mass of the atom. After a free evolution time T, a π pulse flips both the internal and external state of the two atom clouds, which acts as a mirror and redirects the atoms' propagation. After

a second free evolution T, the clouds overlap. A third $\pi/2$ pulse mixes the two clouds together. Without any perturbation in the paths, the population distribution between the two states is equal at the output. Otherwise the probability of finding the atom in state $|e\rangle$ depends on the dephasing in the following way $P = \frac{1}{2}(1 - \cos(\Delta\phi))$, where $\Delta\phi$ is the phase difference acquired during the interrogation time. In atom interferometer, $\Delta\phi = \mathbf{k} \cdot \Delta\mathbf{z} + \int_0^T \delta(t)dt$, where $\Delta\mathbf{z}$ is the distance of atom moving and $\delta(t)$ is the laser detuning during the evolution time T. When atoms free fall in the gravity field, the interferometer phase is given by:

$$\Delta\phi = kgT^2 \tag{1.3}$$

where g is the local gravity and we assume that the laser frequency exactly match the atomic resonance. In fact, the frequency detuing can be generated by the Doppler effect during the atom free falling. In order to compensate this phase shift, the frequency of the laser is chirped during the interferometry sequence. Thus the interferometer phase is modified by $\Delta\phi = kgT^2 - \alpha T^2$, where α is the chirp rate of the laser. Gravity can be extracted by measuring the chirp rate α_0 precisely, which cancels the Doppler shift as $kgT^2 - \alpha_0 T^2 = 0$. The sensivity is proportional to T^2 and is further enhanced by many atoms free-falling simultaneously, which reduces the quantum shot noise limit[33]. Consider that the interrogation time 2T is 1 s and the transition linewidth is 1 Hz, the gravity induced Doppler shift is about 10 MHz in this case, which is sufficient to spoil the population transfer between the states. With 10^6 atoms in the sequence, a 10^{-9} fractional change in the acceleration can be detected. The best sensitivity reported is 4.2 μGal/$\sqrt{\text{Hz}}$ [34] (2T=600 ms). Table 1.5 shows the reported specifications of the atom interferometry gravimeters in labs worldwide.

State-of-the-art

In the past decades, efforts have been consistently made to improve the performance of the atom interferometer as well as span its application into other fields. High sensitivity has been demonstrated by long baseline [43, 44, 45], large momentum transfter [46, 47] and novel schemes [48, 49]. In order to increase the sensitivity further, atom interferometry in microgravity has been proposed, in particular, for fundamental tests such as of the validity of the Einstein's equivalence principle [50, 51, 52, 53]. Some demonstrations have been made on the free fall tower [54, 55], the moving elevator [38], Zero-G aircraft [56] and even on a sounding rocket [57]. The systematic errors of atom interferometers have also been examined in detail [58]. Comparison with other commerical absolute gravimeters indicates the advantages of atom interferometry gravimeters [59, 37, 41]. Benefit from the development of the atomic clock, new atomic species like strontium have been demonstrated for gravity measurement [60]. For the field applications, a lot of effort has been directed towards improving

the compactness, robustness and transportability[61]. Projects like iSense [62], CAG [63] and QG-1[64] have paved the road for the realisation of a mobile, non-laboratory-based sensor. Recently commercial products like AQG and AOSence are in competition against other absolute gravimeters currently on the market.

In addition to gravity, atom interferometers have demonstrated the highest precision in the laboratory for gravity gradients [65] and rotation [66, 67]. The unprecedented sensitivity and practically drift-free atomic sensors are very interesting for applications, e.g. in oil exploration, inertial navigation [68, 69] or geodesy [70]. In fundamental science, atom interferometers have been used to determine the Newtonian gravitational constant [71, 72], fine structure constant [73], SI unit of mass [74] and test the weak equivalence principle [75]. Future applications may include detecting gravitational waves [76] or dark energy [77].

1.3 Organisation of the Thesis

This thesis presents the construction of a reference platform under the UK National Quantum Technology Hub (QT Hub) in Sensors and Metrology. The aim of this work within the hub is to build a high precision gravity reference as a transportable calibration platform. The first step is to build a gravimeter comparable with different state-of-the-art gravimeters. In this experiment, it is the first time that Raman light for atom interferometry has been generated using a scheme based on single sideband modulation. The intrinsic phase coherence of the phase modulated laser significantly reduces the interferometer phase noise induced by the laser phase noise. The thesis is organised as below:

Chapter 2: The theory of atom interferometry is presented in detail. Special emphasis is given to the derivation of the ratio in the state populations after a MachZehnder type sequence of Raman pulses and their application in gravity sensing. Then the sensitivity function is introduced to estimate the impact of noise sources on the gravity measurement. This tool is required in chapter 5 to characterise the performance of the experiment.

Chapter 3: This chapter mainly focuses on the construction of an atomic fountain. The science chamber is inherited from another project 'GGtop'. The former PhD students on the GGtop project, Alex Niggebaum and Andrew Hinton, realized the mageto-optic trap (MOT) and achieved Ramesy fringes [78, 79]. The work of the author starts from the optimisation of the MOT. In order to improve the robustness and stability of the experiment, important modifications have been developed within this thesis, such as building free space optics and changing control software. The chapter also describes how the moving molasses technique is used to launch atoms upwards into the interferometry region.

Chapter 4: The realisation of the atom interferometer is presented. Special emphasis is given to the

Raman laser scheme which is based on single sideband modulation. Some key specifications of the Raman laser system are measured. In addition, the advantage of our Raman laser system is demonstrated experimentally.

Chapter 5: In order to understand the limitation of the system, the noise and systematic errors of the atom interferometer are analysed. The budget of the sensitivity of the gravimeter is calculated and the accuracy of the gravimeter is evaluated.

Chapter 6: The entire system has been transported to the NERC space geodesy facility at Herstmonceux for comparison with FG5 and CG5. New mechanical frames were built, which allowed the experiment to be taken out of the lab. The process of packing, loading and unloading are summarized. Then the gravity measurement protocol in the future comparison is presented.

Chapter 7: This chapter concludes with an outlook on future improvements.

Table 1.5: Comparison of atom interferometer gravimeters with their reported specifications.

Institute	Stanford	LNE-SYRTE	ONERA	ANU	LENS	HU Berlin	ZUT	HUST
Sensitivity (μGal/$\sqrt{Hz}$)	8	60	42	60	700	9.6	100	4.2
Resolution (μGal)		1.9	2.7	13	3.9 at 50000 s	0.05	5.7	0.5
Accuracy (μ)Gal		5.2	25			3.9		
Repetition (Hz)		3			0.5		2.2	1
Interrogation Time (ms)	200		48	60	160	260	120	200
Reference	[35]	[36, 37]	[38]	[39]	[40]	[41]	[42]	[34]

CHAPTER 2

THEORY

Matter wave interferometers can be realised in several ways. We present here the operation of an atom interferometer using stimulated Raman transitions. This method enables using large momentum recoil to efficiently separate, deflect and recombine the atomic wavepackets while allowing one to readout the interferometer using the populations of atomic states.

In this chapter we firstly present the principle of stimulated Raman transitions on a simplified three-level atom. The result is used to perform a $\pi/2 - \pi - \pi/2$ interferometer sequence. The important equations for extracting the gravity value from the measured phase are derived. Finally, the sensitivity function is introduced as a tool to evalute the impact of various noise sources upon the interferometer phase noise. Its application in calculating the interferometer noise induced by the laser phase noise and vibrational noise is introduced. These derivations closely follow the contents in the literature [30] and also refer to theses [80, 81].

2.1 Stimulated Raman Transitions

The two hyperfine ground states can be coupled by stimulated Raman transitions, which are a two-photon process. Assume an atom with two ground states $|g\rangle$ and $|e\rangle$ and an intermediate excited state $|i\rangle$ as in Fig. 2.1. The splitting of the two ground states is equal to ω_{eg}. One pair of counter-propagating lasers with optical frequencies ω_1 and ω_2 are used to drive the stimulated Raman transition. When the atom absorbs or emits one photon, the external state of the atom is also changed by one photon momenta. Due to the coupling of the internal and external states, we describe the atomic state as a tensor product of two Hilbert

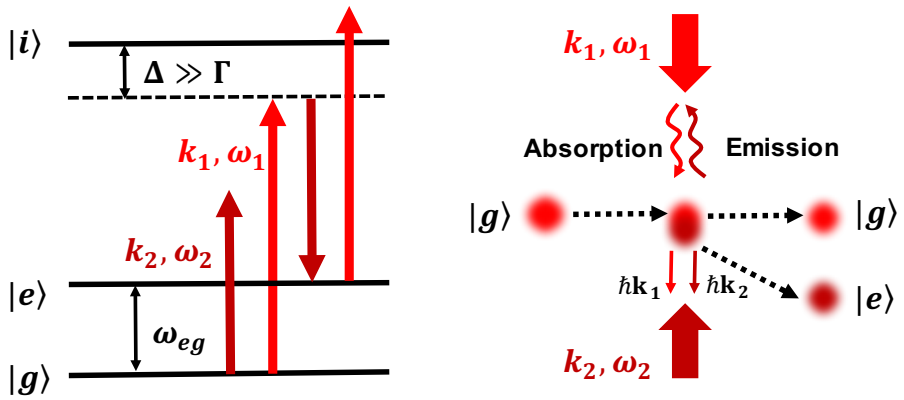

Figure 2.1: Left: Λ type Raman transition in three-level atom. The detuning Δ to the excited state $|i\rangle$ is much larger than the natural linewidth Γ. Right: diagram of the momentum transfer and spatially seperation of atoms performed by a stimulated Raman transition.

spaces in the rest of the chapter:

$$\begin{aligned} |g, \mathbf{p}_g\rangle &= |g\rangle \otimes |\mathbf{p}\rangle \\ |e, \mathbf{p}_e\rangle &= |e\rangle \otimes |\mathbf{p} + \hbar\mathbf{k}_{eff}\rangle \\ |i, \mathbf{p}_{ij}\rangle &= |i\rangle \otimes |\mathbf{p}_{ij}\rangle \end{aligned} \tag{2.1}$$

where $\mathbf{p}$ is the momentum of the atom in state $|g\rangle$, $\hbar\mathbf{k}_{eff}$ is the transferred momentum by stimulated Raman transition with the effective wavevector $\mathbf{k}_{eff} = \mathbf{k}_1 - \mathbf{k}_2$. Since the intermediate state can couple to two frequencies and two ground states, three different momenta are given rise to, which are $\mathbf{p}_{i1} = \mathbf{p} + \hbar\mathbf{k}_1$,$\mathbf{p}_{i2} = \mathbf{p} + \hbar\mathbf{k}_2$ and $\mathbf{p}_{i3} = \mathbf{p} + \hbar(\mathbf{k}_{eff} + \mathbf{k}_1)$. These new intermediate states $|i, \mathbf{p}_{ij}\rangle$ are indicated by the index j. We will show later that these intermediate states can be eliminated adiabatically in case of large detuning ($\Delta \gg \Gamma$).

Resonance Condition

In order to drive the Raman transition effectively, the two-photon resonance condition must be satisfied. The exact resonance condition can be derived by the conservation of energy between the initial and final states:

$$\hbar\omega_1 + \hbar\omega_g + \frac{\mathbf{p}^2}{2m} = \hbar\omega_2 + \hbar\omega_e + \frac{(\mathbf{p} + \hbar\mathbf{k}_{eff})^2}{2m} \tag{2.2}$$

which is rearranged as the frequency difference of the laser:

$$\begin{aligned}\omega_1 - \omega_2 &= \omega_e - \omega_g + \frac{\mathbf{p}\cdot\mathbf{k}_{eff}}{m} + \frac{\hbar\mathbf{k}_{eff}^2}{2m} \\ &= \omega_{eg} + \omega_D + \omega_{rec}\end{aligned} \tag{2.3}$$

where ω_{eg} is the hyperfine state splitting, ω_D is the Doppler shift and ω_{rec} is the recoil shift. Due to the Doppler shift term, only atoms in a limited range of velocities can contribute to the Raman transition. This is the basic principle of how we perform velocity selection and cool the atoms further, prior the atom interferometer (see section 4.4.2).

Time Evolution

In the interaction between the atom and laser, the time evolution of an arbitrary atom state can be written as a linear superposition of the basis states in Equ. 2.1:

$$|\Psi(t)\rangle = a_g(t)|g,\mathbf{p}_g\rangle + a_e(t)|e,\mathbf{p}_e\rangle + a_{i1}(t)|i,\mathbf{p}_{i1}\rangle + a_{i2}(t)|i,\mathbf{p}_{i2}\rangle + a_{i3}(t)|i,\mathbf{p}_{i3}\rangle \tag{2.4}$$

where $a_n(t)$ are time-dependent coefficients. Assume the electromagnetic field is:

$$\mathbf{E}(\mathbf{r},t) = \mathbf{E}_1\cos(\mathbf{k}_1\cdot\mathbf{r} - \omega_1 t + \phi_1) + \mathbf{E}_2\cos(\mathbf{k}_2\cdot\mathbf{r} - \omega_2 t + \phi_2) \tag{2.5}$$

where $\phi_{1,2}$ are the initial phases. In the absence of spontaneous emission ($\Delta \gg \Gamma$), the Hamiltonian operator of the three level system coupled to an electromagnetic field is:

$$\hat{H} = \frac{\hat{\mathbf{P}}^2}{2m} + \hbar\omega_g|g\rangle\langle g| + \hbar\omega_e|e\rangle\langle e| + \hbar\omega_i|i\rangle\langle i| - \hat{\mathbf{d}}\cdot\mathbf{E} \tag{2.6}$$

where $\hat{\mathbf{p}}$ is the momentum operator and $\hat{\mathbf{d}}$ is the electric dipole moment operator. The last term $V = -\mathbf{d}\cdot\mathbf{E}$ is the electric dipole coupling term using the electric dipole approximation. In order to eliminate the time-dependent factors, the coefficients $a_n(t)$ are separated into a fast oscillation term and a slowly varying part as:

$$a_n(t) = c_k(t)e^{-i(\omega_k + \frac{|\mathbf{p}_k|^2}{2m\hbar})t} \tag{2.7}$$

Inserting the wavefunction Equ. 2.4 and the Hamiltonian Equ. 2.6 with new variables 2.7 into the *Schrödinger* equation:

$$i\hbar\frac{d}{dt}|\Psi(t)\rangle = \hat{H}|\Psi(t)\rangle \tag{2.8}$$

it gives rise to new coefficients:

$$\begin{aligned}
i\dot{c}_g(t) =& \frac{\Omega_{g1}^*}{2}e^{i\Delta t - i\phi_1}c_{i1}(t) + \frac{\Omega_{g2}^*}{2}e^{i(\Omega-\delta-\omega_{eg}+\delta_2)t-i\phi_2}c_{i2}(t)\\
i\dot{c}_e(t) =& \frac{\Omega_{e1}^*}{2}e^{i(\Delta+\omega_{eg}-\delta_3)t-i\phi_1}c_{i3}(t) + \frac{\Omega_{e2}^*}{2}e^{i(\Delta-\delta)t-i\phi_2}c_{i1}(t)\\
i\dot{c}_{i1}(t) =& \frac{\Omega_{g1}}{2}e^{-i\Delta t+i\phi_1}c_g(t) + \frac{\Omega_{e2}}{2}e^{i(\Delta-\delta)t+i\phi_2}c_e(t)\\
i\dot{c}_{i2}(t) =& \frac{\Omega_{g2}}{2}e^{-i(\Delta-\delta-\omega_{eg}+\delta_2)t+i\phi_2}c_g(t)\\
i\dot{c}_{i3}(t) =& \frac{\Omega_{e1}}{2}e^{-i(\Delta+\omega_{eg}-\delta_3)t+i\phi_1}c_e(t)
\end{aligned} \tag{2.9}$$

where Ω_{jk}, Δ,δ,δ_2 and δ_3 are defined as below:

$$\Omega_{jk} \equiv -\frac{\langle i|\mathbf{d}\cdot\mathbf{E}_k|j\rangle}{\hbar} \tag{2.10}$$

$$\Delta \equiv \omega_1 - (\omega_i - \omega_g + \frac{\mathbf{p}\cdot\mathbf{k}_1}{m} + \frac{\hbar|\mathbf{k}_1|^2}{2m}) \tag{2.11}$$

$$\delta \equiv \omega_1 - \omega_2 - (\omega_{eg} + \frac{\mathbf{p}\cdot\mathbf{k}_{eff}}{m} + \frac{\hbar|\mathbf{k}_{eff}|^2}{2m}) \tag{2.12}$$

$$\delta_2 \equiv \frac{\hbar\mathbf{k}_2\cdot\mathbf{k}_{eff}}{m}, \delta_3 \equiv \frac{\hbar\mathbf{k}_1\cdot\mathbf{k}_{eff}}{m} \tag{2.13}$$

In the above derivation, we neglect the fast rotating terms at optical frequencies $\omega_i - \omega_g + \omega_1$ (rotating wave approximation (RWA)). In practice, the detuning Δ can deliberately be set to a value much larger than the Rabi frequency Ω_{jk}. Therefore the coefficients $c_g(t)$ and $c_e(t)$ vary much more slowly than explicitly time-dependent terms. We can regard the coefficients $c_g(t)$ and $c_e(t)$ as constant in Equ. 2.9. Hence the atomic system is analogous to a two-level system via the process of adiabatic elimination of the excited state coefficients. In the typical experimental setting where $|\Delta| \gg |\delta|, |\delta_2|, |\delta_3|$, the new coefficients are given by:

$$\begin{aligned}
\dot{c}_e(t) &= -i\left(\Omega_e^{AC}c_e(t) + \frac{\Omega_{eff}}{2}e^{-i(\delta t+\phi_{eff})}c_g(t)\right)\\
\dot{c}_g(t) &= -i\left(\Omega_g^{AC}c_g(t) + \frac{\Omega_{eff}^*}{2}e^{i(\delta t+\phi_{eff})}c_e(t)\right)
\end{aligned} \tag{2.14}$$

where we define the light shift of the two levels Ω_g^{AC} and Ω_e^{AC}, the effective phase between the two light fields ϕ_{eff} and the coupling frequency between the two ground states Ω_{eff} as

$$\Omega_g^{AC} = \frac{\mid \Omega_{g,1} \mid^2}{4\Delta} + \frac{\mid \Omega_{g,2} \mid^2}{4(\Delta - \omega_{eg})}, \Omega_e^{AC} = \frac{\mid \Omega_{e,1} \mid^2}{4(\Delta + \omega_{eg})} + \frac{\mid \Omega_{e,2} \mid^2}{4\Delta} \tag{2.15}$$

$$\Omega_{g,n} = -\frac{\langle i|\mathbf{d}\cdot\mathbf{E}_n|g\rangle}{\hbar}, \Omega_{e,n} = -\frac{\langle i|\mathbf{d}\cdot\mathbf{E}_n|e\rangle}{\hbar} \tag{2.16}$$

$$\phi_{eff} = \phi_1 - \phi_2 \tag{2.17}$$

$$\Omega_{eff} = \frac{\Omega_e^* \Omega_g}{2\Delta} e^{i(\phi_1 - \phi_2)} \tag{2.18}$$

Equ. 2.14 can be resolved by following the solution in nuclear magnetic resonance spectroscopy [82]. The evolution of these coefficients with time in the rotating frame is given by:

$$\begin{aligned}
c_g(t_0+\tau) =& e^{-i(\Omega^{AC}-\delta)\tau/2} \\
&\times [(cos(\frac{\Omega_r\tau}{2}) + \frac{i(\delta^{AC}-\delta)}{\Omega_r} sin(\frac{\Omega_r\tau}{2}))c_g(t_0) - i\frac{\Omega_{eff}}{\Omega_r} sin(\frac{\Omega_r\tau}{2}) e^{i(\omega_{eff}t_0+\phi_{eff})} c_e(t_0))] \\
c_e(t_0+\tau) =& e^{-i(\Omega^{AC}+\delta)\tau/2} \\
&\times [(cos(\frac{\Omega_r\tau}{2}) - \frac{i(\delta^{AC}-\delta)}{\Omega_r} sin(\frac{\Omega_r\tau}{2}))c_e(t_0) - i\frac{\Omega_{eff}}{\Omega_r} sin(\frac{\Omega_r\tau}{2}) e^{-i(\omega_{eff}t_0+\phi_{eff})} c_g(t_0))]
\end{aligned} \tag{2.19}$$

where the off-resonant Rabi frequency Ω_r is written as $\Omega_r = \sqrt{\Omega_{eff}^2 + (\delta - \delta^{AC})^2}$ and $\delta^{AC} = (\Omega_e^{AC} - \Omega_g^{AC})$ is the differential AC Stark shift of the two levels. The results, transferred to the non-rotating frame, are expressed by:

$$\begin{aligned}
a_g(t_0+\tau) =& e^{-i(\Omega^{AC}-\delta+2\omega_g^{'})\tau/2} \\
&\times [(cos(\frac{\Omega_r\tau}{2}) + \frac{i(\delta^{AC}-\delta)}{\Omega_r} sin(\frac{\Omega_r\tau}{2}))a_g(t_0) - i\frac{\Omega_{eff}}{\Omega_r} sin(\frac{\Omega_r\tau}{2}) e^{i(\omega_{eff}t_0+\phi_{eff})} a_e(t_0))] \\
a_e(t_0+\tau) =& e^{-i(\Omega^{AC}+\delta+2\omega_e^{'})\tau/2} \\
&\times [(cos(\frac{\Omega_r\tau}{2}) - \frac{i(\delta^{AC}-\delta)}{\Omega_r} sin(\frac{\Omega_r\tau}{2}))a_e(t_0) - i\frac{\Omega_{eff}}{\Omega_r} sin(\frac{\Omega_r\tau}{2}) e^{-i(\omega_{eff}t_0+\phi_{eff})} a_g(t_0))]
\end{aligned} \tag{2.20}$$

where $\omega_{eff} = \omega_1 - \omega_2$ is the effective frequency

$$\omega_g^{'} = \omega_g + \frac{|\mathbf{p}|^2}{2m\hbar}, \omega_e^{'} = \omega_e + \frac{|\mathbf{p} + 2\hbar\mathbf{k}_{eff}|^2}{2m\hbar} \tag{2.21}$$

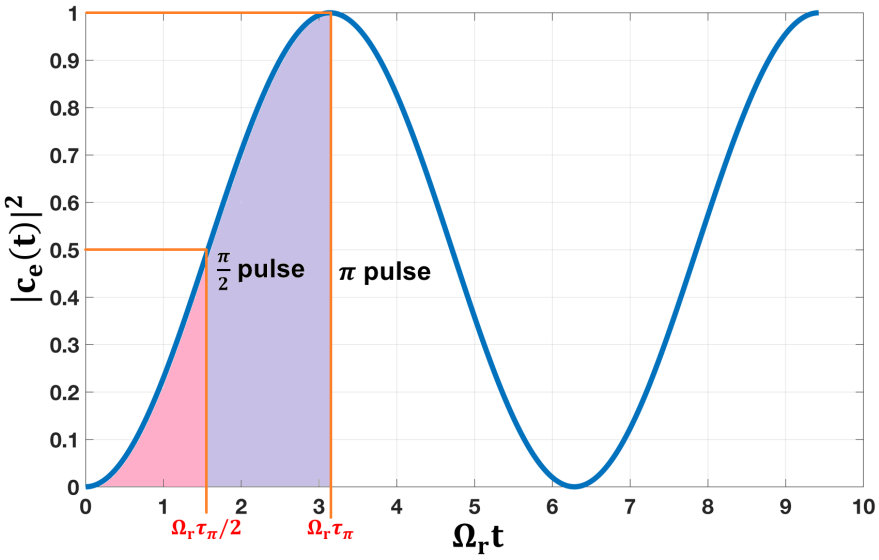

Figure 2.2: Schematic diagram of a Rabi Oscillation. The pulse indicated by $\pi/2$ pulse transfers half of the atoms to the state $|e\rangle$ while the π pulse transfers all the atoms to state $|e\rangle$.

$\pi/2$ and π Transitions

If we consider that the atom is initially in the state $|g, \mathbf{p}\rangle$ such that $c_g(t_0) = 1$ and $c_e(t_0) = 0$. After the resonant Raman transition with AC Stark shift eliminated (δ=0 and δ^{AC}=0), the temporal evolution of the atomic system in the rotating frame is given by:

$$c_e(\tau) = -i\sin\frac{\Omega_{eff}\tau}{2}e^{-i\phi_{eff}-i\frac{\Omega^{AC}\tau}{2}} \tag{2.22}$$

Thus the internal state of the atom changes according to the product of the effective Rabi frequency Ω_{eff} and pulse length τ. The population probability in both the rotating and non-rotating frame is expressed as:

$$\boxed{|c_e|^2 = |a_e|^2 = \frac{1}{2}(1 - \cos(\Omega_{eff}\tau))} \tag{2.23}$$

We depict the variation of the population probability in Fig. 2.2. Excited by a pulse with duration satisfying $\Omega_{eff}\tau$=$\pi/2$, the distribution of populations is equal. The wavefunction is written as:

$$|\Phi(\tau)\rangle = \frac{1}{\sqrt{2}}(|g, \mathbf{p}\rangle + (|e, \mathbf{p} + \hbar\mathbf{k}_{eff}\rangle) \tag{2.24}$$

where atoms in state $|e\rangle$ move away from the other in $|g\rangle$ due to their momentum divergence $\Delta\mathbf{p} = \hbar\mathbf{k}_{eff}$. Such a Raman transition, called $\pi/2$, is the atomic equivalent of a 50/50 splitter in optics. Similarly, a transition π designates a pulse whose duration is twice that of a $\pi/2$ pulse. In this case, population transfer is complete, and all of the atoms transition from state $|g\rangle$ to $|e\rangle$. These two types of pulses are the tools needed to produce an atom interferometer.

Phase Shift

According to Equ. 2.19, Raman transitions also attach an additional phase onto the states. In a sequence of Raman pulses, the final population is changed by the accumulated phases. Consider the general case of a Raman pulse with length τ. The phase shift depends on the initial and final state. Table 2.1 lists the phase shift contribution of one Raman transition combining different initial and final states with

$$\theta^0 = \cos(\frac{\Omega_r\tau}{2}) + \frac{i(\theta - \theta^{AC})}{\Omega_r}\sin(\frac{\Omega_r\tau}{2}) \tag{2.25}$$

Table 2.1: Phase shift contribution terms induced by Raman pulses of length τ to different combinations of initial and final states. Cited from [83]

Transition	Phase Shift
$\|g,\mathbf{p}\rangle \to \|e,\mathbf{p}\rangle$	$(-\Omega_e^{AC} - \Omega_g^{AC} + \delta)\frac{\tau}{2} - \theta^0$
$\|g,\mathbf{p}\rangle \to \|e,\mathbf{p}+\hbar\mathbf{k}_{eff}\rangle$	$(-\Omega_e^{AC} - \Omega_g^{AC} - \delta)\frac{\tau}{2} - \frac{\pi}{2} - \theta t_0 - \phi_{eff}$
$\|e,\mathbf{p}+\hbar\mathbf{k}_{eff}\rangle \to \|e,\mathbf{p}+\hbar\mathbf{k}_{eff}\rangle$	$(-\Omega_e^{AC} - \Omega_g^{AC} - \delta)\frac{\tau}{2} + \theta^0$
$\|e,\mathbf{p}+\hbar\mathbf{k}_{eff}\rangle \to \|g,\mathbf{p}\rangle$	$(-\Omega_e^{AC} - \Omega_g^{AC} + \delta)\frac{\tau}{2} - \frac{\pi}{2} + \theta t_0 + \phi_{eff}$

2.2 Atom Interferometry

2.2.1 Mach-Zehnder atom interferometer

The Mach-Zehnder atom interferometer consists of a sequence of three Raman pulses $\pi/2 - \pi - \pi/2$ separated by time T. As shown in Fig. 2.3, the first $\pi/2$ pulse acts as a beam splitter, putting the atoms into a coherent superposition of $|g,\mathbf{p}\rangle$ and $|e,\mathbf{p}+\hbar\mathbf{k}_{eff}\rangle$. The two wave packets then spatially separate due to the photon recoil transferred during the first pulse. After a free evolution for time T, a π redirects them towards each other, inverting the internal states and velocities. Thus the two wave packets meet after a second interval T. A last $\pi/2$ pulse allows them to interfere.

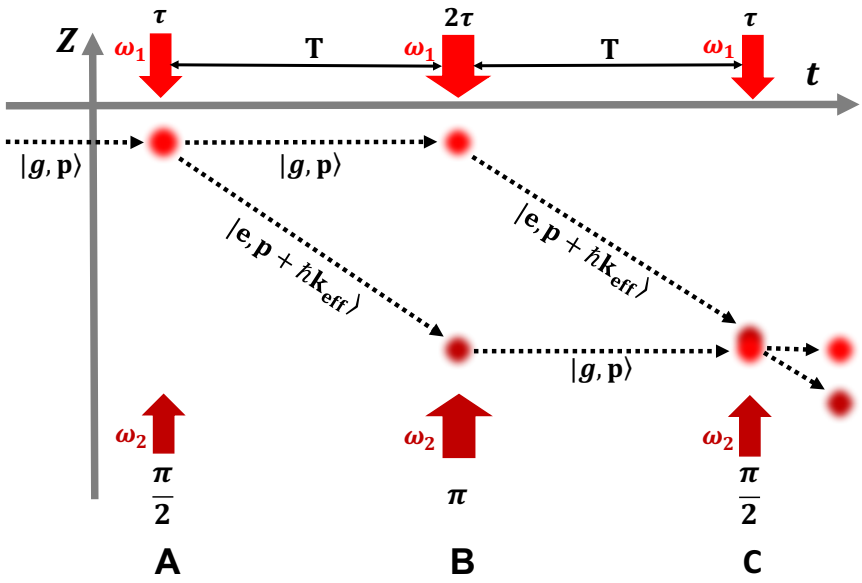

Figure 2.3: Diagram of the Mach-Zehnder atom interferometer with three Raman laser pulses. The positions where the Raman pulse is employed are labelled by A, B, C respectively. The first $\pi/2$ pulse gives a momentum kick to half of the atoms, causing them to move away. The π pulse inverts this separation and the final $\pi/2$ pulse recombines the states. An interference pattern is then observed as population differences in the two output states. The ratio of the output states is governed by the phase difference between the paths.

The effect of a Raman transition can be modelled by a matrix. The initial state is a vector composed of the two probability amplitudes $a_g(t_0)$ and $a_e(t_0)$. According to the coefficient Equ. 2.20, time evolution equations in the matrix formalism are expressed as:

$$\begin{pmatrix} a_{g,\mathbf{p}}(t_0+\tau) \\ a_{e,\mathbf{p}+\hbar\mathbf{k}_{eff}}(t_0+\tau) \end{pmatrix} = M(t_0, \phi_{eff}, \Omega_{eff}, \tau) \begin{pmatrix} a_{g,\mathbf{p}}(t_0) \\ a_{e,\mathbf{p}+\hbar\mathbf{k}_{eff}}(t_0) \end{pmatrix} \tag{2.26}$$

Suppose that the Raman lasers are on resonance ($\delta = 0$) and the AC Stark shift is eliminated $\delta^{AC} = 0$. The evolution matrix is given by:

$$M(t_0, \phi_{eff}, \Omega_{eff}, \tau) = \begin{pmatrix} \cos\left(\frac{|\Omega_{eff}|\tau}{2}\right) e^{-i\omega_g'\tau} & -ie^{i(\omega_{eff}t_0+\phi_{eff})}\sin\left(\frac{|\Omega_{eff}|\tau}{2}\right) e^{-i\omega_g'\tau} \\ -ie^{-i(\omega_{eff}t_0+\phi_{eff})}\sin\left(\frac{|\Omega_{eff}|\tau}{2}\right) e^{-i\omega_e'\tau} & \cos\left(\frac{|\Omega_{eff}|\tau}{2}\right) e^{-i\omega_e'\tau} \end{pmatrix} \tag{2.27}$$

Between each Raman transition, the lasers are switched off and the wave function evolves freely during a time

interval T. Substituting $\Omega_{eff} = 0$ into above equation, the matrix of evolution without coupling becomes:

$$M(\tau = T) = \begin{pmatrix} e^{-i\omega_g^{'}\tau} & 0 \\ 0 & e^{-i\omega_e^{'}\tau} \end{pmatrix} \tag{2.28}$$

We can now calculate the population of the two states at the output of the atom interferometer by successively applying Equ. 2.26 onto the initial state. The matrix is written as the product of three matrices of Raman transitions with durations τ and 2τ and two free evolution matrices. By choosing the time origin as the center of the π pulse, the entire evolution matrix during the sequence is:

$$M_{total} = M(T+\tau, \phi_C(z), \Omega_{eff}, \tau)M(T)M(-\tau, \phi_B(z), \Omega_{eff}, 2\tau)M(T)M(-T-2\tau, \phi_A(z), \Omega_{eff}, \tau) \tag{2.29}$$

where $\phi_A(z)$, $\phi_B(z)$ and $\phi_C(z)$ are the light phase of the Raman laser at the atomic positions during the three Raman pulses. The phase change during the pulse is neglected. After expanding the five matrices and applying the initial states ($a_{g,\mathbf{p}}(0) = 1, a_{e,\mathbf{p}+\hbar\mathbf{k}_{eff}}(0) = 0$), we achieve the population probability of the atoms in $\mid e, \mathbf{p} + \hbar\mathbf{k}_{eff}\rangle$ at the output:

$$\boxed{P_{|e,\mathbf{p}+\hbar\mathbf{k}_{eff}\rangle} = \mid C_{|e,\mathbf{p}+\hbar\mathbf{k}_{eff}\rangle} \mid^2 = \frac{1}{2}\left[1 - \cos(\phi_A(z) - 2\phi_B(z) + \phi_C(z))\right]} \tag{2.30}$$

The probability is determined by the phase difference between the two arms. The interference fringes have a 100% contrast when the transitions are resonant, without light shift, which is analogous to optics, when the splitters distribute the intensity equally between the two arms and the mirrors redirects all of the incident light.

2.2.2 Phase Shift Due to g

The amplitudes of the population probability depends on the phase difference of the Raman lasers during the transition. In the gravity field, the atoms are accelerated during free fall. The altitude of the atoms varies as -$\frac{1}{2}gt^2$. If the two Raman lasers are aligned vertically, their phase difference is written as:

$$\begin{aligned} \phi(t) = \phi(1) - \phi(2) &= (\omega_1 - \omega_2)t - (\mathbf{k}_1 - \mathbf{k}_2)\cdot\mathbf{z}(t) + \delta\phi(t) \\ &= \omega_{eff}t - \mathbf{k}_{eff}\cdot\mathbf{z}(t) + \delta\phi(t) \end{aligned} \tag{2.31}$$

Since the constant or linear terms of the phase difference cancel in the interferometry phase, only the term $\mathbf{z}$(t) quadratic in t, and the phase noise term $\delta\phi(t)$ remain. Consider that the atoms fall along the equiphase planes defined by the two counter-propagating lasers. At each transition, the phase difference of the lasers is imprinted on the atoms at the position of the atoms falling along this vertical rule. Substituting Equ. 2.31 into Equ. 2.30, we have

$$\Delta\Phi = \phi_A(z) - 2\phi_B(z) + \phi_C(z) = \mathbf{k}_{eff}\mathbf{g}T^2 + \delta\phi(T) - 2\delta\phi(0) + \delta\phi(T) \tag{2.32}$$

where the terms $\delta\phi(T) - 2\delta\phi(0) + \delta\phi(T)$ represent the laser phase noise at the time of the three Raman pulses.

On the other hand, if the frequency difference of the Raman laser beams remains constant while the atoms are in free-fall, the Doppler shift given by $\delta\omega_D(t) = -\mathbf{k}_{eff} \cdot \mathbf{g}t$ is produced. Thus the resonance condition is lost, the transition probability decreases and the contrast of the interferometry fringe also decreases rapidly. In order to keep the pulses resonant at all times, we sweep the frequency of the three pulses to compensate the Doppler shift as

$$\Delta\omega(t) = \omega_0 + \alpha(t - t_0) \tag{2.33}$$

Evaluating Equ. 2.30 in the falling frame, the final net phase shift is expressed as:

$$\Delta\Phi = (\alpha - \mathbf{k}_{eff} \cdot \mathbf{g})T^2 \tag{2.34}$$

Gravity is measured at the central fringe where $\alpha = \mathbf{k}_{eff} \cdot \mathbf{g}$, meaning the Doppler shift is compensated.

2.2.3 Light Shift

In our experiment, we drive stimulated Raman transitions on the ^{87}Rb D_2 line, which is not a simple three-level system. The hyperfine splitting of the excited level $5^2P_{3/2}$ is shown in Fig. 2.4. The Raman transition is driven between the two ground states $|^5S_{1/2}, F = 1\rangle$ and $|^5S_{1/2}, F = 2\rangle$. When the atom interacts with the laser, we need to consider the coupling with all four excited levels. In fact, due to dipole transition selection rules, only the $|5^2P_{3/2}, F^{'} = 1\rangle$ and $|5^2P_{3/2}, F^{'} = 2\rangle$ states can be considered as the virtual levels. We define the detuning Δ in respect to $|5^2P_{3/2}, F^{'} = 1\rangle$ and Δ_1, Δ_2, Δ_3 as the other three levels' energy difference in respect to $|5^2P_{3/2}, F^{'} = 1\rangle$. Thus the light shift in Equ. 2.15 can be rewritten by taking into account all

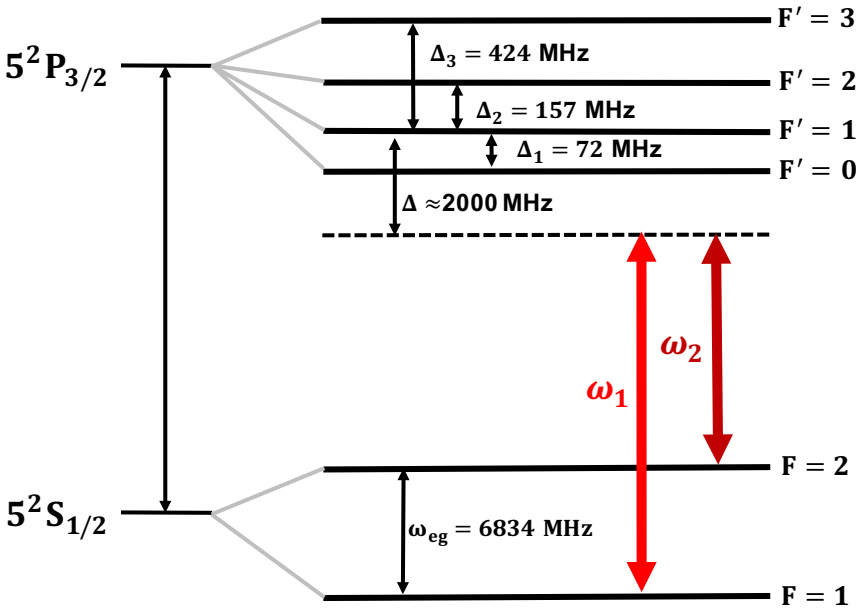

Figure 2.4: Level scheme of the ^{87}Rb D2 line and the levels chosen for Raman transitions. Energy level differences are not drawn to scale. Two-photon Raman transition is driven between the two ground states $|^5S_{1/2}, F = 1\rangle$ and $|^5S_{1/2}, F = 2\rangle$ by Raman laser ω_1 and ω_2. The detuning Δ is defined in respect to $|5^2P_{3/2}, F^{'} = 1\rangle$ and Δ_1, Δ_2, Δ_3 are the detuning of the other three levels' energy difference in respect to $|5^2P_{3/2}, F^{'} = 1\rangle$. $\Delta = 2000$ MHz is the experimental parameter in this thesis.

interactions between the laser and atomic levels:

$$\begin{aligned}\Omega_g^{AC} &= \sum_k \frac{|\Omega_{k,g,1}|^2}{4(\Delta + \Delta_k)} + \frac{|\Omega_{k,g,2}|^2}{4(\Delta + \Delta_k - \omega_{eg})} \\ \Omega_e^{AC} &= \sum_k \frac{|\Omega_{k,e,1}|^2}{4(\Delta + \Delta_k + \omega_{eg})} + \frac{|\Omega_{k,e,2}|^2}{4(\Delta + \Delta_k)}\end{aligned} \tag{2.35}$$

where $\Omega_{k,F,n} = -\langle i, F^{'} = k|\mathbf{d}\cdot\mathbf{E}_n|F\rangle/\hbar$ is the Rabi frequency between the ground states $g = |5^2S_{1/2}, F = 1\rangle$ or $e = |5^2S_{1/2}, F = 2\rangle$, and the excited states $|5^2P_{3/2}, F^{'} = k\rangle$ coupled by the laser ω_n. Taking into account the Clebsch-Gordan coefficients and the linear polarisation of the Raman laser [84], the above equation can be written as:

$$\begin{aligned}\Omega_g^{AC} &= \frac{\Omega_1^2}{4}\left(\frac{5}{24\Delta} + \frac{1}{8(\Delta - \Delta_2)}\right) + \frac{\Omega_2^2}{4}\left(\frac{5}{24(\Delta - \omega_{eg})} + \frac{1}{8(\Delta - \Delta_2 - \omega_{eg})}\right) \\ \Omega_e^{AC} &= \frac{\Omega_1^2}{4}\left(\frac{1}{120(\Delta + \omega_{eg})} + \frac{1}{8(\Delta - \Delta_2 + \omega_{eg})} + \frac{1}{5(\Delta - \Delta_3 + \omega_{eg})}\right) + \frac{\Omega_2^2}{4}\left(\frac{1}{120\Delta} + \frac{1}{8(\Delta - \Delta_2) + 5(\Delta - \Delta_3)}\right)\end{aligned} \tag{2.36}$$

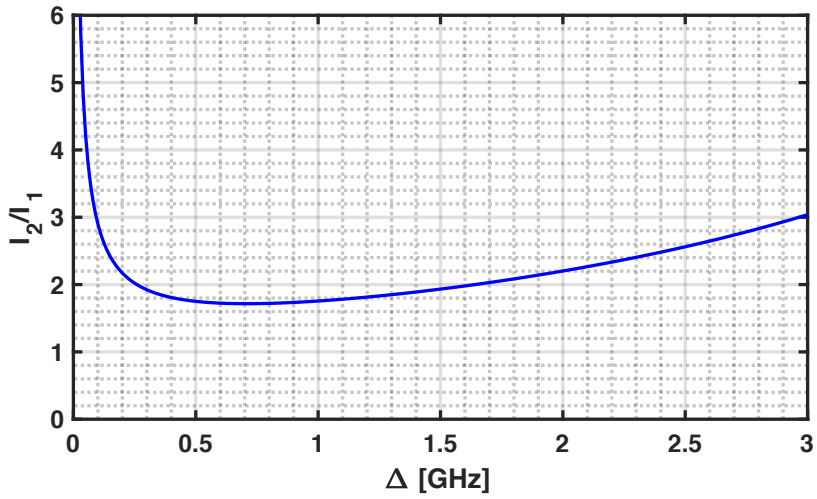

Figure 2.5: The intensity ratio of Raman laser for cancelling the AC stark shift plotted as a function of the detuning Δ.

where the Rabi frequency Ω_i is geivn by involving the laser intensity I_i, the saturation intensity I_{sat} and the linewidth Γ[84]:

$$|\Omega_i| = \frac{\Gamma}{\sqrt{2}}\sqrt{\frac{I_i}{I_{sat}}} \tag{2.37}$$

The light shift changes the energy difference between the ground hyperfine levels (AC Stark effect), resulting in a Raman transition that will not exactly satisfy the resonance condition. As a consequence, the interferometer will have an additional phase shift due to the light shift:

$$\delta\Phi = \frac{\delta_A^{AC} - \delta_C^{AC}}{\Omega_{eff}} \tag{2.38}$$

where δ_A^{AC} and δ_C^{AC} are the differential light shifts during the $\pi/2$ pulse at A and C. According the euq. 2.36 and 2.38, the light shift is a linear combination of the laser intensities. We can cancel the light shift by carefully choosing the ratio of the two laser intensities I_1 and I_2, where $\delta^{AC} = 0$. The ratio is a function of detuning Δ and given by:

$$\boxed{R = \frac{|E_2|^2}{|E_1|^2} = \frac{I_2}{I_1} = \frac{(\frac{1}{60(\Delta+\omega_{eg})} + \frac{1}{4(\Delta-\Delta_2+\omega_{eg})} + \frac{2}{5(\Delta-\Delta_3+\omega_{eg})}) - (\frac{5}{12\Delta} + \frac{1}{4(\Delta-\Delta_2)})}{(\frac{5}{12(\Delta-\omega_{eg})} + \frac{1}{4(\Delta-\Delta_2-\omega_{eg})}) - (\frac{1}{60\Delta} + \frac{1}{4(\Delta-\Delta_2)} + \frac{2}{5(\Delta-\Delta_3)})}} \tag{2.39}$$

We plot the required ratio in Fig. 2.5 as a function of the detuning Δ. It is shown that, when Δ=2 GHz, the light shift vanishes for $R \approx 2.1$. We will measure the actual ratio in experiment, which will be introduced in chapter 5.

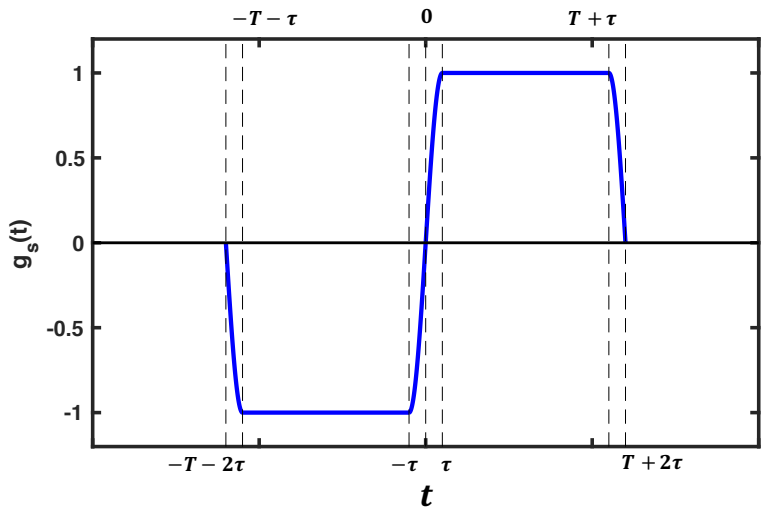

Figure 2.6: Sensitivity Function g_s(t) as a function of the instant phase jump of the Raman laser.

2.3 Phase Noise

During the interferometry process, various kinds of noise exist to shift the interferometry phase Φ. In the following sections, we will introduce a tool called the sensitivity function to characterize the sensitivity of the interferometer to different sources of noise. This method was experimentally verified in the atom interferometer [85] and is described in detail elsewhere[86, 87]. We summarize the explicit mathematical formulas and make an application in evaluating the phase noise of the Raman laser and vibration noise. The other effects (for example magnetic field) are evaluated with the same method in chapter 5.

2.3.1 Sensitivity Function

If an elementary phase jump $\delta\phi$ of the Raman laser happens at time t, the transition probability P is changed by δP. The sensitivity function g_s can be defined as:

$$g_s(t) = 2 \lim_{\delta\phi \to 0} \frac{\delta P(\delta\phi, t)}{\delta\phi} \tag{2.40}$$

For simplicity, we assume the interferometer phase is $\Phi = \frac{\pi}{2}$, where the transition probability is 1/2 and has the highest sensitivity to the phase jump. With a small phase jump $\delta\phi$, the transition probability is:

$$P(\delta\phi, t) = \frac{1 - cos(\frac{\pi}{2} \pm \delta\Phi(\delta\phi, t))}{2} \approx \frac{1 \pm \delta\Phi(\delta\phi, t)}{2} \tag{2.41}$$

After substituting the above equation into the sensitivity function, we achieve the new sensitivity function:

$$g_s(t) = \lim_{\delta\phi \to 0} \frac{\delta\Phi(\delta\phi, t)}{\delta\phi} \tag{2.42}$$

The phase fluctuation $\delta\phi$ is most probable to happen during the free evolution time or during the duration of the pulse. We firstly assume the duration of the pulse is negligible with respect to the free evolution interval T. If the phase jump takes place during the first free evolution (-T<t<0), it is also added to the phases of the second and third pulses. Since the laser phase is considered constant elsewhere, the interferometry phase shift becomes:

$$\Phi = \phi(-T) - 2(\phi(0) + \delta\phi) + (\phi(T) + \delta\phi) = \frac{\pi}{2} - \delta\phi \tag{2.43}$$

Therefore $\delta\Phi = -\delta\phi$ and the sensitivity function is -1 for -T<t<0. In the same way we find g_s (t) = +1 for 0 <t<T. In the general case where the duration of the pulses is not negligible, the expression of g_s is obtained by modifying the matrices which comprise the total matrix of the interferometer (Equ. 2.29). If a phase jump occurs during a pulse, the matrix of this transition is considered to be the product of the matrix before and after the phase jump individually. Thus we can derive the complete sensitivity function for the atom interferometer [83]:

$$g_s(t) = \begin{cases} \sin(\Omega_r(t+T)) & -T - 2\tau < t < -T - \tau \\ -1 & -T - \tau < t < -\tau \\ \sin(\Omega_r t) & -\tau < t < \tau \\ 1 & \tau < t < T + \tau \\ \sin(\Omega_r(t-T)) & T + \tau < t < T + 2\tau \\ 0 & \text{else} \end{cases} \tag{2.44}$$

The function is zero outside the interferometer. The visualization of the above function is plotted in Fig. 2.6.

2.3.2 Laser Phase Noise

We now can evaluate the influence of phase noise of the lasers by:

$$\delta\Phi = \int g_s(t) d\phi(t) = \int g_s(t) \frac{d\phi(t)}{dt} dt \tag{2.45}$$

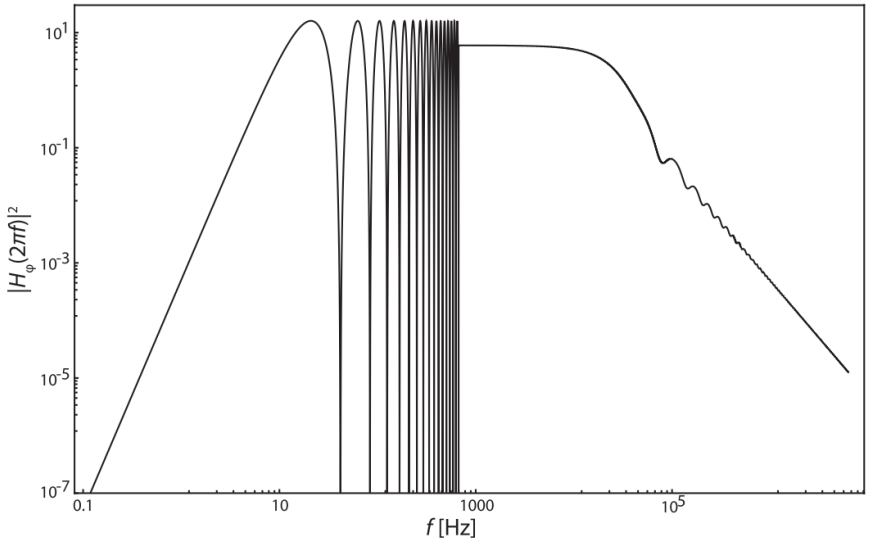

Figure 2.7: Double logarithmic plot of $|\mathrm{H}(\omega)|^2$ for T=150 ms and τ=100 μs, averaged after 16 oscillations due to its highly oscillation behaviour. Cited from [83].

However, in practice, it is much easier to measure the phase noise in the frequency domain. Let S_ω and S_ϕ be the power spectral densities (PSD) of the phase noise of the Raman laser, expressed in terms of frequency and phase. The variance of the corresponding interferometry phase noise is then written as:

$$\begin{aligned}\sigma_\Phi^2 &= \int_0^{+\infty} \mid G(\omega) \mid^2 S_\omega(\omega) d\omega \\ &= \int_0^{+\infty} \mid \omega G(\omega) \mid^2 S_\phi(\omega) d\omega \\ &= \int_0^{+\infty} \mid H(\omega) \mid^2 S_\phi(\omega) d\omega\end{aligned} \tag{2.46}$$

where $G(\omega)$ is the Fourier transform of the sensitivity function $g_s(t)$. $H(\omega)$ is defined as a weighting function, which is expressed as:

$$\boxed{H(\omega) = \int_{-\infty}^{+\infty} e^{-i\omega t} g(t) dt = \frac{4i\omega\Omega_r}{\omega^2 - \Omega_r^2} \sin(\frac{\omega(T+2\tau)}{2})(\cos(\frac{\omega(T+2\tau)}{2}) + \frac{\Omega_r}{\omega}\sin(\frac{\omega T}{2}))} \tag{2.47}$$

As shown in Fig. 2.7, the weighting function acts as a band pass filter. The low-pass filtering at high frequency is characterized with a cut-off frequency given by $f_c = \sqrt{3}\Omega_R/6\pi = \sqrt{3}/(12\tau)$, due to the fact that the response time of the atoms is necessarily limited by the Rabi frequency. Longer Raman pulses reduce the contribution of the phase noise at high frequencies. It should be noted, however, that the number of atoms selected by the Raman transition is low, resulting in degradation of the contrast of the atom interferometry

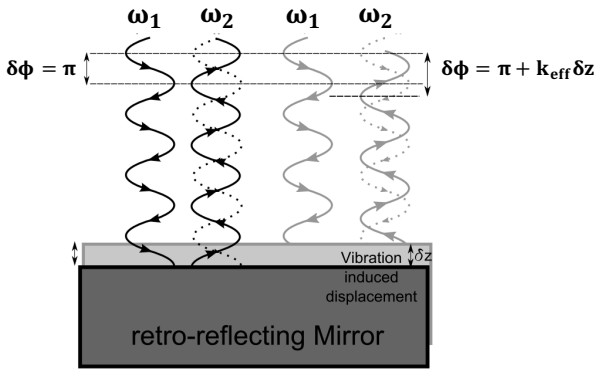

Figure 2.8: Vibration induced phase noise. The relative phase between Raman laser ω_1 and ω_2 changes depending on the displacement δz which are depicted by black/grey lines. Modified from [88].

fringe. The series of zeros in the weighting function corresponds to the fluctuations whose period is multiples of T + 2τ. In this case, the perturbation of the phase jump is identical for all the three pulses and the interferometry phase shift vanishes.

2.3.3 Vibration Noise

The counter-propagating frequency pair for the two-photon Raman transition is generated in using a retro-reflection geometry: both beams enter the vacuum chamber from the top and a mirror located beneath the vacuum enclosure retro-reflects both beams. The advantage of this configuration is that any mechanical noise on the optical components before entering the vacuum chamber is common to all Raman beams. The phase difference between the two Raman beams is then defined by the position of the retro-reflection mirror. In chapter 4, a passive vibration isolator is used to suppress the seismic noise on the mirror. However, due to the limited capability of the platform, the residual vibration is still a main limitation for the measurement sensitivity. The sensitivity function is extended to evaluate the influence of the vibration noise. Following the idea above, we define the sensitivity function due to vibration of the mirror as

$$g_a(t) = 2 \lim_{\delta a \to 0} \frac{\delta P(\delta a, t)}{\delta a} \tag{2.48}$$

As shown in Fig. 2.8, considering an infinitesimal displacement δz, the phase of the beam on the back reflection path is changed by $\delta\phi = 2\mathbf{k}_i \delta z \approx \mathbf{k}_{eff}\delta z$. Therefore $g_a(t)$ can be expressed as:

$$g_a(t) = \frac{d^2 g_z(t)}{dt^2} = \frac{1}{\mathbf{k}_{eff}} \frac{d^2 g_s(t)}{dt^2} \tag{2.49}$$

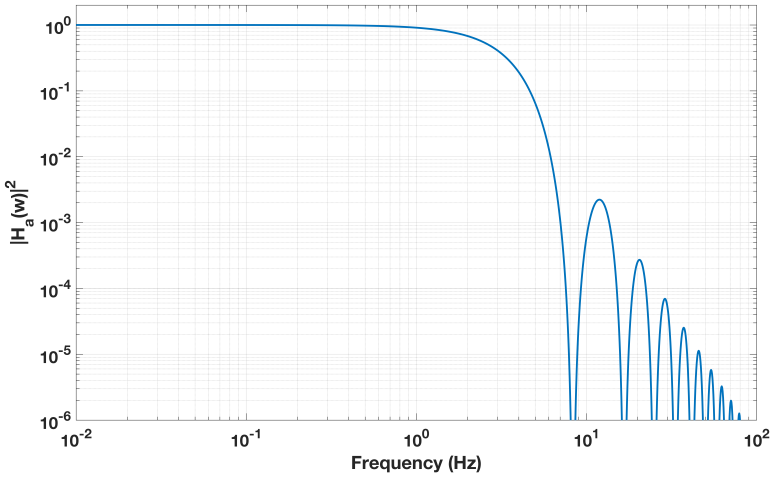

Figure 2.9: The square of the acceleration transfer function $H_a(\omega)$ for T=120 ms.

The PSD of the Raman phase noise induced by the vibration is therefore:

$$S_\varphi(\omega) = \mathbf{k}_{eff}^2 S_z(\omega) = \mathbf{k}_{eff}^2 \frac{S_a(\omega)}{\omega^4} \tag{2.50}$$

where $S_a(\omega)$ is the PSD of the vertical vibrations of the mirror in units of $(\mathrm{m/s^2})^2/\mathrm{Hz}$. The corresponding interferometry phase noise can be evaluated by:

$$\boxed{\sigma_\Phi^{rms} = \sqrt{\int_0^\infty |H_\phi(\omega)|^2 \frac{k_{eff}^2}{\omega^4} S_a(\omega) d\omega}} \tag{2.51}$$

Fig. 2.9 shows the transfer function $|H_a(\omega)|^2$ for T=120 ms. The function behaves as a second order low pass filter and the cut-off frequency is $f_0 = \frac{1}{2T}$. The overall interferometer phase is most sensitive to frequency vibrations below 10 Hz.

2.4 Summary

This chapter presented a theoretical description of an atom interferometer based upon stimulated Raman transitions. We discussed how Raman pulses transfer population and create the interference between the atomic states. Emphasis was put on the derivation of the ratio in the state populations after a Mach-Zehnder type sequence of Raman pulses. At the output, a Doppler phase shift is accumulated when atoms free fall in the gravity field. This gives rise to a tool for high-precision measurements of gravity. Finally, we derived

the sensitivity function as well as the phase noise transfer function in the form of Raman phase noise and vibration. These tools will be used in chapter 5 to characterize the sensitivity limitation and the systemic errors in the current experiment.

CHAPTER 3

ATOMIC FOUNTAIN

This chapter provides a description of the experimental apparatus and the realization of the atomic fountain. The science chamber is inherited from a previous project, which will be summarised in the first section. The work of the author is presented from the second section onwards, focusing on the realisation and optimisation of the atomic fountain.

3.1 Apparatus Review

3.1.1 Science Chamber

The experiment is operated in an ultra-high-vacuum (UHV) environment in the 10^{-10} mBar region, in order to minimise collisions of trapped atoms with background gas. Figure 3.1 shows the schematic of the vacuum system with some other components. The mechanical design and construction were done by former students, Alex Niggebaum and Andrew Hinton. More details can be found in their theses [78, 79]. For a complete description, the following paragraph will give a summary.

MOT Chamber: The material of the entire vacuum system is Titanium, which is a high-strength, lightweight, low-magnetism and high resistivity metal. These properties help to suppress eddy currents and reduce parasitic magnetic fields. The main part is the magneto-optical-trap (MOT) chamber for a three dimensional MOT (3D MOT), which prepares atoms for the atom interferometer. The MOT chamber is machined to be the shape of an octagonal prism. Six square surfaces are drilled orthogonally for optical access of the MOT laser beams. The chamber is oriented with four beams having an angle of α=45° and the other two perpendicular to the vertical axis respectively. The bottom of the MOT chamber is drilled with holes of 40 mm in diameter for the Raman laser. A 20 mm thick window is mounted at a slight angle to

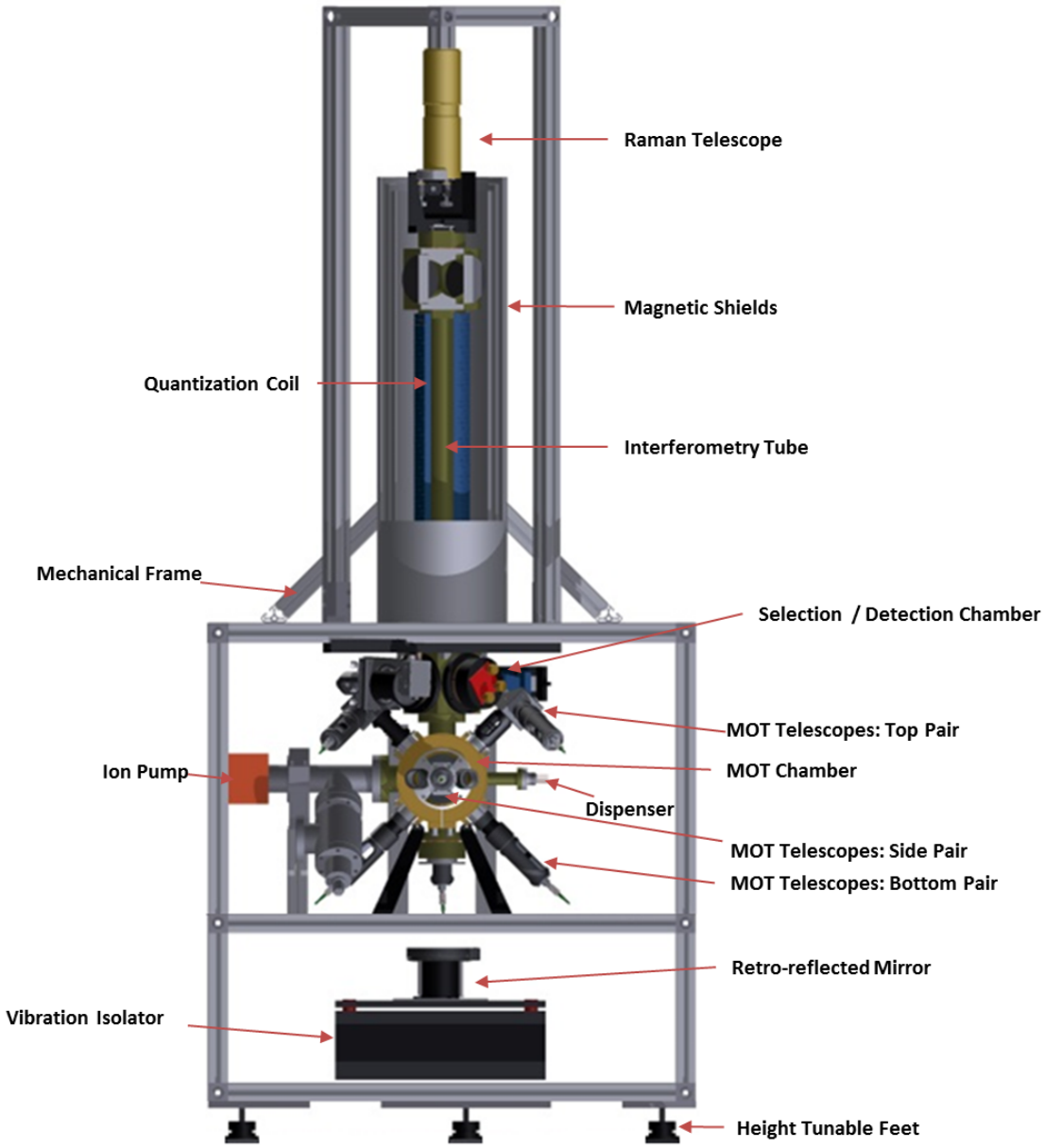

Figure 3.1: Schematic of the main functional parts of the experimental apparatus.

eliminate the risk of a standing wave forming from the window at the opposite end of the chamber. All the windows are sealed by indium.

Pump: The UHV is achieved and maintained by an ion pump (SAES NEXTorr 100-5), associating ion pump (6 l/s) and non evaporative getter. This combination provides an equivalent pumping speed of 100 l/s with a compact size. The primary pump is housed by a T-piece and connected with the MOT chamber on a CF40 flange. The T-piece keeps the ion pump away from the MOT chamber by 15 cm. Thus the strong magnetic fields from the ion pump decay sufficiently to below 0.5 Gauss around the MOT chamber region.

Atom Source: The 3D MOT was initially fed from a 2 dimensional MOT (2D MOT). However, it was removed because the pressure inside the chamber was found to be too high to trap atoms. This is possibly because a careless mechanical design allows for poor connectivity between the 2D MOT chamber and its compact ion pump. Instead, the rubidium source now evaporates from the rubidium dispensers, which are installed on a CF16 flange. But the option of a 2D MOT is still open in the future.

Interrogation Tube: The interrogation region consists of a 50 cm long titanium tube. Each end of the tube is connected to a cube, which has four indium-sealed windows for horizontal optical access.

System Mounting: The whole system is suspended on an aluminium frame of dimensions (H×W×D): 162.8 cm × 95.5 cm × 45.9 cm. This package also includes the vibration isolator. At the bottom of the frame, three height tunable feet are mounted to provide the flexibility to align the apparatus and adjust the direction of the atom launch.

3.1.2 Atom Trapping

The experiment starts by trapping atoms using the technique called magneto-optical trapping, which generates a spatially dependent force to trap neutral atoms[89]. The typical configuration of the MOT is illustrated in Fig. 3.2a. Three pairs of counter-propagating laser beams are set in orthogonality. One pair of anti-Helmholtz coils creates a quadrupole magnetic field, where the magnetic field in the MOT centre is zero and increases linearly along all directions. Fig. 3.2b shows the one-dimensional case. Atomic magnetically sensitive m_f levels split proportional to the magnetic field strength due to the Zeeman effect. The polarisation of the laser beams are set to match the transition selection rules. Thus atoms are more likely to absorb photons from the laser beam which is opposite to its motion. The atoms are hence pushed back towards the centre.

Since thermal atoms generally have a momentum that is thousands of times higher than one single photon's, atom trapping must involve many absorption-spontaneous emission cycles, which requires the

atomic structure to possess a cycling transition [90]. The specific requirement for ^{87}Rb is that a repump laser is required to avoid atoms falling into the dark state F=1 where they would stop cycling. The level scheme of ^{87}Rb is listed in Fig. 3.4.

The temperature in the MOT is bound by the Doppler limit, which is 146 μK for rubidium [84]. After the MOT is switched off, atoms diffuse quickly. In order to slow down the burst, a technique called optical molasses is applied [91]. The general procedure is to increase the laser detuning and decrease the laser intensity within a few ms once the anti-Helmholtz coils are switched off. During this period, the mechanism of polarisation gradient cooling can reduce the temperature of atoms further to a temperature which is limited by the recoil limit (0.35 μK for rubidium [84]).

In the GGtop experiment, the MOT temperature was around 4 mK and the molasses temperature was 17 μK. This is the starting point for the atomic fountain and atom interferometry in the reference platform project.

3.2 Atomic Fountain Design

As discussed in chapter 2, the sensitivity of atom interferometry is proportional to T^2, where T is the free evolution time in the atom interferometer. For high sensitivity gravimeters, large T is desired. However, atoms released from the MOT chamber will start to fall downwards and be accelerated due to gravity. For time scales on the order of 1 s, the atoms will fall about 5 m away from the original trapping region in the vertical direction. It is impractical and uneconomical to build an enormous apparatus to achieve sufficiently long T. One straightforward solution is to create a fountain to launch the atoms upwards. This rise-and-fall geometry doubles the maximum interrogation time for a given apparatus [92], and also provides the potential to build a gradiometer in the future [93]. The following paragraph will provide a detailed description of the atomic fountain apparatus, including the laser distribution, the detection scheme and the control system. The relevant results will be presented in the next section.

3.2.1 Moving Molasses Geometry

In a standard optical molasses introduced above, the frequencies of all MOT laser beams are equal and the atoms are cooled isotropically in the laboratory frame. This is a so-called static molasses since the atom experiences a null resultant force when its velocity is zero. If the frequencies of one pair of counter-propagating

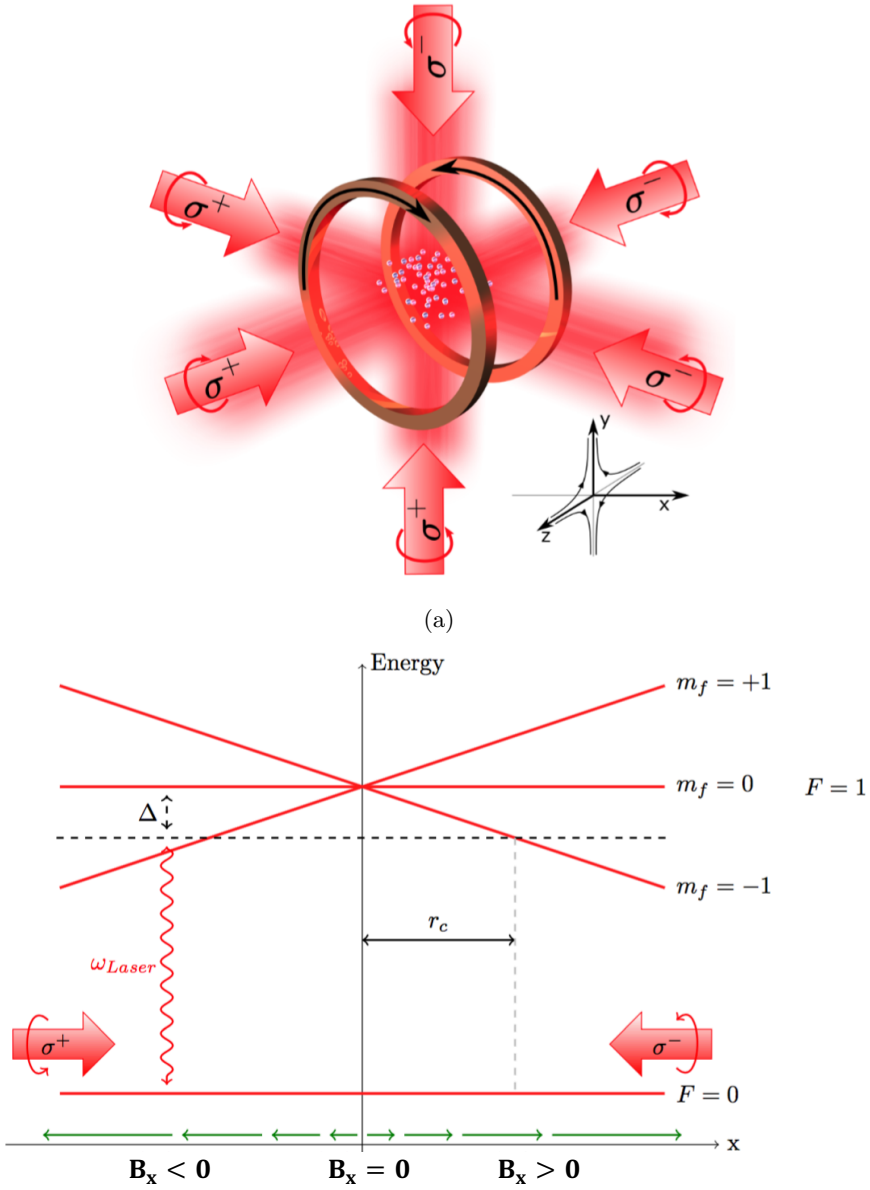

Figure 3.2: Geometry of a 3D MOT. Fig. 3.2a indicates the typical configuration including the polarisations of three pairs of laser beams and the anti-Helmholtz coils. The magnetic field in the MOT centre is zero and increases linearly along all directions. The magnetically sensitive m_f levels split due to the Zeeman effect. Fig. 3.2b shows the one-dimensional case. According to the selection rules, beams labelled $+\sigma$ and $\sigma-$ drive the Δm_f=+1 and Δm_f=-1 transition respectively. Thus atoms are more likely to absorb the photon from the laser beam which is opposite to its motion. (Fig. 3.2a and Fig. 3.2b are cited from Alex Niggebaum's thesis [78].)

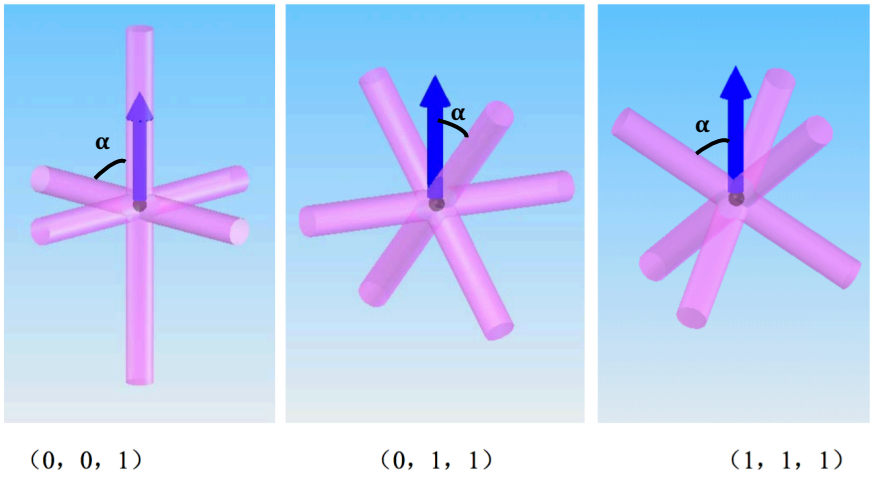

Figure 3.3: Typical spatial configuration of laser beams for moving molasses. The arrow in blue indicates the vector of the launch velocity. The angle between the vector and the laser is labelled by α.

cooling beams are shifted by a relative detuning as

$$\omega_1 = \omega_0 + \Delta\omega, \omega_2 = \omega_0 - \Delta\omega \tag{3.1}$$

where ω_0 is the normal frequency of the cooling laser and $\Delta\omega$ is the relative detuning, atoms will be accelarated along the beam direction until the Doppler shift compensates the relative detuning. A new equilibrium is built in the atomic moving frame, where atoms will be cooled about a velocity v [94, 95]. Depending on the orientation of the MOT laser beams, the moving molasses can be classified as one of three spatial configurations as shown in Fig. 3.3: one-dimensional moving molasses (0,0,1), two-dimensional moving molasses (0,1,1) and three-dimensional moving molasses (1,1,1). The corresponding launch velocity and direction are determined by the relative detuning and spatial configuration. Assuming the angle between the launch direction of the atoms and the laser propagation direction is α, the velocities in the three configurations are given by:

$$\begin{aligned}(0,0,1) &: v = \frac{\Delta\omega}{\mathbf{k}} \\ (0,1,1) &: v = \frac{2\cos(45^\circ)\Delta\omega}{\mathbf{k}} \\ (1,1,1) &: v = \frac{3\cos(54.7^\circ)\Delta\omega}{\mathbf{k}}\end{aligned} \tag{3.2}$$

where $\mathbf{k}$ is the wavevector of the laser.

In our experiment, we trap atoms in a 3D MOT at first and we adopt the two-dimensional moving molasses

(0,1,1) to launch the atoms. The frequency of the two top beams and bottom beams are red shifted and blue shifted respectively relative to the side beams' frequency. Thus the atoms achieve an equilibrium velocity upwards with respect to the laboratory frame [96].

3.2.2 Optics Delivery

To realize the atomic fountain via the moving molasses, the optical delivery system should satisfy two basic requirements as below:

(1) Three pairs of beams, namely the side pair, the top pair and the bottom pair of laser beams must be controlled independently in terms of frequency and intensity;

(2) The power between one opposite pair of laser beams needs to be balanced in order to ensure the launch direction is vertical. It means the intensity and polarisation of the laser must be stable.

In the previous experiment, a fibre optics delivery system consisting of commercially available fibre integrated components was built, to satisfy the robustness and compactness requirements. Each fibre component was spliced in order to reduce the amount of light intensity loss and polarisation fluctuations from angular misalignment which is typically associated with fibre-to-fibre mating sleeves. However because of poor component choices and careless assembly, the polarisation quality was degraded substantially and the polarisation maintaining ability was ruined [79]. In this experiment, miniaturisation is not the chief concern. Therefore a free-space optics delivery system was built to push the experiment on uninterrupted. In parallel, a further exploration on building a fully integrated fibre system was executed in other projects.

Optics Delivery Scheme

We use the ^{87}Rb D_2 transition to produce all the optical frequencies in the experiment. Fig. 3.4 shows the level diagram. These frequencies lie around 780 nm and are easily accessible by laser diodes. The schematic of the free-space system is shown in figure 3.5. When designing the optics system, we also gave consideration to compactness, robustness and power consumption. Finally two readily available commercial lasers (New Focus, Vortex 6900) and one tapered amplifier (New Focus, TA 7600) were chosen to provide the light needed for atom trapping, cooling and launching. (The Raman laser system will be discussed in detail separately in the next chapter). In this optics delivery system, the reference and cooling laser share the same laser source from Laser 1. The seed laser is fed into the tapered amplifier where the laser power is amplified to about 800 mW. Then the light is split into two parts via a polarisation beam splitter (PBS) :

(1) A fraction of the laser power (20 mW) goes through the PBS and subsequently propagates through a

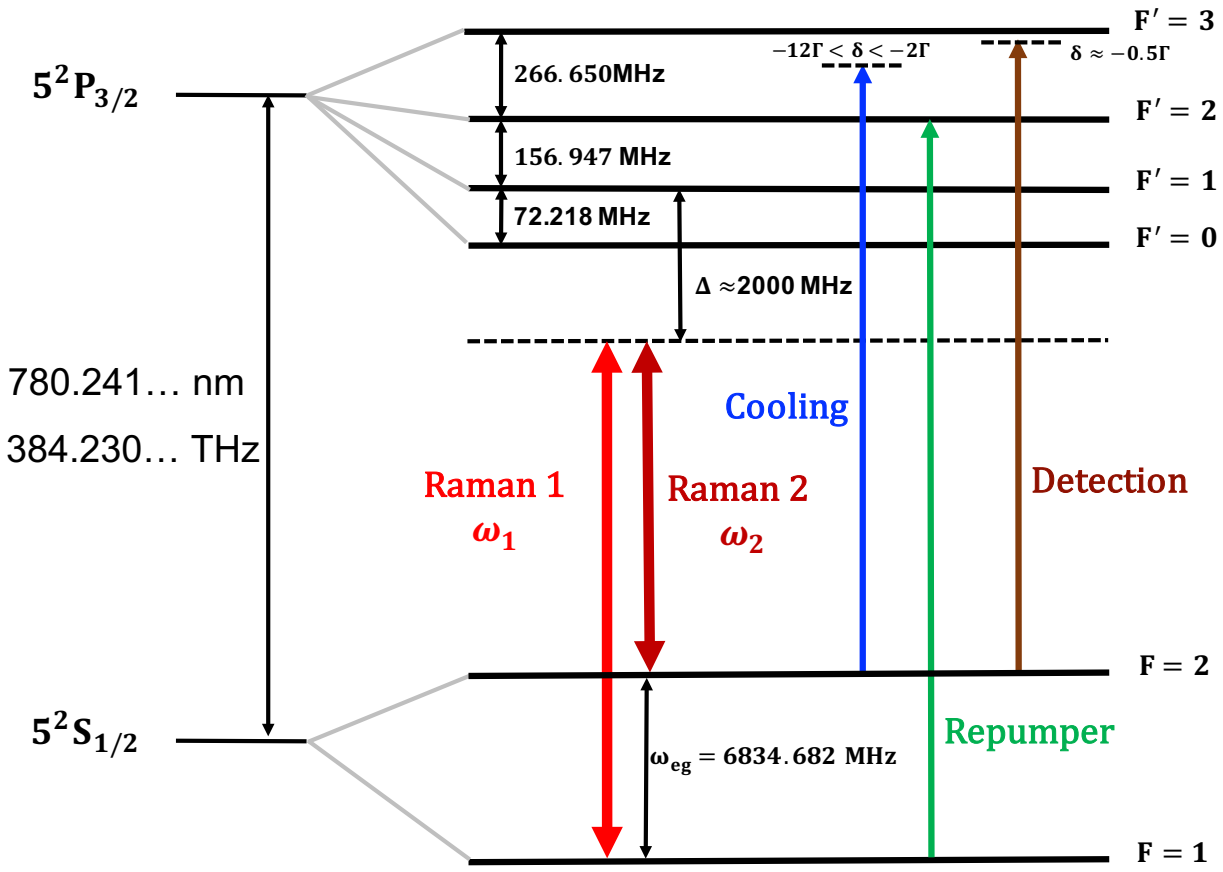

Figure 3.4: ^{87}Rb D_2 transition hyperfine structure, with frequency splittings between the hyperfine energy levels.The frequencies used for the lasers in the experiment and their detunings from the respective energy levels are labelled. Modified from [84].

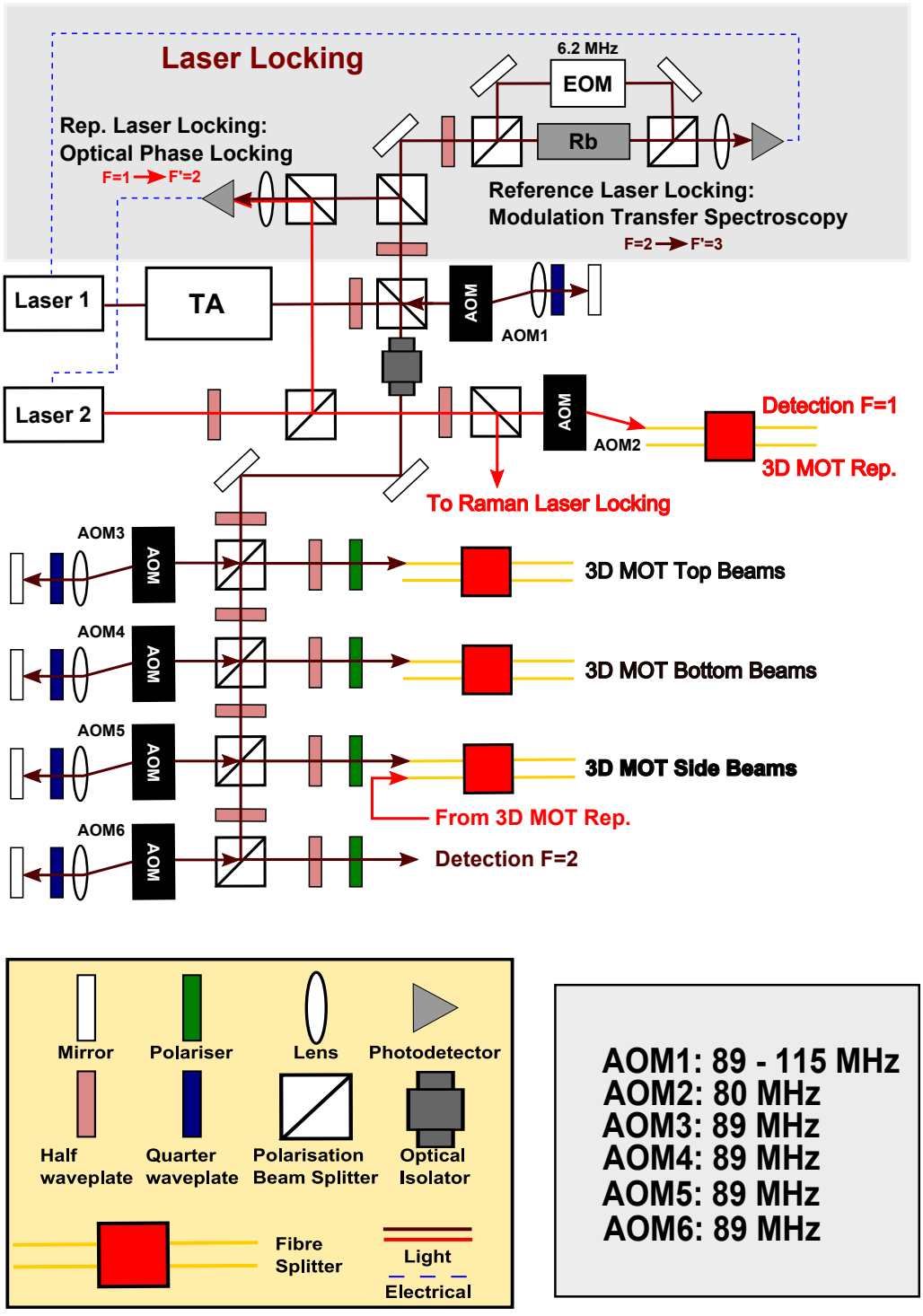

Figure 3.5: Schematic view of the free space optics system. The frequencies used for the experiment is plotted in Fig. 3.4

double-pass AOM setup. The returned light serves as the reference laser, which is injected into the locking stage. The laser is locked on the transition $F = 2 \rightarrow F^{'} = 3$ by Modulation Transfer Spectroscopy (MTS) [97].

(2) Most of the power is reflected by the PBS and delivered to the cooling laser stage, where the laser is split into four paths. Each one includes a double-pass AOM (acousto-optic modulators), which is able to control the frequency and amplitude of the light. Three of the beams returning from the AOMs are injected into three separate 2:2 fiber splitters and lead to the MOT chamber, where they serve as cooling beams. The last path is injected into a fiber and works as a detection beam.

The frequency tuning of the cooling laser beams during the molasses is achieved by varying the RF frequency of AOMs in double pass configuration. The reference laser after double pass through AOM1 gets a frequency shift of $2\omega_1$, where ω_1 is the frequency shift of the first-order diffraction in AOM1. On the other hand, the cooling beams passing through AOMi achieve a frequency shift ω_i (i=3 to 6), where ω_i is the first order shift in AOMi. Therefore, compared to the reference laser frequency, the frequency of the cooling light is shifted by $2(\omega_1 - \omega_i)$ [98]. All the required frequencies of the RF signals driving the AOMs are listed in figure 3.5. The arrangement above decouples the synchronous change of the cooling laser's intensity and frequency when varying the frequency of the RF signal driving the AOM. For example, the frequency of the cooling laser can be shifted by only changing ω_i and its intensity is controlled by changing the power of the RF signal driving the AOMi. In the moving molasses, the top beams and bottom beams achieve a relative detuning by shifting the frequency of AOM3 and AOM4 in the cooling laser stage. This setup also provides flexibility when optimising the molasses. In addition, this method achieves a wide tuning range for the laser frequency. If the bandwidth of a single pass AOM is 20 MHz, then the cooling laser can achieve a tuning range of 80 MHz, which is about 13 times higher than the natural linewidth of ^{87}Rb.

The repump beam is generated using the second New Focus laser module. It is split into two paths: one part is injected into one input port of the fibre splitter for the side beams; the other part is mixed with the reference laser and phase locked on the transition $F = 1 \rightarrow F^{'} = 2$ using a modified ADF 4108 evaluation board from Analog Devices.

During the construction of the optics system, we found a reflection from the cooling laser stage, which interferes with the reference laser. The interference induced ripples on the demodulated signal of the MTS and resulted in losing locking easily. This reflection was induced by the $\lambda/4$ waveplate because of its low reflectivity (about 5%). The interference still existed even after replacing it with an ultra-low reflectivity waveplate. Therefore a 60 dB optical isolator (OL) (LIONS, FI-780-5TVC) is placed in the laser path.

However an 80% transmission of the OL makes optical power loss inevitable.

The polarisation stability is the most basic concern for the optics delivery system. A trick is applied here to maintain polarisation in the fibre. A true zero order $\lambda/2$ waveplate is placed before each fibre coupler and is used to match the laser polarisation with the axis of the fibre. In addition, a polariser is placed between the waveplate and fibre coupler to clean the polarisation further in case any polarisation shifts are introduced by optical components in the path.

Performance Test

After the free-space optics system was set up, a test in terms of the stability of the laser polarisation and beam splitting was made. The test setup is sketched in Fig. 3.6a. One of the outputs of the fibre splitter transmits light through a Glan−Taylor prism (Thorlabs, GT5) which has a Extinction Ratio 100000:1. The power after the prism is measured by the power meter P1 (Thorlabs, PM100D). The other output of the fibre splitter is projected onto the same power meter P2 without a Glan−Taylor prism in the path. Thus on the first power meter, any laser polarisation and intensity fluctuation before the Glan−Taylor prism will be transferred into changes in laser power. Comparing the measurement on both power meters, the splitter ratio of the optical splitter is monitored. We choose the fibre splitter for the side beams deliberately since it is relatively far from the laser source such that the fluctuation is maximized. Figure 3.6b shows the measurement result which lasted for four days. The laser on the two power meters show a common fluctuation, which is induced by the fluctuation of the total laser power. The power on the P1 has a fluctuation of about 0.6%, which is mainly due to the fluctuation of the laser polarisation. This indicates that, in the lab environment, the fibre splitter can split the power steadily.

3.2.3 Detection Scheme

In atom interferometry, the transition probability is usually extracted by the normalized detection, which includes two-state sequential detection [99]. The advantage of this method is that the proportion of the atoms in hyperfine ground states is independent of the fluctuation of the total atom number. However, we employ single state detection in this thesis due to its simple optics requirements. This is feasible because the total atom number in the atomic fountain was checked to be stable in short time. In the meanwhile, a normalized detection setup is being designed and will be employed in the future.

The detection is realized by fluorescence excitation using one sheet beam. The setup is shown in Fig. 3.7. The detection laser is set to be circular polarisation and its frequency is tuned to the transition F=2→F'=3.

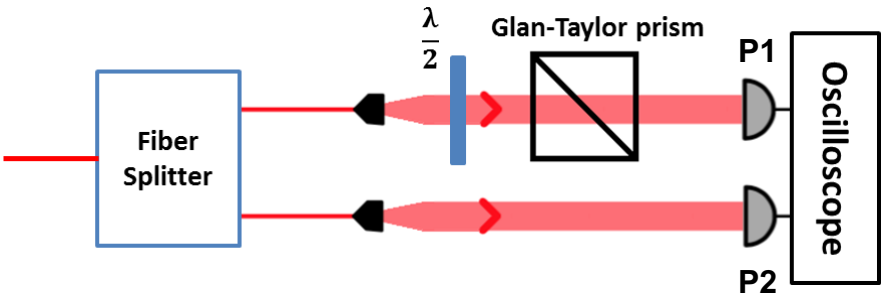

(a)

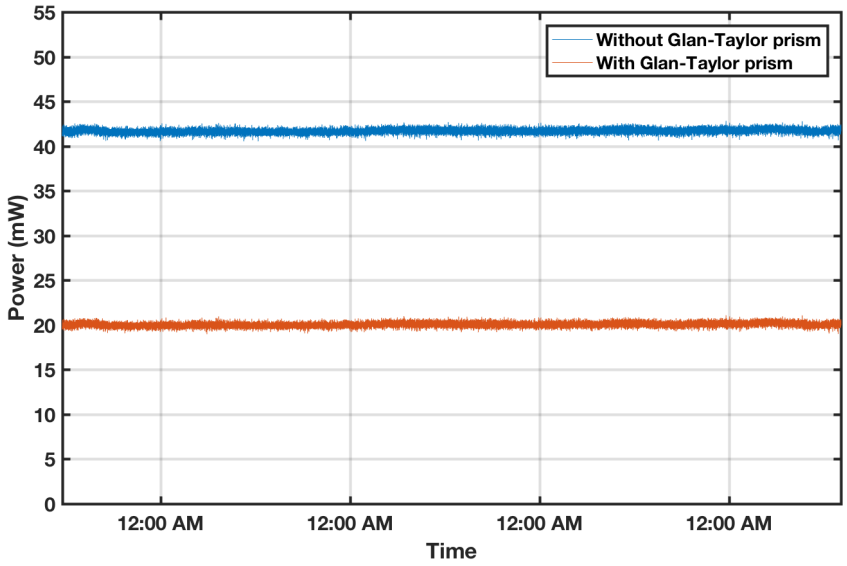

(b)

Figure 3.6: Stability measurement setup (Fig. 3.6a) and results (Fig. 3.6b) of the output light from one fibre splitter in the free space optics system. The two outputs of the 1-to-2 fibre splitter are monitored by two power meters respectively. A Glan-Taylor prism is placed in one path to transfer both the laser polarisation and intensity fluctuations into changes in laser power. The angle of the half-wave-plate with respect to the axis of the polarizer was set to be 22.5°. The measurement was last for four days.

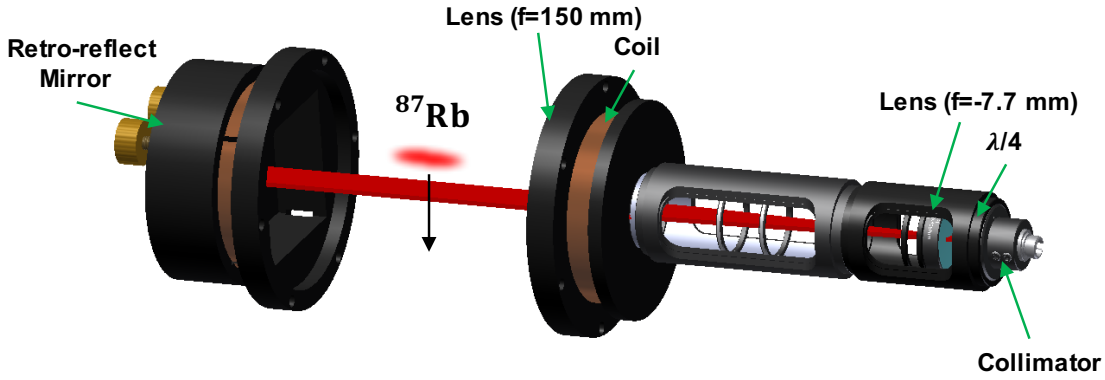

(a)

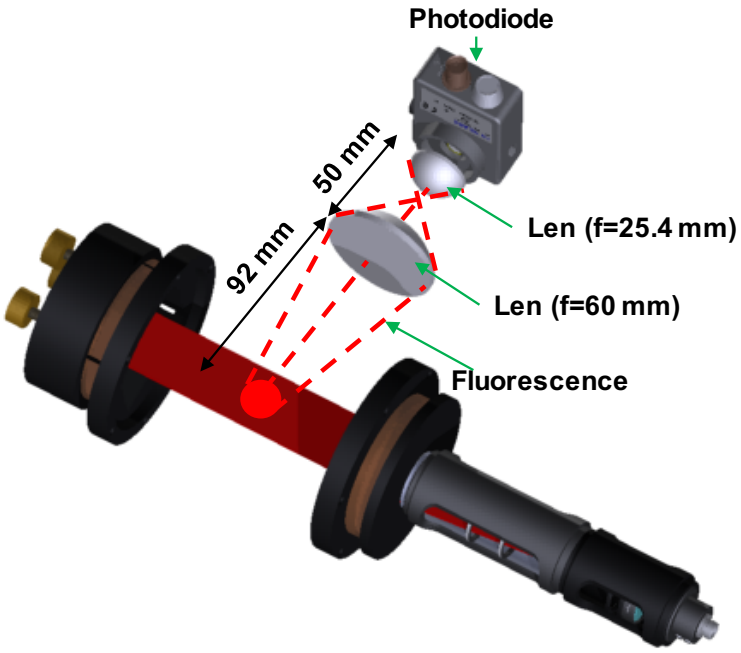

(b)

Figure 3.7: Schematic of the detection setup. Fig. 3.7a shows the the configuration to generate the detection laser. The laser is set to be circular polarisation. A combination of a negative cylinder lens (f=-7.7 mm) and a positive cylinder lens (f=150 mm) generate a sheet beam with 30 mm in width and 1.5 mm in thickness. The upper part of the laser is retro-reflected while the lower part is blocked. A pair of Helmholtz coils is used to generate the magnetic field to define the quantization axis. Fig.3.7b indicates the fluorescence collection optics. The fluorescence emitted from atoms falling through the detection laser is focused on the photodiode by combo of one 2 inch positive lens (f=60 mm) and one 1 inch positive lens (f=25.4 mm). The achieved solid angle is 0.23.

A combination of a negative cylinder lens (f=-7.7 mm) and a positive cylinder lens (f=150 mm) generate a sheet beam with 25 mm in width and 1.5 mm in thickness. The upper part of the laser is retro-reflected while the lower part is blocked. Thus atoms in state F=2 can be blow away when they pass the lower part of the detection laser. A photodiode (Thorlabs, DET36A) is placed on the side to collect the fluorescence in detection. The output of the photodiode is then amplified by a current amplifier (FEMTO current amplifier, DLPCA-200). The transform from the output of the current amplifier to the atom number is derived as below.

When atoms fall through the detection beam, the instantaneous fluorescence signal collected by the photodiode is given by:

$$\begin{aligned} V(t) &= G \times I(t) \\ &= G \times \frac{\eta \times dN_{photon} \times \hbar\omega}{dt} \end{aligned} \tag{3.3}$$

where G is the gain of the current amplifier, $I(t)$ is the photon current, η is the quantum efficiency (measured in A/W), dN_{photon} is the instantaneous photon number hitting on the photodiode and $\hbar\omega$ is the energy of single photon. Assuming the velocity of the atoms during the detection is stationary, the atom number in the probed state can be expressed as:

$$\begin{aligned} N &= \frac{\int dN_{photon}}{R_{sc} \times \tau \times A} \\ &= \frac{\int V(t)dt}{G \times \eta \times R_{sc} \times \tau \times \hbar\omega \times A} \end{aligned} \tag{3.4}$$

where R_{sc} is the scattering rate and τ is the duration of time when fraction of atoms stays in the detection beam and A is the solid angle of the detection window. Thus atom number is proportional to the area of the fluorescence signal. After substituting all the parameters into the above equation, we achieve N=332$\int V(t)dt$.

3.2.4 Experiment Control

To operate the experiment, all of the electronics should follow a precise timing sequence. Timing jitter when triggering the Raman pulses will induce additional phase shifts whilst atoms may be prepared in the wrong state if the laser is switched at the incorrect time. Therefore the core function of the control system is to generate a timing sequence, requiring a resolution down to a few nanoseconds with considerable stability.

The entire control system is based on a National Instruments sbRIO-9632 FPGA. A scripted program using Python generates the timing sequence. Although scripted programming is not as interface friendly as

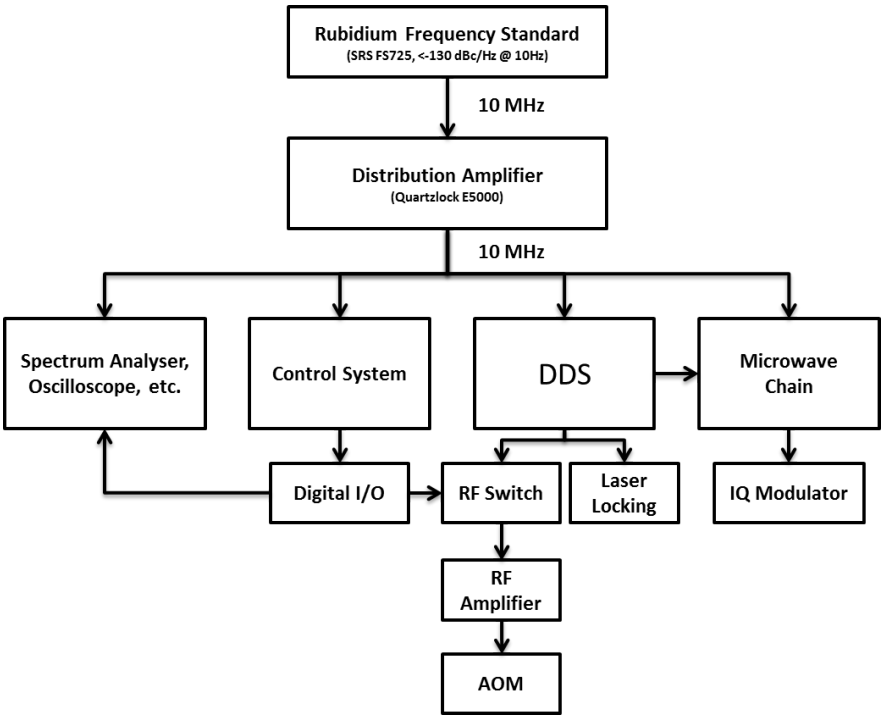

Figure 3.8: Schematics of the timing system.

Labview, it gives the flexibility to operate more complicated control flow. After configuring the sequence, it is loaded on a FPGA and then executed on the hardware in real time. A synchronous timing system is built specifically as shown in figure 3.8. The reference frequency originates from a Rubidium frequency standard (SRS, FS5725). A distribution amplifier is used to distribute this signal to multiple channels. Thus all of the electronics is synchronized to the low noise 10 MHz frequency reference.

3.3 Atomic Fountain Results

The first step of the experiment is to load atoms into a magneto-optical trap and then launch them upwards into the interferometry region with the moving optical molasses. The crucial purpose of this step is to include as many atoms as possible in the atom interferometry sequence, enhancing the signal-to-noise ratio at the final outputs. We therefore need to achieve high loading rates and low temperature atom clouds. By achieving the first, the measurement bandwidth can be increased, whilst the second promotes slow expansion of atoms after launch, which allows more atoms to be addressed in the centre of the Raman laser.

3.3.1 MOT Characterisation

In the previous design, a two dimensional MOT (2D-MOT) was attached to the MOT chamber, which is a common method for achieving high loading rates in cold atom experiments [100]. However the maximum loading rate of 2.7×10^7 atoms/s achieved was insufficient. After running for years, we could only detect a weak fluorescence signal in the 2D-MOT chamber. Unable to solve the problem, we had to disconnect the 2D-MOT chamber to inspect it separately. Instead rubidium dispensers were installed to act as the atom source. In the following paragraph, the MOT is optimised with the newly-fitted dispenser. Some characteristics in terms of atom number and loading rate are presented.

During the MOT, atoms are cooled and trapped from a room temperature vapour directly. However there are various loss mechanisms that knock atoms out of the trapping region, for example the collisions with background gas. The number of atoms in the MOT ultimately saturates when an equilibrium between the loading process and the loss mechanisms is reached. To a good approximation, the dynamics of the MOT loading and loss are governed by the rate equation:

$$N = \frac{R}{\gamma}(1 - e^{-\gamma t}) \tag{3.5}$$

where N is the number of atoms in the trap, R is the loading rate into the MOT and γ is the loss rate due to collisions with all background gases [101]. Normally R is proportional to the background gas pressure, namely the rubidium gas released from the dispenser. But increasing the pressure also leads to increased collisional losses from the trap. We firstly optimise the current setting of the dispenser. The dependence on magnetic field gradient and cooling laser detuning is also inspected afterwards.

Dependence on the Dispenser Current

Fig. 3.9 shows the loading rates with varying dispenser currents, which is measured by collecting the fluorescence from the 3D-MOT and is then converted to an atom number. The optimal current is found to be 4.7 A, above which the loading rate would still increase but the steady state atom number would decrease due to a high background pressure. To preserve the lifetime of the dispenser, it is operated at 4 A for the data presented in the remainder of this work. With this current, 7.2×10^8 atoms are trapped after 3 seconds.

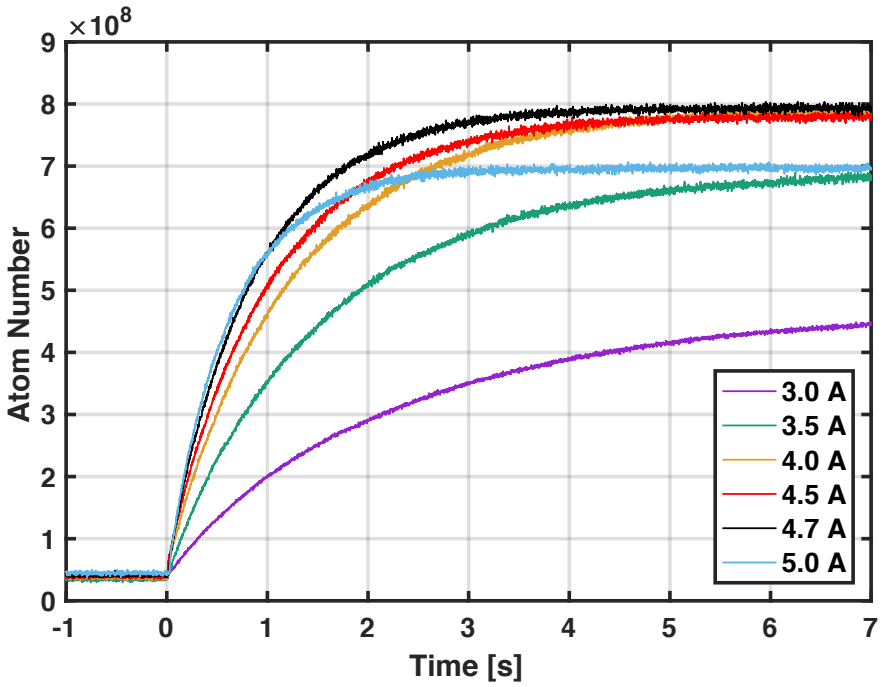

Figure 3.9: Estimated number of atoms loaded into the MOT as a function of time after the quadrupole field is turned on with different currents through the rubidium dispenser.

Dependence on the Magnetic Field Gradient

The effect of the magnetic field gradient is shown in Fig. 3.10a. The loading rate and the steady state atom number is extracted after fitting the loading curves with Equ.3.5. As the coil current increases, the loading rate increases at first while the steady state atom number is stable around 7.7×10^8. Both level off when the magnetic field gradient is between 10 G/cm and 12 G/cm. Then both the loading rate and the steady state number decrease if the current of coils is continually increased. These characteristics can be explained as below. For low magnetic field gradients, the trap depth is not deep enough to confine atoms. However in the case of high magnetic field gradients, the Zeeman shift at the edge of the beams is comparable with the detuning of the cooling beams from resonance, which degrades the cooling mechanism. In our experiment, the magnetic field gradient is chosen to be 11 G/cm. The corresponding coil current is 0.85 A.

Dependence on Detuning

For the cooling laser detuning, we can find a rise-and-fall in both loading rate and the steady state atom number, which is shown in the Fig. 3.10b. The argument above can also be employed to explain why the steady state number of atoms falls when the laser detuning is small. For large detuning, the scattering force

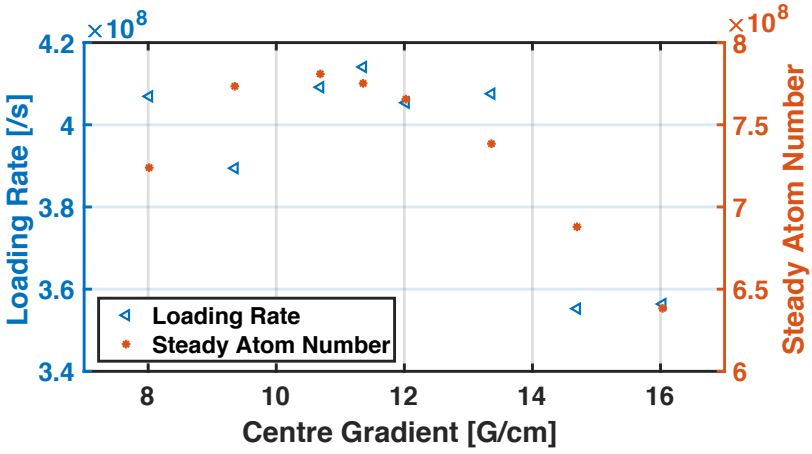

(a)

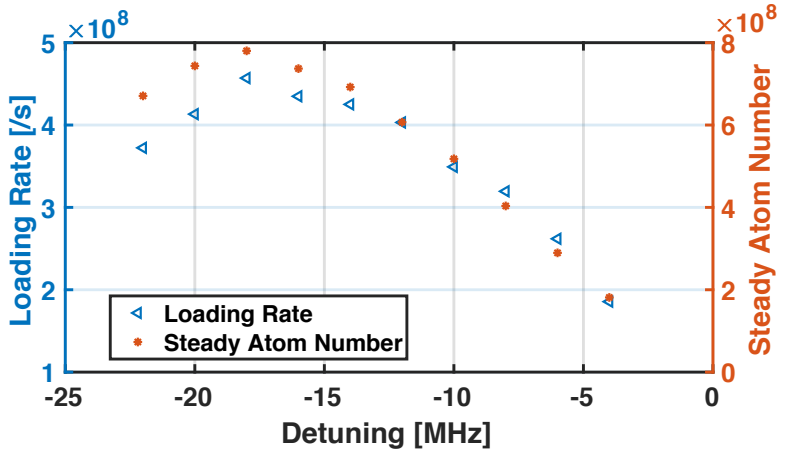

(b)

Figure 3.10: Dependence of loading rate and steady state atom number on MOT coil current (Fig. 3.10a) and cooling laser detuning (Fig. 3.10b).

is weak so that the number of atoms that can be captured decreases. In the experiment, the detuning of the cooling laser is set to be -18 MHz, where 8×10^8 atoms are achieved.

Telescopes Alignment

To estimate the cloud size, a CCD camera was set up to collect a fluorescence image of the cloud. The cloud size was measured at about 3mm in diameter. However a fringe across the cloud appears by accident as shown in Fig. 3.14, which is the result of spatially dependent polarisation gradient cooling [102]. Sisyphus cooling depends on the splitting between ground state sublevels which can have a beat pattern if the three pairs of trapping beams are not crossing at right angles. The varying cooling force is the reason for the interference fringes. As shown in Fig. 3.11b, correct alignment of the cooling beams can eliminate the fringe

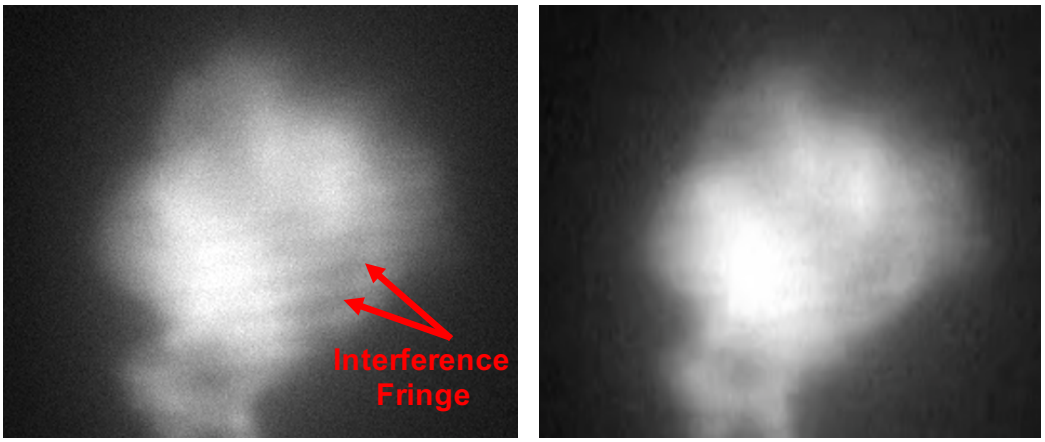

(a) (b)

Figure 3.11: Photos of interferometric fringe across the atomic cloud due to the misalignment of one pair of counter-propagating cooling laser beams (Fig. 3.11a). The interference is eliminated after improving the alignment (Fig. 3.11b).

over the cloud.

3.3.2 Atom Launching

After a consistent number of atoms, about 8×10^8, is loaded into the MOT, the atomic fountain is used to launch the atoms into the interferometer tube along a ballistic trajectory. The cut-view of MOT chamber for atom launching is shown in Fig. 3.12a and the launching sequence is shown in Fig. 3.12b. During the loading time, the six cooling beams are red-detuned by about 18 MHz (about -3Γ, where Γ is the line-width) from the $|F = 2\rangle \rightarrow |F^{'} = 3\rangle$ transition. When loading is complete, the quadrupole magnetic field is rapidly switched off. In the meantime, the beams' detuning is increased to -5Γ and last for 5 ms to reduce the temperature further by optical molasses. In order to accelerate the atoms upwards, a relative detuning between upper and bottom MOT beams of $\Delta\omega = 2\pi \times 2.4$ MHz is applied, which transfer the optical molasses state to a moving frame. Instead of adding the ultimate relative detuning at once, the relative detuning is added with a ramp, which is helpful to keep the atoms following adiabatically. After 2 ms, the beams detuning is further increased to -10Γ and the intensity is ramped down to zero during 3 ms. The repumping beam is kept on during the whole launch sequence and is left on for another 1 ms to pump all of the atoms into the $|F = 2\rangle$. According to Equ. 3.2, the launching velocity is 2.7 m/s. In the paragraph below, we assess the quality of the atomic fountain in terms of the temperature, launching efficiency and launch direction.

Temperature: It is subtle to optimise the temperature of molasses, which is determined by various factors, for example the background magnetic field, the beam intensity balance, timing sequence etc. In

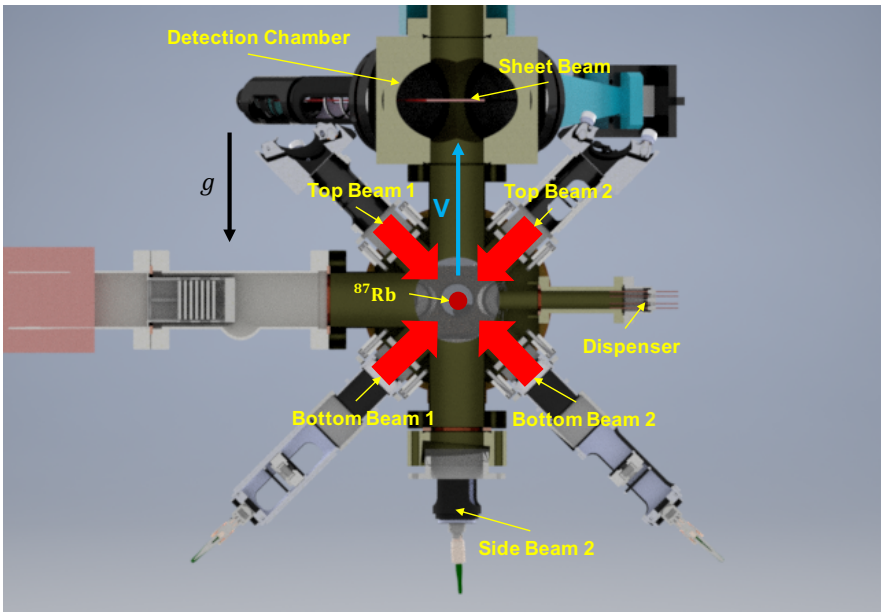

(a)

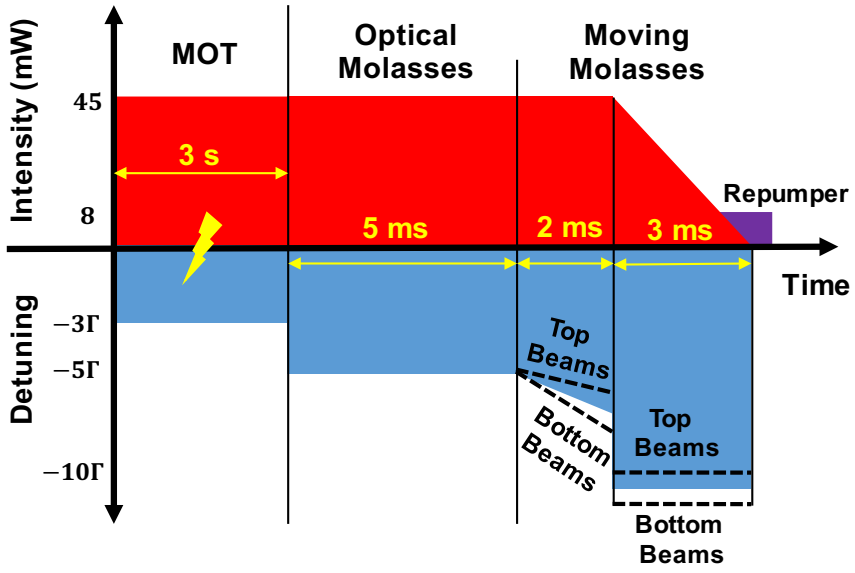

(b)

Figure 3.12: Figure 3.12a is the cut-view of atom launching in MOT chamber. The atoms are launched upwards by 2D moving molasses. The MOT beams are indicated except that the side beam 1 is not plotted in the figure. The state of the atoms can be detected when the atom cloud goes through the sheet beam in the detection chamber. The fluorescence emitted from atoms is probed by photodiode as presented in section 3.2.3. Figure 3.12b is the sequence of atom launching in the fountain. Horizontal dashed lines represent the different detuning for the top and bottom cooling laser. The time axis is not to scale.

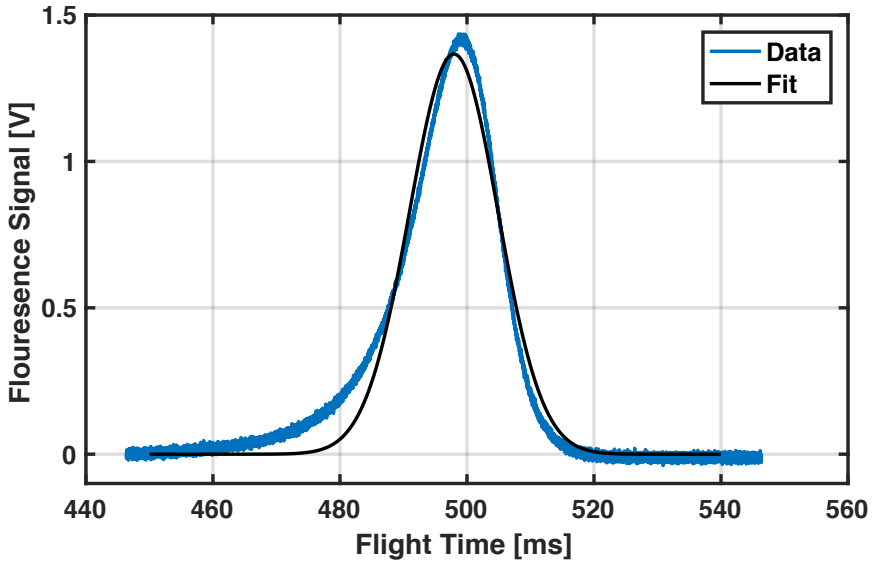

Figure 3.13: Fluorescence signal in time-of-flight when atoms are launched and fall through the detection laser on the way back. The atomic distribution is a Gaussian in the space and velocity domains.

fact, we have to experimentally inspect all the possible limitations to find an optimum. The measurement is performed by launching the atoms upwards and collecting the fluorescence at a certain height, where a slightly red detuned horizontal thin sheet beam is switched on. As the cloud expands during flight, the atomic density distribution is a Gaussian both in the space (x,y,z) and velocity domain (v_x, v_y, v_z). This can be written as:

$$n(t) = (\frac{m}{2\pi kT})^{3/2}\pi v_0^2(\frac{\frac{1}{2}gt^2 + l_0}{t^2})e^{-\frac{(\frac{1}{2}gt^2 - l_0)^2}{v_0^2 t^2}} \tag{3.6}$$

where l_0 is the distance from the MOT center to the sheet beam, g is the local gravity, $v_0 = \sqrt{2kT/m}$ is the most probable velocity, T is the cloud temperature, m is the atomic mass and k is the Boltzmann constant [103]. The temperature is extracted after fitting the fluorescence signal in time-of-flight as shown in Fig. 3.13. After optimising for quite some time, we achieved a minimum temperature of 9.5 μ K with a relative detuning of $\Delta\omega = 2\pi \times 2.4$ MHz.

Atom number: After submitting the fluorescence signal in Fig. 3.13 into the Equ. 3.4, we achieve the total atom number is $5{\times}10^6$.

Launching efficiency: To achieve higher interrogation times, we have to launch the atoms with a bigger relative detuning. However we find the launching efficiency decays when increasing the relative detuning. The TOF signal with varying relative detuning was measured and is shown in Fig. 3.14a, including the theoretical case for comparison. We also collect the fluorescence signal at 3 ms after launching by using a

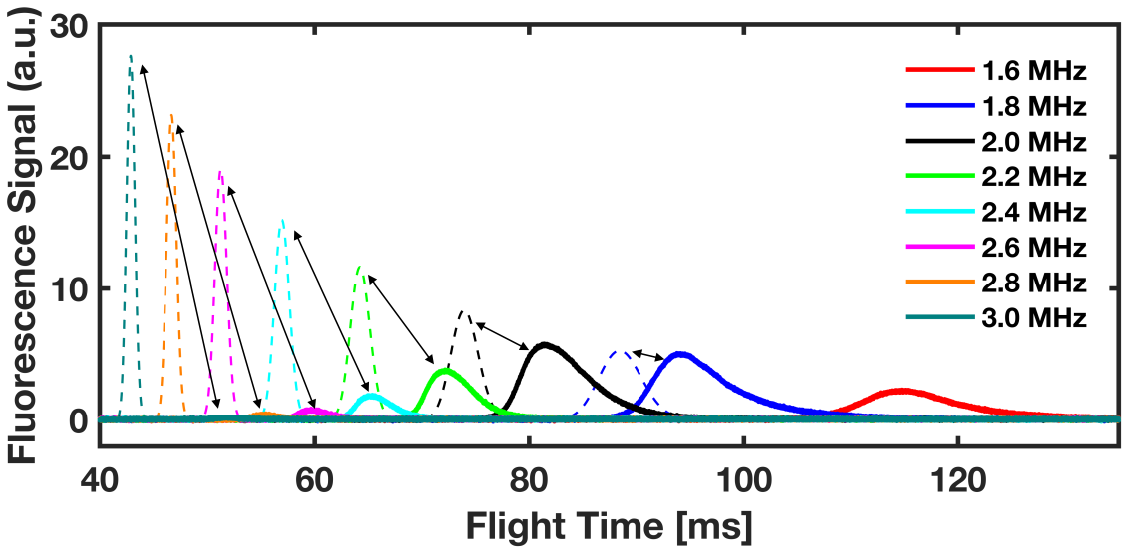

(a)

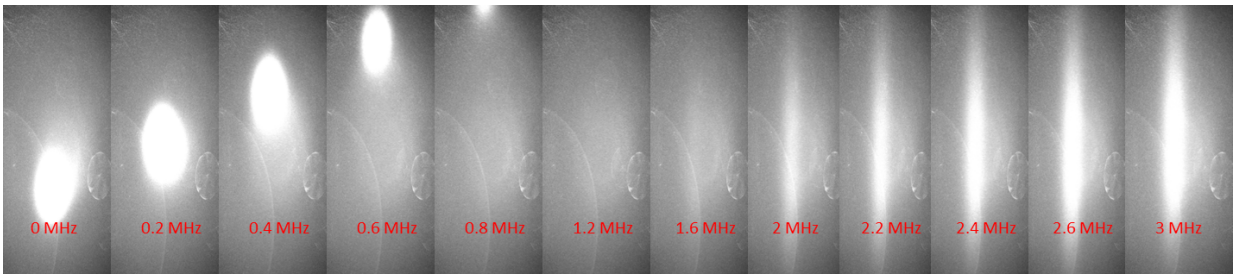

(b)

Figure 3.14: Launch atoms with varying relative detuning. Fig. 3.14a shows the fluorescence signal collected when atoms move upward (solid line) and its corresponding simulation (dotted line). The data for 1.6MHz coincides with the prediction, where the solid line and dotted line are overlapped. The data for other detuning is referred to the corresponding prediction by the double arrows. The residual atoms in the MOT chamber is probed by CCD camera 3ms after launching (Fig. 3.14b).

CCD to look from the side of the MOT chamber. Quite a lot of atoms are left in the chamber or lost along the path when the relative detuning is high. This is induced by the fact that the cooling laser beam size is limited by the 1 inch window. The effective accelerating distance is not long enough when the relative detuning is high so that moving molasses stop before some atoms are accelerated to the expected velocity.

Launch direction: The launch direction is inspected by tracing the cloud center during time-of-flight. A detection beam is incident vertically from the top of the system while a CCD camera is mounted on the bottom. Absorption images in x-y plane are collected at 20 ms, 25 ms, 30 ms and 35 ms after launching. The center is extracted after fitting the data with a Gaussian function. We repeat the measurement over 40 hours. Both the launching direction and long-term stability are inspected. The results are presented in

Fig. 3.15. In a single launch sequence, the centre of the cloud shifts by 0.2 mm along the x direction and 0.1 mm along the y direction within 15 ms. Assuming there is no horizontal acceleration, the velocities along the x and y directions are 13 mm/s and 6.7 mm/s along the x and y directions respectively. In addition, the center of the cloud is oscillating over time, the amplitude of which are 0.1 mm in x and 0.4 mm in y. This is induced by intensity drifts of the 6 cooling laser beams.

3.4 Summary

This chapter presented the construction and realization of the atomic fountain, which launches the atoms about 40 cm above the MOT centre. For higher launching, the efficiency is decreased, resulting in some atoms being left in the MOT chamber or lost along the path. Further improvement requires a higher power cooling laser with larger beam diameter, which enhances the effective cooling during the initial portion of the launch. The current setup is able to create atom clouds at a rate of 0.5 Hz with a temperature down to 10 μK, which paves the way for atom interferometry in next chapter.

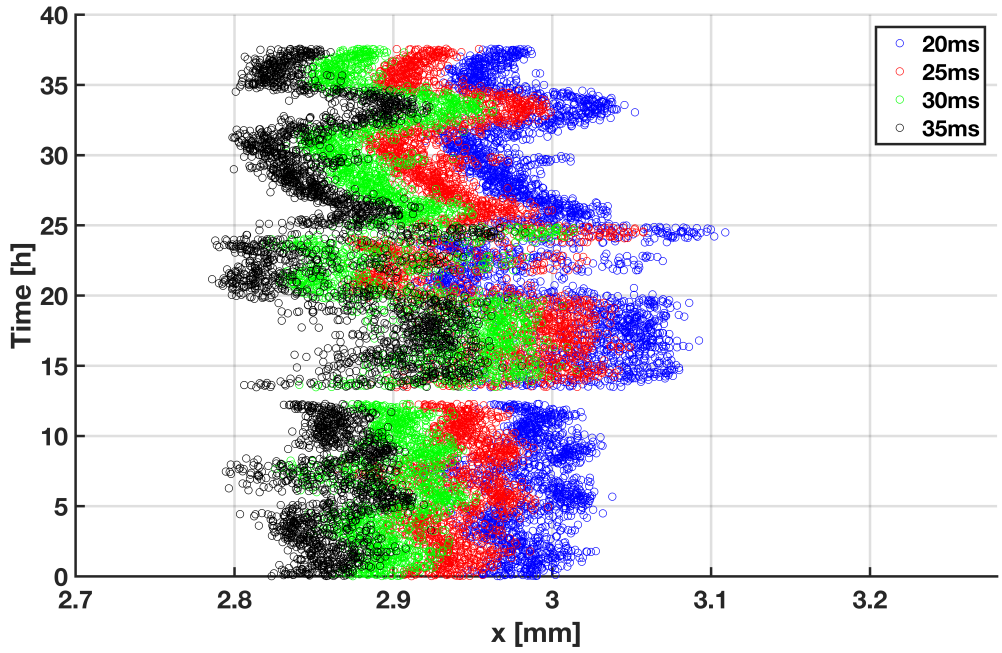

(a)

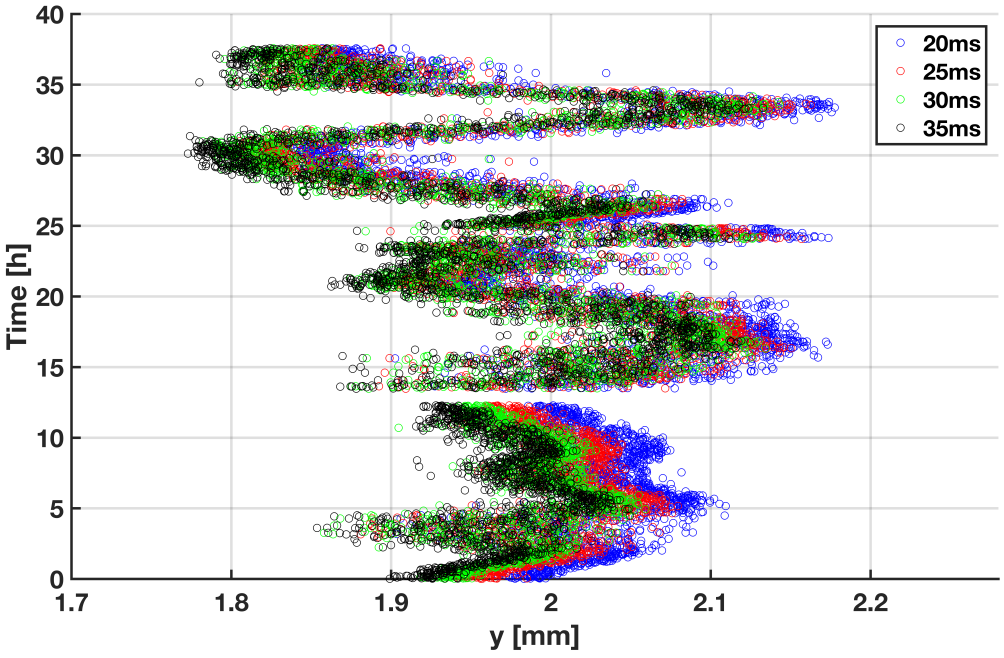

(b)

Figure 3.15: TOF measurement by absorption image in x-y plane. The centre of the cloud is extracted via fitting the image by Gaussian function. The measurement is repeated near 40 hours.

CHAPTER 4

RAMAN ATOM INTERFEROMETER

Atom interferometry with a Raman laser based on optical single-sideband (OSSB) will be presented in this chapter. The prime target is to achieve a sensitivity as high as possible, which is typically limited by the phase noise of the Raman laser and the vibration noise on the retro-reflection mirror. In this chapter, we will introduce the novel solutions developed within our experiment to suppress these effects, enabling higher sensitivity, and potentially allowing higher accuracy compared to existing approaches. This chapter will outline the OSSB approach, demonstrate its use within atom interferometry, and perform initial characterisation of its performance alongside characterisation of the gravimeter system.

The first section will focus on building an IQ modulator based OSSB laser system for the Raman laser. This technique not only supplies a light source for the coherent manipulation of atoms but also eliminates the residual effects arising from redundant sidebands. In this thesis, we combine the OSSB with second harmonic generation (SHG) to extend the spectrum coverage. Thus integrated devices based on fibre components in the telecom C-band can be employed in the experiment. The characteristics of the OSSB and its non-linear optical frequency mixing counterpart are derived in theory and measured in experiment. In the second section, a commercial passive vibration isolator is employed. In order to attenuate the perturbation from the environment, a shield box is made to promote the performance of the platform. We realize atom interferometry with the Raman laser based on OSSB. Some key results are presented, especially the atom interferometry fringe with an improved sensitivity. In the last, we compare atom interferometry when performed with the Raman laser based on the electro-optic modulator (EOM) and OSSB scheme. The emphasis is given on measuring the spatially dependent Rabi frequency and the interferometer phase shift.

4.1 Raman Laser

In atom interferometers, the Raman laser is usually implemented through optical phase locking (OPLL), acousto-optic modulators (AOM) or electro-optic modulator (EOM). In the OPLL scheme, the relative phase of two separate lasers is locked to an ultra-low noise reference oscillator by an optical phase-lock loop [104, 105, 106, 107]. However, this scheme usually requires the slave laser with high modulation bandwidth to achieve low relative phase noise and inherently higher complexity, worse reliability and compactness. Additionally, the phase servo system needs to be carefully designed to achieve low residual phase noise and wide locking bandwidth of the OPLL [108]. The AOM scheme is usually simpler and more robust than OPLL. Nevertheless, this scheme usually has a relative limited range of frequency shifting and lower efficiency [109]. Another feasible method is to create the Raman laser beams with phase modulation technique, such as EOM. Due to the phase-coherence between the modulated frequency components, the phase-modulated lasers have the advantage of low phase noise without the aid of OPLL. However, the EOM scheme usually produces a double sideband (DSB) spectrum which contains redundant sidebands. These redundant sidebands not only waste the optical power but also introduce extra undesirable interactions which adversely interferes with the systems normal operation and impairs the performance. As a consequence, the Rabi frequence is spatially depedent [94] and extra phase shifts are produced [110]. Althougth the redundant sidebands can be suppressed by introducing an optical filter [111], it unavoidably complicates the system. Comparing with aforementioned schemes, the full-carrier optical single sideband scheme (FC-OSSB) essentially preserves the advantages of aforementioned schemes as most of the complexity is offloaded to the microwave subsystem, which is more manageable. Furthermore due to the suppression of the redundant sidebands, the spatially interference in EOM scheme can be resolved.

4.1.1 Optical Single Sideband Modulation

The FC-OSSB is based on a dual-parallel Mach-Zehnder phase modulator (MZM) [113, 114], which is essentially an optical analogy of a Hartley modulator well known in microwave industry. The simplified architecture of the dual-parallel MZM is illustrated in Fig. 4.1. Two sub-MZMs, MZM_1 and MZM_2, are joined to form MZM_3. Each arm of the MZMs essentially works as a single phase modulator. MZM_1 and MZM_2 are respectively driven by V_I and V_Q which are essentially the same modulation signal with a relative phase difference ϕ_e. $\mathrm{MZM}_{1,2}$ are biased by $V_{DC_{1,2}}$ which induce $\pm\phi_{1,2}$ between the arms of $\mathrm{MZM}_{1,2}$. In the same manner MZM_3 is biased with V_{DC_3} that introduces an optical phase delay ϕ_3 between MZM_1 and MZM_2. Assume the seed laser is $E_0 e^{i\omega_c t}$ and a modulation signal ω with modulation depth β, the output can be expressed

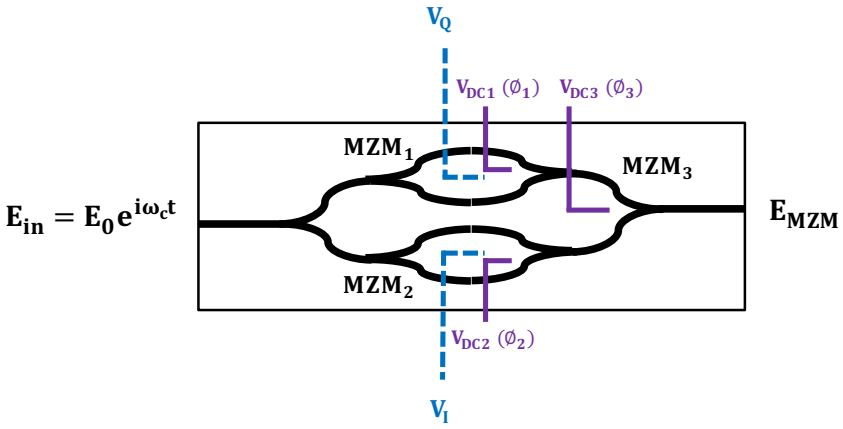

Figure 4.1: Illustration of the architecture of an IQ modulator with dual-parallel nested Mach-Zehnder interferometer waveguide (black), RF electrodes (blue, dashed) and DC electrodes (purple, solid)(modified according to the datasheet [112]). The modulator is fed by a monochromatic laser beam, which is split into two sub-MZMs, MZM_1 and MZM_2. Two RF driving signals V_I and V_Q with a relative phase difference ϕ_e separately modulate the laser beam and create sidebands in each sub-MZM. DC voltages, DC_1, DC_2 and DC_3, induce the optical phase delay in the corresponding sub-MZM.

by Bessel functions:

$$\begin{aligned}
E_{MZM} &= E_1 + E_2 + (E_3 + E_4)e^{i\phi_3} \\
&= \frac{E_0}{\sqrt{2}} e^{i\omega_c t}(e^{i(\beta\sin(\omega t+\phi_e)+\phi_1)} + e^{-i(\beta\sin(\omega t+\phi_e)+\phi_1)} + e^{i(\beta\sin(\omega t)+\phi_2+\phi_3)} + e^{-i(\beta\sin(\omega t)+\phi_2-\phi_3)}) \\
&= \sum_{-\infty}^{\infty} \frac{E_0}{\sqrt{2}} J_n(\beta) e^{i(\omega_c t+n\omega t)} e^{i(\phi_1+n\phi_e)} + \sum_{-\infty}^{\infty} \frac{E_0}{\sqrt{2}} J_n(\beta) e^{i(\omega_c t+n\omega t)} e^{i(-\phi_1+n\phi_e+n\pi)} \\
&\quad + \sum_{-\infty}^{\infty} \frac{E_0}{\sqrt{2}} J_n(\beta) e^{i(\omega_c t+n\omega t)} e^{i(\phi_2+\phi_3)} + \sum_{-\infty}^{\infty} \frac{E_0}{\sqrt{2}} J_n(\beta) e^{i(\omega_c t+n\omega t)} e^{i(-\phi_2+\phi_3+n\pi)} \\
&= \frac{E_0}{\sqrt{2}} J_0(\beta) A_0 e^{i\omega_c t} + \frac{E_0}{\sqrt{2}} \sum_{n=1}^{\infty} J_n(\beta) A_n e^{i(\omega_c t+n\omega t)} + \frac{E_0}{\sqrt{2}} \sum_{n=1}^{\infty} (-1)^n J_n(\beta) B_n e^{i(\omega_c t-n\omega t)}
\end{aligned} \tag{4.1}$$

with the coefficients A_n and B_n defined as below:

$$\begin{aligned}
A_n &= e^{i(\phi_1+n\phi_e)} + e^{i(-\phi_1+n\phi_e+n\pi)} + e^{i(\phi_2+\phi_3)} + e^{i(-\phi_2+\phi_3+n\pi)} \\
B_n &= e^{i(\phi_1+n\phi_e)} + e^{i(-\phi_1+n\phi_e+n\pi)} + e^{i(\phi_2+\phi_3)} + e^{i(-\phi_2+\phi_3+n\pi)}
\end{aligned} \tag{4.2}$$

where E_n is the optical field at each arm, $J_n(\beta)$ is the nth order of Bessel function and β is the modulation index. For simplicity, assume small modulation index ($\beta \ll 1$) and n=4, the output is simplified as:

$$\begin{aligned} E_{MZM} = \frac{E_0}{\sqrt{2}}[&J_0(\beta)A_0 e^{i\omega_c t} \\ &+ J_1(\beta)A_1 e^{i(\omega_c+\omega)t} - J_1(\beta)B_1 e^{i(\omega_c-\omega)t} \\ &+ J_2(\beta)A_2 e^{i(\omega_c+2\omega)t} + J_2(\beta)B_2 e^{i(\omega_0-2\Omega)t} \\ &+ J_3(\beta)A_3 e^{i(\omega_c+3\omega)t} - J_3(\beta)B_3 e^{i(\omega_c-3\omega)t} \\ &+ J_4(\beta)A_4 e^{i(\omega_c+4\omega)t} + J_4(\beta)B_4 e^{i(\omega_c-4\omega)t}] \end{aligned} \tag{4.3}$$

The corresponding optical power of each sidebands is list as follow:

$$\begin{aligned} P_0 &= 2E_0J_0^2(\beta)(\cos^2(\phi_1)+\cos^2(\phi_2)+2\cos(\phi_1)\cos(\phi_2)\cos(\phi_3)) \\ P_{+1} &= 2E_0J_1^2(\beta)(\sin^2(\phi_1)+\sin^2(\phi_2)+2\sin(\phi_1)\sin(\phi_2)\cos(\phi_3-\phi_e)) \\ P_{-1} &= 2E_0J_1^2(\beta)(\sin^2(\phi_1)+\sin^2(\phi_2)+2\sin(\phi_1)\sin(\phi_2)\cos(\phi_3+\phi_e)) \\ P_{+2} &= 2E_0J_2^2(\beta)(\cos^2(\phi_1)+\cos^2(\phi_2)+2\cos(\phi_1)\cos(\phi_2)\cos(\phi_3-2\phi_e)) \\ P_{-2} &= 2E_0J_2^2(\beta)(\cos^2(\phi_1)+\cos^2(\phi_2)+2\cos(\phi_1)\cos(\phi_2)\cos(\phi_3+2\phi_e)) \\ P_{+3} &= 2E_0J_3^2(\beta)(\sin^2(\phi_1)+\sin^2(\phi_2)+2\sin(\phi_1)\sin(\phi_2)\cos(\phi_3-3\phi_e)) \\ P_{-3} &= 2E_0J_3^2(\beta)(\sin^2(\phi_1)+\sin^2(\phi_2)+2\sin(\phi_1)\sin(\phi_2)\cos(\phi_3+3\phi_e)) \\ P_{+4} &= 2E_0J_4^2(\beta)(\cos^2(\phi_1)+\cos^2(\phi_2)+2\cos(\phi_1)\cos(\phi_2)\cos(\phi_3-4\phi_e)) \\ P_{-4} &= 2E_0J_4^2(\beta)(\cos^2(\phi_1)+\cos^2(\phi_2)+2\cos(\phi_1)\cos(\phi_2)\cos(\phi_3+4\phi_e)) \end{aligned} \tag{4.4}$$

where the coefficients A_n and B_n are extended. In a typical FC-OSSB modulation based on a 90° hybrid coupler ($\phi_e = \frac{\pi}{2}$), -1st order and +3rd order sidebands are effectively suppressed, i.e. $P_{-1} = 0$ and $P_{+3} = 0$ [115]. In this case, the below equations should be satisfied: $\phi_1 = \phi_2 = \phi$ and $\phi_3 = \phi_e = \frac{\pi}{2}$. Substituting these constraints into Equ. 4.4, the optical power of all the sidebands are simplified as below:

$$\begin{aligned} P_0 &= 4E_0J_0^2(\beta)\cos^2(\phi) & & \\ P_{+1} &= 8E_0J_1^2(\beta)\sin^2(\phi) & P_{-1} &= 0 \\ P_{+2} &= 4E_0J_2^2(\beta)\cos^2(\phi) & P_{-2} &= 4E_0J_2^2(\beta)\cos^2(\phi) \\ P_{+3} &= 0 & P_{-3} &= 8E_0J_3^2(\beta)\sin^2(\phi) \\ P_{+4} &= 4E_0J_4^2(\beta)\cos^2(\phi) & P_{-4} &= 4E_0J_4^2(\beta)\cos^2(\phi) \end{aligned} \tag{4.5}$$

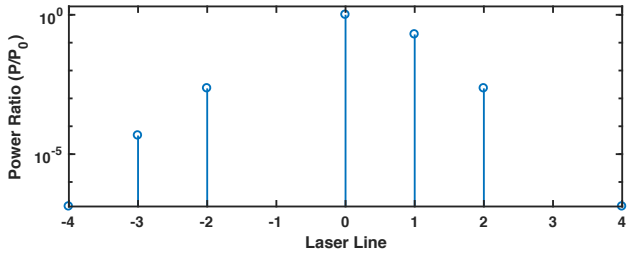

Figure 4.2: Stem plot of the power ratio of sidebands in respect to the carrier according to Equ. 4.5. The y axis is in log scale. In the calculation, β=0.6 and $\phi = \pi/4$.

After substituting β=0.6 and $\phi = \pi/4$ into above equations, we achieve $P_1/P_0 = 1.98$ and $P_2/P_0 = P_{-2}/P_0 = 0.002$. As shown in Fig. 4.2, all the other sidebands are less than 10^{-4} in respect to the carrier.

OSSB Combining with Sum-Frequency Generation

The spectral coverage of OSSB can be further extended to where there are no convenient light sources or modulators available by non-linear optical processes such as second harmonic generation (SHG). In our experiment, the OSSB modulator operates on 1560 nm wavelength light. The output is then converted into 780 nm by SHG to resonate with ^{87}Rb D_2 line. A periodically poled lithium niobate ridge waveguide (PPLN RW) is employed for the conversion. Unlike other non-linear processes, SHG of OSSB will unavoidably degrade the OSSB because of the self-mixing characteristics, which pairs the different frequency components of OSSB and creates undesired frequencies. The optical field of the self-mixing signal of Equ. 4.1 can be expressed as [116]:

$$
\begin{aligned}
E_{780} \quad &\propto E_{MZM}^2 \\
&= \frac{E_0^2}{2} J_0^2(\beta) A_0^2 e^{j2\omega_c t} \\
&\quad + E_0^2 \sum_{n=1}^{\infty} J_0(\beta) J_n(\beta) A_0 A_n e^{j(2\omega_c + n\omega)t} \\
&\quad + E_0^2 \sum_{n=1}^{\infty} (-1)^n J_0(\beta) J_n(\beta) A_0 B_n e^{j(2\omega_c - n\omega)t} \\
&\quad + \frac{E_0^2}{2} \sum_{n=2}^{\infty} \sum_{l=1}^{n-1} J_l(\beta) J_{n-l}(\beta) A_l A_{n-l} e^{j(2\omega_c + n\omega)t} \\
&\quad + \frac{E_0^2}{2} \sum_{n=2}^{\infty} \sum_{l=1}^{n-1} (-1)^n J_l(\beta) J_{n-l}(\beta) B_l B_{n-l} e^{j(2\omega_c - n\omega)t} \\
&\quad + E_0^2 \sum_{n=2}^{\infty} \sum_{l=1}^{n-1} (-1)^l J_l(\beta) J_{n-l}(\beta) B_l A_{n-l} e^{j(2\omega_c + (n-2l)\omega)t}
\end{aligned}
\tag{4.6}
$$

The Cauchy product is applied in the above derivation to simplify the expression.[1] The first term corresponds to the SHG of the carrier frequency itself, which is the most common application of the PPLN RW. The second and third terms are the SHG combining the carrier and one of the sidebands. The terms in blue,green and red correspond to the SHG between any two of the sidebands. In the FC-OSSB modulation based on a 90° hybrid coupler, -1st and +3rd order sidebands are cancelled when setting $\phi_1 = \phi_2 = \phi$ and $\phi_3 = \phi_e = \frac{\pi}{2}$. Substituting these constraints and the assumption n=4 into Equ. 4.6, the optical field after the PPLN RW can be simplified as:

$$\begin{aligned}
E_{PPLN} \propto (&\frac{E_0^2}{2} J_0^2(\beta) A_0^2 + E_0^2 J_2(\beta) J_2(\beta) B_2 A_2) e^{j2\omega_c t} \\
&+ (E_0^2 J_0(\beta) J_1(\beta) A_0 A_1) e^{j(2\omega_c+\omega)t} \\
&+ (E_0^2 J_2(\beta) J_1(\beta) B_2 A_1) e^{j(2\omega_c-\omega)t} \\
&+ (E_0^2 J_0(\beta) J_2(\beta) A_0 A_2 + \frac{E_0^2}{2} J_1(\beta) J_1(\beta) A_1 A_1) e^{j(2\omega_c+2\omega)t} \\
&+ (E_0^2 J_0(\beta) J_2(\beta) A_0 B_2 - E_0^2 J_3(\beta) J_1(\beta) B_3 A_1) e^{j(2\omega_c-2\omega)t} \\
&+ (\frac{E_0^2}{2} J_1(\beta) J_2(\beta) A_1 A_2 + \frac{E_0^2}{2} J_2(\beta) J_1(\beta) A_2 A_1) e^{j(2\omega_c+3\omega)t} \\
&- (E_0^2 J_0(\beta) J_3(\beta) A_0 B_3) e^{j(2\omega_c-3\omega)t} \\
&+ (E_0^2 J_0(\beta) J_4(\beta) A_0 A_4 + \frac{E_0^2}{2} J_2(\beta) J_2(\beta) A_2 A_2) e^{j(2\omega_c+4\omega)t} \\
&+ (E_0^2 J_0(\beta) J_4(\beta) A_0 B_4 + \frac{E_0^2}{2} J_2(\beta) J_2(\beta) B_2 B_2) e^{j(2\omega_c-4\omega)t}
\end{aligned} \tag{4.8}$$

It is shown in above equation, both the carrier and sidebands have terms contributed by the SHG of FC-OSSB. The -1st order sideband after PPLN RW is non-zero any more, which is generated by the SHG of the -2nd and +1st order sidebands of FC-OSSB. The SHG of the +1st and +2nd order sidebands of FC-OSSB creates the +3rd order sideband after PPLN RW. In order to suppress these unwanted sidebands, the modulation index β and DC bias voltages need to be set carefully.

Simulation

We assume the optical power ratio (OPR) between the +1st order sideband and the carrier at 780 nm (after PPLN RW) is 1/2, i.e. -3 dB. With the proposed FC-OSSB scheme above, the OPRs of the sideband-to-

[1] Cauchy product: For the power series $\sum_{n=1}^{\infty} a_n x^n$ and $\sum_{n=1}^{\infty} b_n x^n$, their product can be modified as

$$(\sum_{n=1}^{\infty} a_n x^n)(\sum_{n=1}^{\infty} b_n x^n) = \sum_{k=2}^{\infty} (\sum_{j=1}^{k-1} a_j b_{k-j} x^k) \tag{4.7}$$

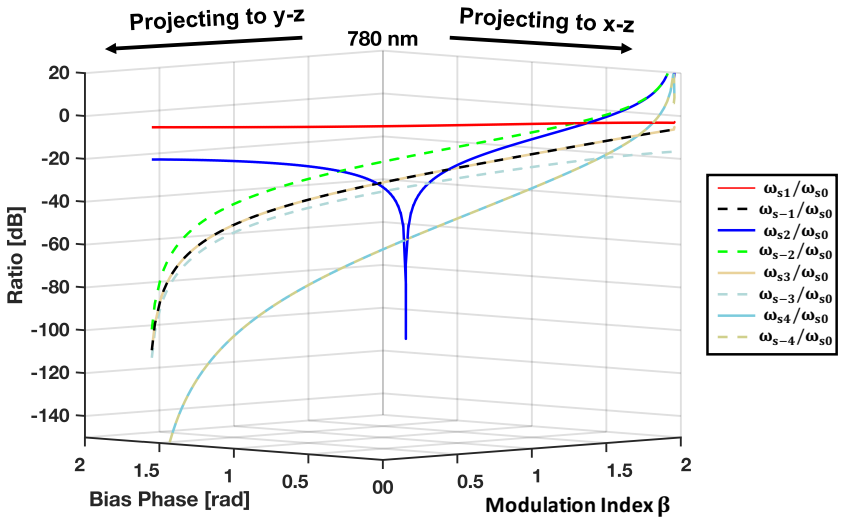

(a)

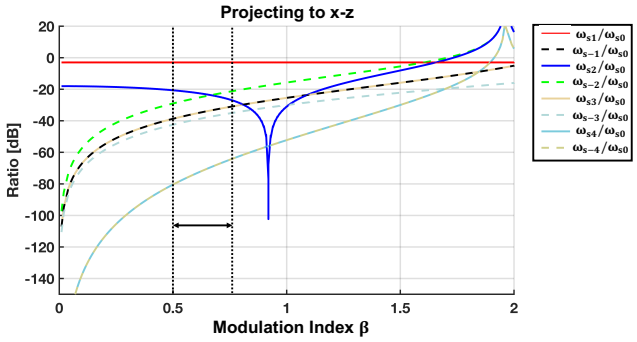

(b)

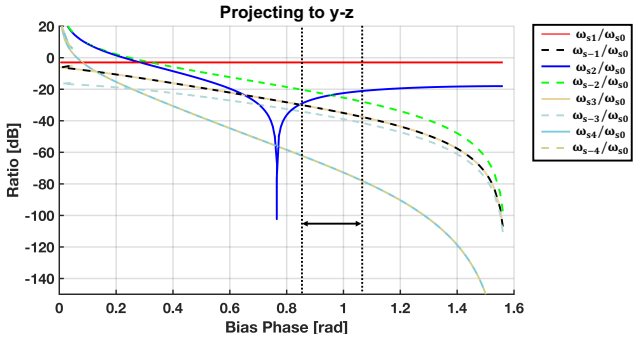

(c)

Figure 4.3: The sidebands ratio referred to the carrier at 780 nm as a function of the Bessel cofficients and bias phase when the ratio of +1st to carrier is fixed to be -3dB. Fig. 4.3c and 4.3b are the projection of the Fig. 4.3a onto the x-z and y-z planes respectively. The carrier and nth order sideband after PPLN RW is ω_{s0} and ω_{sn} respectively.

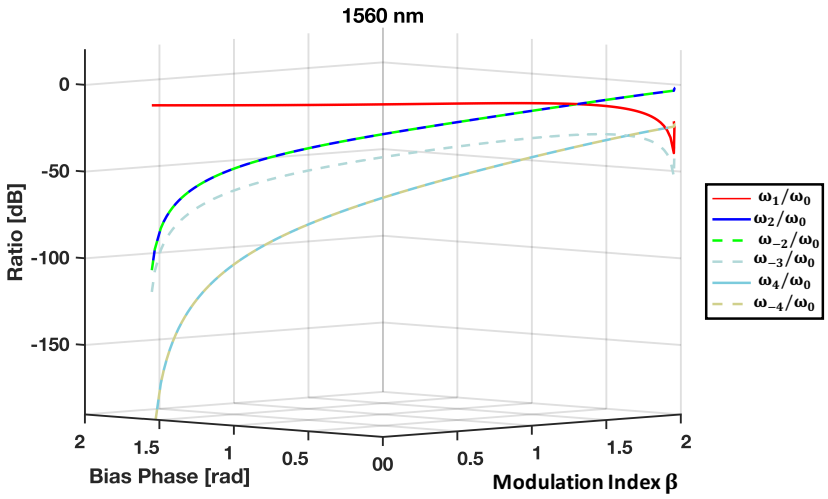

Figure 4.4: The sidebands' ratio referred to the carrier at 1560 nm as a function of the Bessel cofficient and bias phase when the ratio of +1st to carrier at 780 nm is fixed to be -3 dB.The carrier and nth order sideband in OSSB is ω_0 and ω_n respectively.

carrier are simulated as a function of the bias phase ϕ and the modulation index β. The result is plotted in Fig. 4.3a. For visual display, we change the orientation of the figure axes and project the curves on x-z (Fig. 4.3b) and y-z (Fig. 4.3c) respectively.

From the above figures, in order to suppress all the -1st, +2nd and -2nd order sidebands below -20 dB, the modulation index β is limited between 0.5 and 0.7 and the corresponding bias phase ϕ is limited between 1.05 and 0.84 rad. If we intentionally suppress the -1st order sideband as low as possible, the +2nd order sideband will increase to a saturated value at -18.06 dB. With the same conditions as above, the OPRs of the sideband-to-carrier in FC-OSSB (1560 nm, before PPLN RW) are also plotted in Fig. 4.4. Since the -1st and +3rd order sidebands are cancelled, they are not plotted in the figure. With the same setting of the bias phase and modulation index as above, the +1st order sideband is -9 dB while both the -2nd and +2nd order sidebands are suppressed between -38 dB and -26.5 dB. The other higher order sidebands are much lower.

Broadband Frequency Shifter

One by-product of the OSSB technique is that the above laser system can also work as an agile optical frequency shifter. Generally the optical frequency shift can be achieved through AOM and serrodyne modulation. The AOM is very mature but the limitations are the lower efficiency and a small frequency shift range, i.e. tens MHz. The serrodyne modulation [117, 118] provides a very convenient way to shift the optical frequency. Nevertheless, the achievable largest frequency shift is about 1.4 GHz and the best efficiency was

about 80% which are limited by the microwave non-linear-transmission-line (NLTL), aka comb generator [118]. Multiple NLTLs are also needed to cover different frequency shifts. Contrary to these two frequency shift schemes, the suppressed carrier optical single sideband (SC-OSSB) scheme is very simple and versatile. If substituting $\phi_3 = \phi_e = \pi$ and $\phi_1 = \phi_2 = \frac{\pi}{2}$ into Equ. 4.3 and 4.8, we can also achieve SC-OSSB at both 1560 nm and 780 nm:

$$E_{MZM} = -2\sqrt{2}E_0 J_1(\beta)e^{j(\omega_0+\Omega)t} + 2\sqrt{2}J_3(\beta)e^{j(\omega_0-3\Omega)t} \tag{4.9}$$

$$E_{PPLN} \propto 8E_0^2 J_1(\beta)J_1(\beta)e^{j(2\omega_0+2\Omega)t} - 16E_0^2 J_3(\beta)J_1(\beta)e^{j(2\omega_0-2\Omega)t} \tag{4.10}$$

It is shown that the SC-OSSB is independent of the driving modulation index, meaning that we do not need to over-drive the modulator to achieve carrier suppression. The frequency shift range is limited by the bandwidth of the modulator which can be as high as 20 GHz for commercial products and the suppression of the carrier and undesirable sidebands can achieve better than 20 dB.

4.1.2 Raman Laser Setup

Due to the advanced development of the telecommunication industry, high-power and robust laser components for near-infrared wavelength are widely available. Especially, with the aid of the non-linear wavelength conversion processes like SHG, telecommunication wavelength lasesr can be converted to the rubidium D_2-line wavelength, opening the gates to utilize the telecom laser for rubidium experiments [119]. In our lab, few experiments have accumulated abundant experience in building frequency doubled fibre laser system for cold atom experiments. In Clemens Rammeloo's thesis [120], a compact frequency doubled fibre laser system has been built for both laser cooling and atom interferometry. The multiple frequency components are generated by EOM. In order to suppress the unwanted laser frequency, we build the Raman laser system based on OSSB which comprises a 1560 nm fibre laser and a dual-arm Mach-Zehnder (MZ) IQ modulator. The diagram of the setup is illustrated in Fig. 4.5. The 1560 nm seed laser is an erbium-doped fibre laser (NKT Photonics, Koheras BASIK E15), which has a narrow linewidth (2 kHz) and high passive frequency stability. The optical carrier with optical power 14 dBm is injected to a fibre IQ modulator (Photline, MXIQ-LN-40) to generate the OSSB. Two RF driving signals are supplied by a microwave chain, which will be described in below section. Because of the insertion loss and destructive interference of the optical power between arms, only about 2 dBm is output from the IQ modulator. An erbium-doped fibre amplifier (EDFA) from Orion Laser (YEDFA-PM) has to be employed before the wavelength conversion. The module is principally chosen for its low input

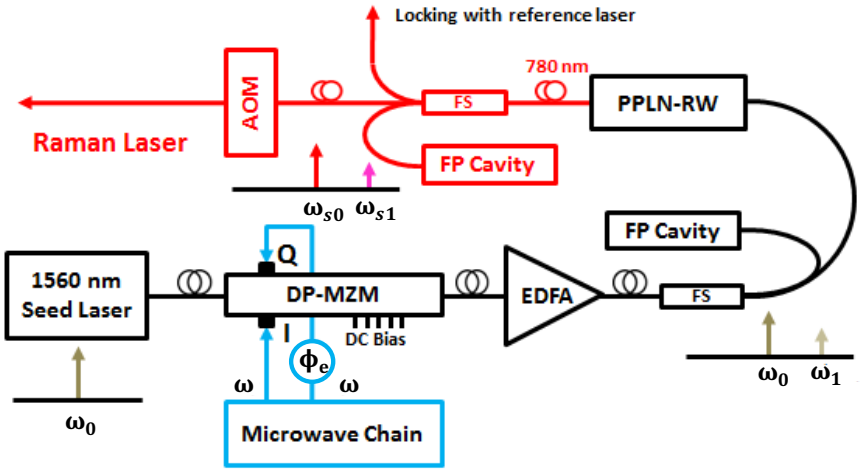

Figure 4.5: Diagram of the Raman laser system. The optical components in black and red indicate the laser frequency in 1560 nm and 780 nm respectively. FS: fibre splitter; EDFA: erbium-doped fibre amplifier; PPLN RW: periodically poled lithium niobate crystal waveguide; FP Cavity: Fabry-Perot cavity; AOM: acousto-optical modulator;

power limit ($\geq$ -10 dBm) and high amplification gain. Optical power at 1560 nm can be amplified up to 33 dBm. Afterwards a PPLN RW in a small fibre coupled package (WH-0780-000-F-B-C, NTT Electronics) is used to convert 1560 nm wavelength laser to 780 nm wavelength laser. Considering the damage threshold of PPLN RW crystal, the optical power of the input laser is limit below 30 dBm. The optical power of 780 nm light is approximately 440 mW. In order to monitor the laser spectrum, a fraction of light before and after the PPLN RW are led into Fabry-Perot cavities (FP cavity) by fibre splitters. Another fraction of the laser, after PPLN RW, is divided to beat with reference laser for frequency stabilizing. The performance of all the components except the IQ modulator has been analysed comprehensively in the thesis [120]. Here we mainly examine the spectrum of OSSB combining with SHG as well as its modulation bandwidth.

Raman Laser Spectrum

The spectrum before and after the PPLN RW is measured by two FP cavities, whose free spectral range (FSR) are 10 GHz (Thorlabs, SA210) and 1.5 GHz (Thorlabs, SA200) respectively. Here we define the carrier and nth order sideband in OSSB is ω_0 and ω_n respectively while the carrier and nth order sideband after PPLN RW is ω_{s0} and ω_{sn}. The shorthand for the different frequency components is as:

$$\begin{aligned} \omega_n &= \omega_c + n\omega \\ \omega_0 = \omega_c, \omega_1 &= \omega_c + \omega, \omega_{-1} = \omega_c - \omega ... \end{aligned} \tag{4.11}$$

and $'s'$ is added to the subscript to refer the components:

$$\begin{aligned} \omega_{sn} &= 2\omega_c + n\omega \\ \omega_{s0} &= 2\omega_c, \omega_{s1} = 2\omega_c + \omega, \omega_{-1} = 2\omega_c - \omega ... \end{aligned} \tag{4.12}$$

As shown in Fig. 4.3a, the amplitude of these unwanted sidebands depends on the setting of the modulator. To optimize the 780 nm FC-OSSB, we start from its counterpart at 1560 nm by adjusting ϕ_3 and observing the suppression pattern of the different frequency components such as ω_{-1} and ω_0. Further optimization is achieved by adjusting $\phi_{1,2}$. Subsequently, the power and the spectrum of 780 nm OSSB are adjusted primarily through the modulation depth β but also $\phi_{1,2}$. Eventually the temperature of the wavelength conversion module is adjusted to shift the gain profile and finish the optimization. Fig. 4.6a and 4.6b show the spectrum of FC-OSSB in 1560 nm and its self-mixing signal in 780 nm respectively. The RF driving signals, I and Q, are set at 6.834 GHz. The FC-OSSB spectrum shown are acquired with a power ratio ω_{s1}/ω_{s0}, at -3 dB at 780 nm, as desired for compensating light shifts. The ω_{s-1} is not visible and the ω_{s2} is approximately 21 dB below ω_{s0}. Meanwhile, concerning the 1560 nm components, the ω_{-1} is suppressed better than 20 dB compared with ω_0. The other higher order sidebands are much smaller and can be neglected. In the measurement, the RF power applied to the I/Q ports of the modulator is 13 dBm which corresponds to $\beta \approx 0.74$ based on the $V_\pi = 6$ V. From the simulated result in Fig. 4.3b, the corresponding OPR of ω_{s2}/ω_{s0} should be around -30 dB, which is -9 dB lower than the measured data. This is because the OPR of ω_1/ω_0 is higher than the simulated result. Thus the SHG term $\frac{E_0^2}{2} J_1(\beta) J_1(\beta) A_1 A_1 e^{i(2\omega_c + 2\omega)t}$ increases the optical power at ω_{s2}. The degeneration can be explained by the unbalanced RF power applied on the I and Q ports and the non-identical waveguides on the two arms of the modulator.

The I/Q modulator is also used to realize SC-OSSB. Fig. 4.6c shows the spectrum of SC-OSSB in 1560 nm. The ω_0 is suppressed to the noise level. Nevertheless the extinction ratio of ω_{-1} is only better than -16 dB with respect to ω_1. According to the Equ. 4.6, the SHG between ω_1 and ω_{-1} will generate a laser line proportional to $-E_0^2 J_1(\beta) J_1(\beta) B_1 A_1 e^{i(\omega_1 + \omega_{-1})t}$, the frequency of which is equal to ω_{s0}. Thus the suppression of ω_{s0} at 780 nm is considerably impaired. The revival of the carrier at 780 nm is clearly seen in Fig. 4.6d. The ω_{s0} is only -16 dB compared with the frequency at ω_{s2}. Meanwhile, the ω_{s1} amplitude is beneath the noise level.

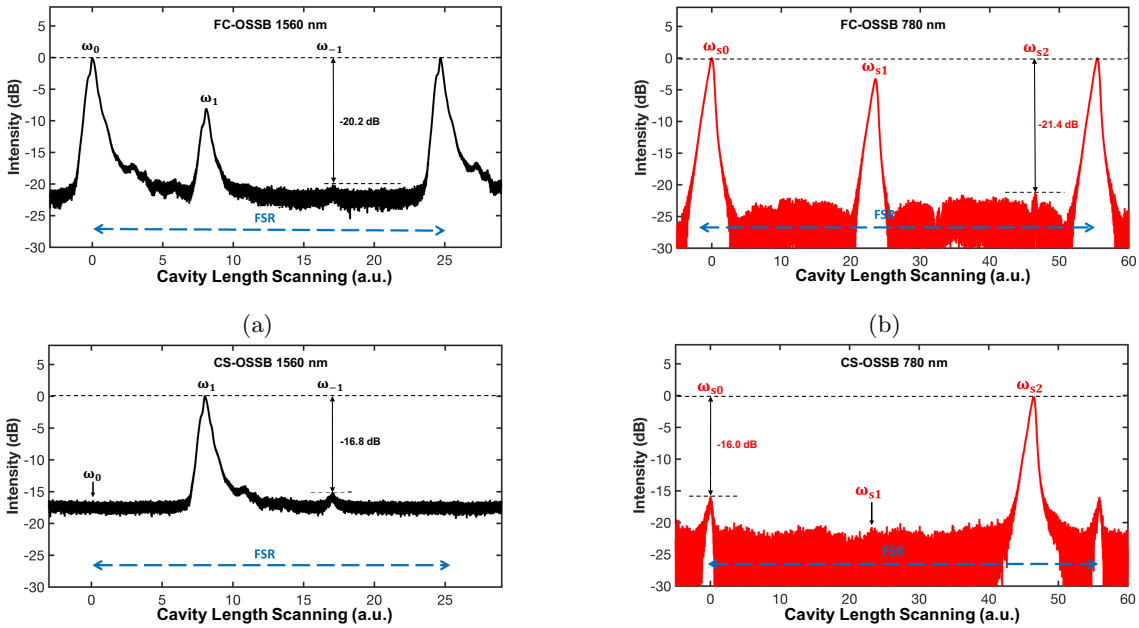

Figure 4.6: Spectrum of FC-OSSB (Fig. 4.6a and 4.6b) and SC-OSSB (Fig. 4.6c and 4.6d). The spectrum is measured before (black) and after (red) the PPLN respectively. Each figure is plotted in logarithmic scale. The observed laser lines are labelled at the corresponding positions. The FSRs of cavities are marked by the blue dash lines.The FC-OSSB spectra shown are acquired with a power ratio ω_{s1}/ω_{s0}, at -3 dB at 780 nm, as desired for compensating light shifts.

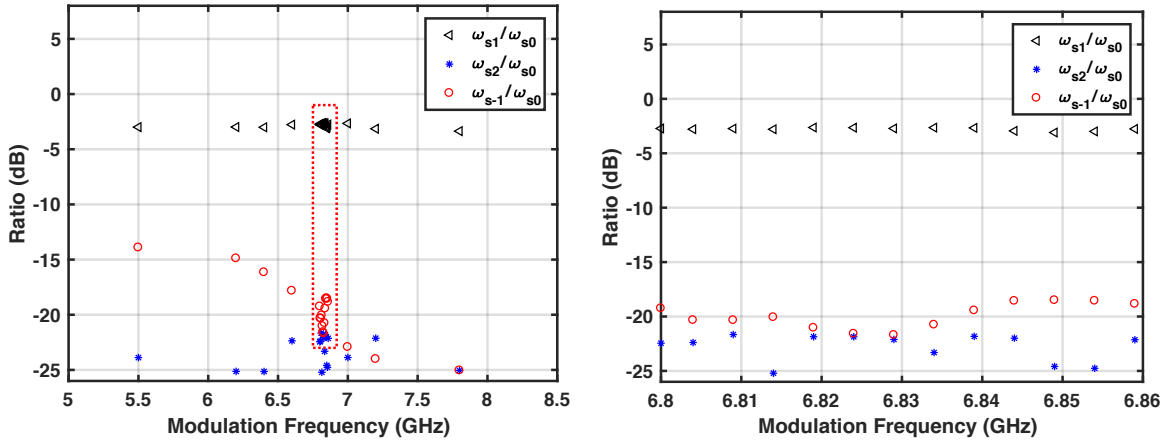

Figure 4.7: The 780 nm sideband ratio verse the modulation frequency. The ratio ω_{s1}/ω_{s0} is to -3 dB at 6.834 GHz. The subfigure (b) is the red dash boxed region in (a).

Modulation Bandwidth

In the gravity measurement with atom interferometry, the Raman laser is chirped to cancel the Doppler shift. During the chirping, the OPR of the +1st order sideband ω_{s1} to carrier ω_{s0} should maintain the ratio to eliminate the AC stark shift whilst the unwanted sidebands need to be suppressed low enough all the time to reduce the Raman transition driven by other laser pairs. The tuning of RF driving signal ω may produce unwelcome side effects such as degradation of suppression and power ratio variation of ω_{s0}/ω_{s1}. These would primarily be caused by the frequency dependent characteristics of the microwave electronics driving the I/Q modulator. The dependence of the FC-OSSB performance with ω_m was investigated, and the results for ω_m within 4–8 GHz are shown in Fig. 4.7a. Figure 4.7b shows the enlarged region covering the experimental frequency chirping for Doppler shift compensation. During scanning, the OPR of ω_{s1}/ω_{s0} is set to be -3 dB. The sideband ω_{s2} can be suppressed below -20 dB between 5 GHz and 8 GHz while the suppression of the sideband ω_{s-1} starts to increase below 6.8 GHz. This is because the RF devices have a frequency-dependent phase shift, which degrades the OSSB. However, for the range between 6.8 GHz and 6.86 GHz where the atom interferometer operates, the sideband ω_{s-1} is suppressed below -18 dB.

4.1.3 Microwave Chain

A frequency reference chain is built to generate a low phase noise microwave source near 6.8 GHz to drive the IQ modulator. The schematic is shown in figure 4.8. The chain is based on a multiplied crystal oscillator (Wenzel, GMXO-PLD), which is highly integrated with multipliers to create 7 GHz from an oven-controlled

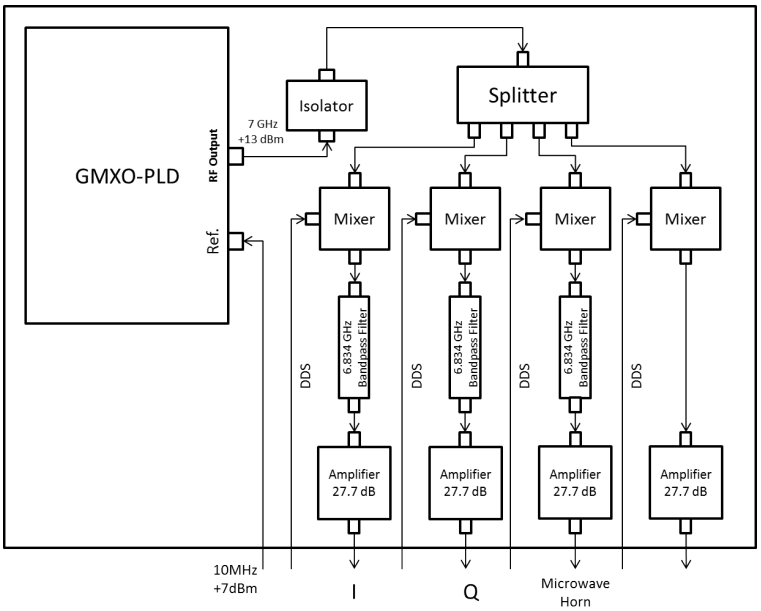

Figure 4.8: Schematics of the microwave chain.

crystal oscillator (OCXO). The module can be phase locked to an external frequency, which is 10 MHz from an atomic clock in our case. In the chain, the 7 GHz out of the GMXO-PLD is split into four channels, two for the IQ modulator, one for the microwave horn and the fourth is auxiliary. Each channel is able to mix with an external RF source like direct digital synthesizer (DDS) or arbitrary function generator (AFG). The down conversion frequency is filtered by a bandpass filter (ELHYTE, BP6834-70/T-5CS) before entering the amplifier. The RF phase noise and the corresponding Raman laser phase noise will be evaluated in section 5.2.3.

4.2 Vibration Control

A stable inertial reference is vital for absolute gravity measurement. The phase planes of the Raman laser works as an optical ruler to meter the relative acceleration of the free falling atoms in atom interferometry. However, in the retro-reflection geometry, vibration imposed on the retro-reflection mirror can induce phase noise, and even wash out the interferometry fringe. In fact, the inertial acceleration measured in the atom interferometry is the combination of the gravitational and vibrational acceleration. As a consequence of the equivalence principle, it is impossible to distinguish between gravitational fields and motion of inertial reference, namely the retro-reflecting mirror in our case. Therefore a vibration isolator is required. As a starting point, we purchased a passive vibration isolator (MinusK Technology,10BM-10). However, the

performance of the platform is degraded due to the perturbation from the environment. We at first searched for the main perturbation source in our lab and then formulated a usage scheme to enhance the isolation as well as possible.

4.2.1 Passive Vibration Isolator

The passive vibration isolator 10BM-10 has a payload range between 0-4.5 kg. Employing a patented mechanism using negative stiffness elements, the system can provide vibration isolation with a vertical resonance frequency of 0.5 Hz and a horizontal resonance frequency of 1.5 Hz [121]. Since the entire retro-reflection mirror setup is only 2.2 kg, extra load has to be added to tune the horizontal and vertical resonance frequency to the minimal. The residual acceleration on the platform is measured by two seismometers (Sercel geophone L4C seismometers). In order to identify the main vibration source present in our lab and test the performance of the passive vibration isolator, we deliberately set some specific scenarios to test. During the measurement, one L4C is positioned on the baseplate of the vibration isolator while the other one is placed on the floor next to the isolator. Fig. 4.9 shows the amplitude spectrum density (ASD) of the residual vibration in these specific scenarios.

Human Movements: When a human walks around the experiment, vibration on the floor ranges from 0.2 Hz and 100 Hz are all excited, especially between 0.2 Hz and 20 Hz. Although the passive vibration isolator can suppress noise quite a lot, residual vibration on the platform is still increased when there is human activity nearby, especially in the spectrum ranging from 0.1 Hz to 15 Hz, where our interferometer is most sensitive. As shown in Fig. 4.9a, an apparent spike appears at around 1.7 Hz on both the floor and isolator platform when human walks around. This should be the eigenmode frequency of the building.

Air Flow: When the vibration isolator works properly, the spring is adjusted quite soft (low stiffness). Thus even if air flow pass the isolator, it can perturb the isolator, resulting in strengthening the residual vibration on the isolator. As shown in Fig. 4.9b, after we housed the entire isolator setup with a box, the residual vibration was reduced, especially the spectrum region below 2 Hz. With the box, the vibration is amplified below 0.9 Hz and have a maximum amplification of 2 at resonance frequency. However, without the box, the amplification starts from 2 Hz and reaches the maximum amplification nearly 100 at resonance frequency.

Building Floor: The building typically has eigenstates at frequency ranging from 0.1 Hz to 2 Hz [88]. The plot of ASP in the lab (the second floor) and the ground floor of the building is shown in the Fig. 4.9c. The ground floor presents less vibration.

On the basis of the above results, a shield box is designed to enclose the passive vibration isolator setup,

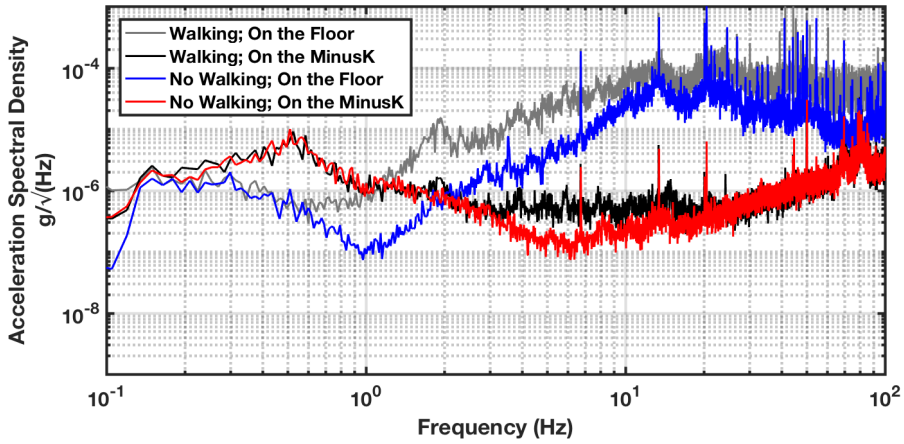

(a)

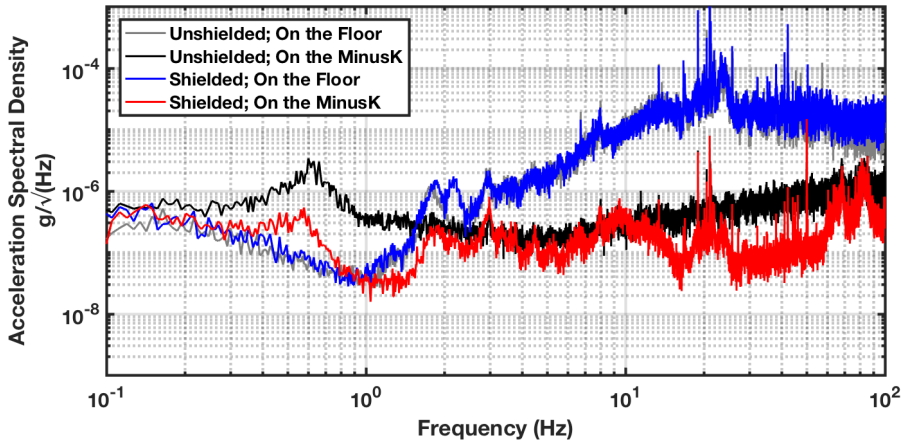

(b)

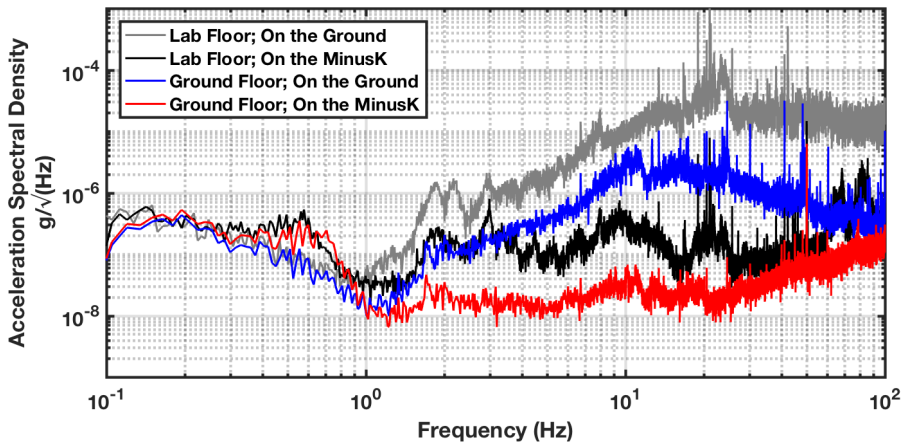

(c)

Figure 4.9: Power spectrum density of the vibration in specific scenes. In the measurement, one L4C is positioned on the baseplate of the vibration isolator while the other one is placed on the floor next to the isolator.

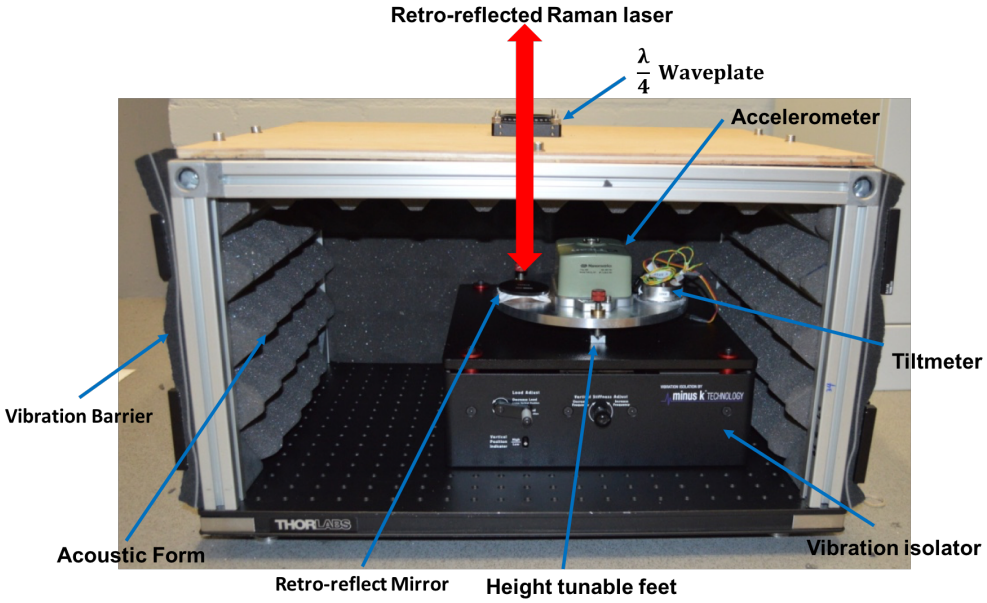

Figure 4.10: Photograph of the shield box which attenuates the perturbation from the environment. The vibration isolator platform is placed inside.

aiming to attenuate the perturbation from the environment in the lab. As shown in the Fig. 4.10, the entire house is built on a breadboard. Three speaker feet are mounted underneath the breadboard as the base of the stand. In order to reduce the vibration from air flow and acoustic noise, the walls of the box consist of lead barrier soundproofing and acoustic foams. On the top, a 2 inch hole is reserved for the optical access, which is covered by a 2 inch $\lambda/4$ waveplate.

4.3 Magnetic Field Control

The stray magnetic field can cause the atomic levels shift because of the Zeeman effect. This is one of the systematic errors in gravity measurement (see section 5.3.1). Alghouth the first order Zeeman shift can be eliminated via preparing atoms in magnetic insensitive state $m_F = 0$, the quadratic Zeeman effect is still present [84]. In order to attenuate the magnetic field, the entire interferometer tube is enclosed inside an assembly of three-stage magnetic shield, which is made of 1 mm thick high-permeability nickel-iron-molybdenum alloy. The shields are concentric cylinders and equally spaced. The innermost cylinder has a length of 660 mm and a diameter of 150 mm while the outermost is 680 mm long and 130 mm wide. All the shields sit on an acrylic plate, where three circle grooves are machined to fix the shields. Fig. 4.11 shows the residual magnetic flux inside the shields measured by magnetometer from Stefan Mayer Instruments

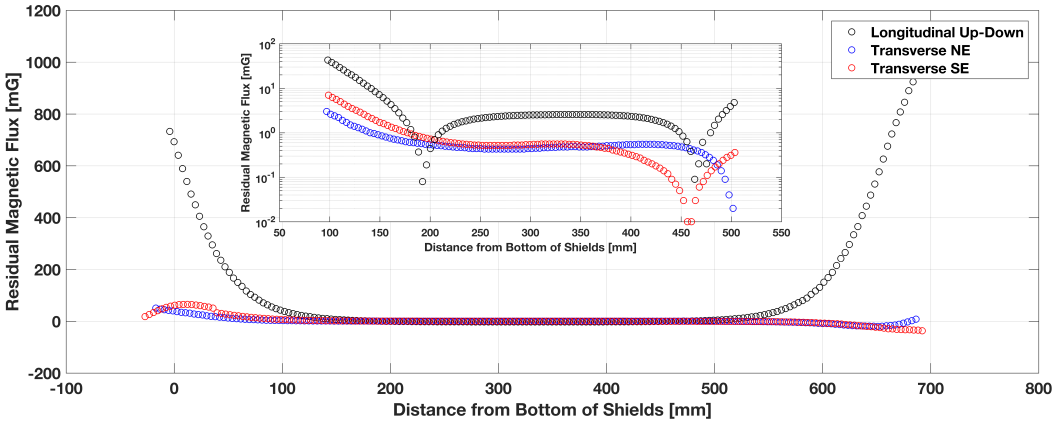

Figure 4.11: Residual field inside the magnetic shields. Sub plots inset shows the flux homogeneity between 10 cm and 40 cm from the bottom of the cylinder.

(Fluxmaster). The longitudinal residual magnetic flux along the cylinder axis is attenuated below 10 mG between 100 mm and 500 mm where the transverses magnetic flux along both North-East and South-East are below 1 mG.

In the atom interferometry, the quantization axis is provided by a solenoid wound on a Teflon cylinder surrounding the interferometer tube. Two helical groves with opposing direction of rotation are machined on the outer mantle of the Teflon cylinder, with which the exact position of coils winding is addressed. A laser driver is employed to supply the current for the coil. Fig. 4.12b shows the longitudinal and transverse magnetic flux inside the quantization coil. Between 100 mm and 400 mm, the fluctuation of the longitudinal residual magnetic flux is less than 10 mG whilst the transverse magnetic fluxes is below 10 mG and changes within 1 mG.

After assembling the magnetic shields and quantization coils, the magnetic field present in the interferometer region needs to be measured precisely again. This is because the phase shift induced by the second order Zeeman shift needs to be estimated quantitatively. In addition, the edge effects from both the magnetic shields and quantization coil redirect the magnetic flux. Spatially inhomogeneous magnetic fields can induce energy shifting, which employs additional acceleration on atoms. The detailed analysis will be present in Chapter 5.

(a)

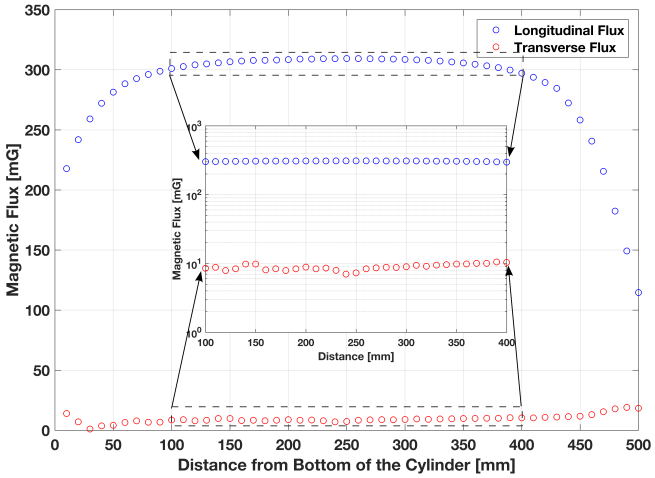

(b) Longitudinal and transverse flux of quantization coil measured along the axis of the cylinder. Sub plots inset shows the flux homogeneity between 10 cm and 40 cm from the bottom of the cylinder.

Figure 4.12: Photograph of the quantisation coil. The magnetic field inside the solenoid is measured when the current is 0.1 A.

4.4 Atom Interferometry Results

4.4.1 Raman Transition

Raman Laser Configuration

The basic principle of the Raman transition is presented in chapter 2. However, in order to drive the Raman transition effectively, few more conditions should be satisfied.

(1) To measure the gravity, the Raman laser beams need to be configured in counter-propagating configuration such that the Raman transition is velocity sensitive.

(2) The Doppler shift should be larger than the linewidth of Raman transition. After generated from the single-sideband modulation, the Raman laser beams are led into the vacuum chamber via the same fibre and then retro-reflected by the mirror on the vibration isolator. As shown in Fig. 4.13a, there are two pairs of counter-propagating Raman lasers existing in the vacuum chamber with opposite effective wavevector, ($\mathbf{k}_{11}$, $\mathbf{k}_{22}$) and ($\mathbf{k}_{12}$, $\mathbf{k}_{21}$). Since the Doppler shift is larger than the transition linewidth, only one pair can be in resonance and drive the two-photon Raman transition.

(3) The polarization of the Raman laser beams should be orthogonal. For a detuning bigger than the hyperfine

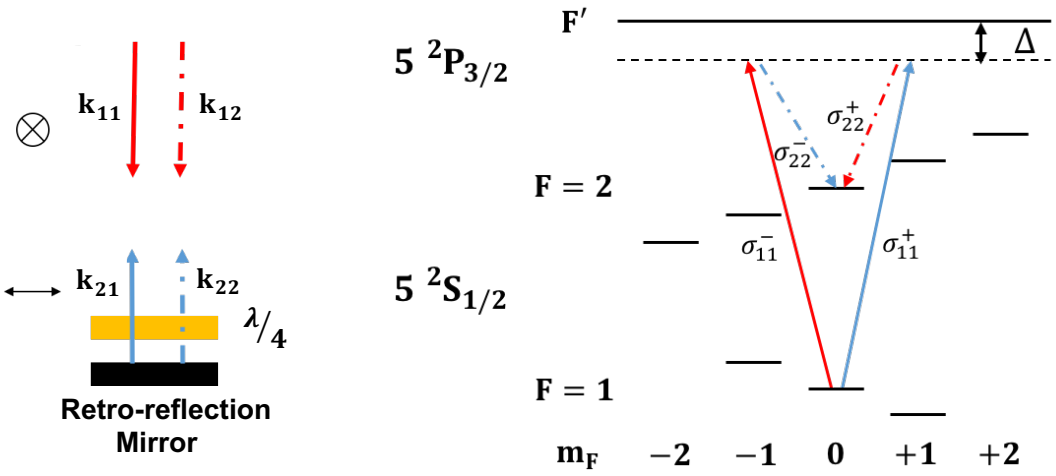

(a) (b)

Figure 4.13: Raman transition with counter-propagating laser beams.

splitting, the Rabi frequency is approximately given by[122]:

$$\Omega_{eff} \cong \frac{e^2}{4\hbar^2\Delta}[\mathbf{E}_1 \times \mathbf{E}_2^*] \cdot M \tag{4.13}$$

where M is the dipole matrix elements. To maximize the transition probability, the driving fields $\mathbf{E}_1$ and $\mathbf{E}_2$ must have orthogonal polarisation. In our experiment, the incident laser beams are of linear polarization. A $\lambda/4$ waveplate is inserted before the retro-reflecting mirror. Thus the incident laser beams pass through the $\lambda/4$ waveplate twice, which is equivalent to a $\lambda/2$ waveplate. We then rotate the waveplate until the polarization of the retro-reflected laser is converted into the orthogonal polarization of the incident laser. In the vertical quantization axis, the linear polarisation can be decomposed into circular polarisations.

$$\begin{aligned} k_{11} : x &= \frac{(x+iy)+(x-iy)}{2} \rightarrow k_{11} = \sigma_{11}^+ + \sigma_{11}^- \\ k_{22} : x &= \frac{(x+iy)-(x-iy)}{2} \rightarrow k_{22} = \sigma_{22}^+ + \sigma_{22}^- \end{aligned} \tag{4.14}$$

Thus there are four possible combinations which can drive the two photon Raman transitions, namely $\sigma_{11}^+ + \sigma_{22}^+$, $\sigma_{11}^+ - \sigma_{22}^-$, $\sigma_{11}^- + \sigma_{22}^+$ and $\sigma_{11}^- + \sigma_{22}^-$. Based on the dipole transition matrix, only the pairs $\sigma_{11}^+ + \sigma_{22}^+$ and $\sigma_{11}^- + \sigma_{22}^-$ are non-zero and contributes to the Raman transition [123].

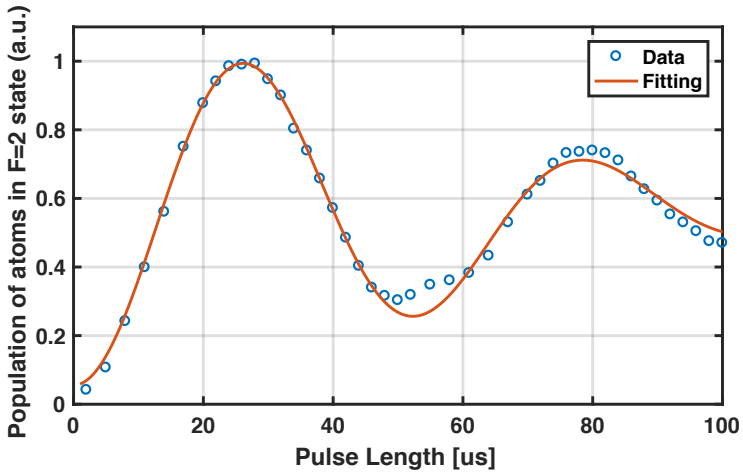

Figure 4.14: Rabi Oscillation in Doppler-sensitive configuration. The Rabi frequency is fitted to be 117 kHz.

Rabi Oscillation

We determine the π pulse duration in experiment. In the end of the moving molasses, atoms fall to the ground state $|F = 1\rangle$. After that atoms fly into the magnetic shields, where a Raman pulse is switched on. The atoms transmitted to the state $|F = 2\rangle$ will be detected in their way back to detection region. We measure the probability of transition as a function of the Raman pulse duration τ. The result is shown in Fig. 4.14. According to the data, we achieve τ_π=26 μs. We also notice that the amplitude of the oscillations diminishes as the pulse duration increases. This is because the thermal expansion of the atomic cloud degrades the coherence.

4.4.2 Velocity Selection and State Preparation

Although the atoms in optical molasses have been cooled to temperature below 10 μK. The finite temperature still corresponds to a velocity spread, where the Doppler broadening of the atomic resonance is wider than the linewidth of the Raman transition. Thus, in the velocity-sensitive Raman transition, atoms in different velocity classes are excited deconstructively, resulting in losing the fringe contrast in atom interferometry. On the other hand, after moving molasses sequence, the atoms are pumped into the state $|F = 2\rangle$. At that moment, the atoms are randomly distributed in all possible Zeeman sublevels. To minimize the effect of stray magnetic fields, only the atoms in the $m_F = 0$ sublevels are used. Therefore, prior to the atom interferometry sequence, a stage where the atoms are addressed into a very narrow velocity distribution and the internal state is prepared in magnetic-insensitive state $m_F = 0$, is vitally important. The entire process is illustrated in Fig. 4.15.

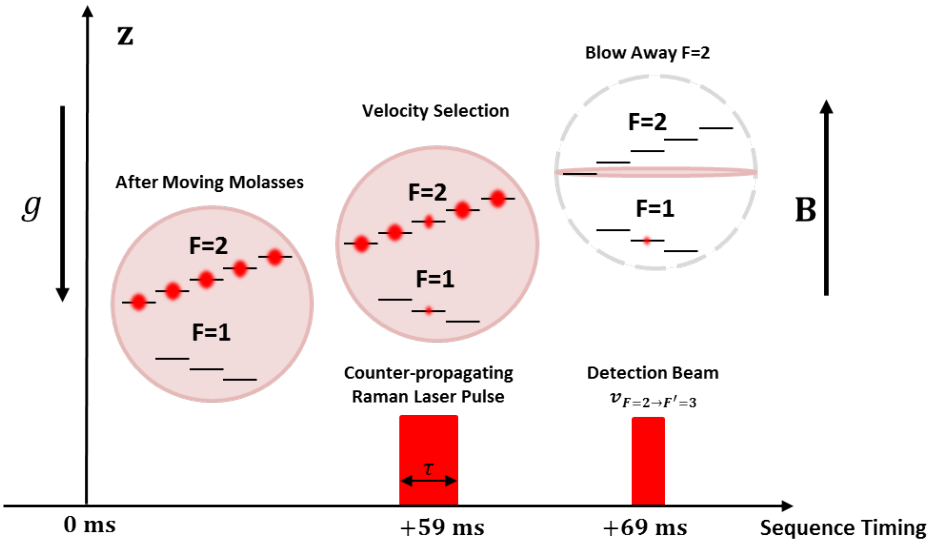

Figure 4.15: The visualization of the velocity selection and state preparation process.

The velocity selection is realized by stimulated Raman transition [124]. At 59 ms after moving molasses, the atoms fly into the detection chamber, where the Raman laser beams are applied. A certain group of atoms can be in resonant with the Λ transition $|F = 2\rangle \rightarrow |F = 1\rangle$ if the Doppler shift of their velocity component parallel to the Raman lasers exactly compensates the Raman laser detuning. Then the velocity spread of atoms transmitted to the state $|F = 1\rangle$ is given by the Doppler-shift formula $\Delta v/c = \Delta\nu/(\nu_1 + \nu_2)$, where $\Delta\nu$ is the linewidth of the Raman transition and $\nu_{1,2}$ is the frequency of the Raman laser beams. Due to the long lifetime between the two hyperfine states, the linewidth of the Raman transition is determined by the interaction time, namely the Fourier width of the Raman pulse duration τ, which is much narrower than the Doppler broadening of the atomic resonance. For atoms with velocity $\mathbf{v}$, the corresponding Doppler shift is $\delta_{Doppler} = \mathbf{k_{eff}} \cdot \mathbf{v}$. Then the vertical velocity spread Δv_z after the velocity selection is related to the width of the Raman transition by:

$$\Delta v_z = \frac{\Delta\delta_{Doppler}}{k_{eff}} = \frac{c \cdot \Delta\nu}{\nu_1 + \nu_2} \approx \frac{1}{\tau \cdot k_{eff}} \tag{4.15}$$

If τ is 50 μs, Δv_z is about 1.2 mm/s, which corresponding to a temperature of

$$T = \frac{m \cdot (\Delta v)^2}{k_B} \approx 15 \quad \text{nK} \tag{4.16}$$

where k_B is the Boltzmann constant and m is the atomic mass of rubidium. Atoms in different velocity

classes can also be selected by varying the frequency difference between the Raman lasers.

Fig. 4.16a shows the fluorescence signal when the atoms remaining in the state $|F = 2\rangle$ pass through the detection beam. The curve area is proportional to the atom number. The presence of a dip in the curve is interpreted as the amount of atoms being selected, with which we can count the selection efficiency. In recent velocity selection scheme, there are 3×10^5 atom is selected, corresponding to 5% of the total launched atoms (the atom number is calculated based on the Equ. 3.4). However the atoms are selected without any specific m_F sublevels addressed. In order to preselect the desired internal state, the magnetic field from the quantisation coil is added to remove the degeneracy among m_F sublevels. Sublevels in the state $|F = 2\rangle$ are split by $\Delta E = 0.7$ MHz/G$\cdot m_F$B [84]. By adjusting the frequency difference of the Raman lasers finely, only the atoms in state $|F = 2, m_F = 0\rangle$ are in resonance and transmitted into state $|F = 1, m_F = 0\rangle$. Other transitions, $|F = 2, m_F = -1\rangle \rightarrow |F = 1, m_F = -1\rangle$ and $|F = 2, m_F = 1\rangle \rightarrow |F = 1, m_F = 1\rangle$, can also be reached by tuning the Raman lasers. Fig. 4.16b shows the transitions of the above magnetic sublevles. However, because of the threefold degeneracy in hyperfine states, only one third of the atoms is selected at this stage compared with the case without the quantization coil. The red curve in Fig. 4.16a shows the fluorescence signal with the quantization coil on. There are 1.6×10^5 selected, corresponding to 2.6% of the total launched atoms.

After atoms are selected in the external and internal state, the remaining atoms in the state $|F = 2\rangle$ are blown away when they carry on flying past the horizontal detection beam. The lower part of the detection beam is not retro-reflected. Thus the excited atoms are exerted a force towards the chamber wall and pushed away from the flight direction. Finally only atoms addressed in the narrow velocity spread along the Raman lasers direction and in the internal state $|F = 1, m_F = 0\rangle$ remain. The spatial distribution of the atomic cloud is like a cigar as shown in the last stage in Fig. 4.15. Because the sensitivity of the atom interferometer is ultimately limited by shot noise due to the finite number of atoms, a more efficient state selection sequence is desirable. The initial atom number could be improved by incorporating optical pumping in the future. In other experiment, Zeeman state optical pumping is used to increase the atom number by a factor of three [125].

4.4.3 Interferometry Fringe

After velocity selection and state preparation, the remaining atoms carry on flying into the magnetically shielded region. A Mach-Zehnder atom interferometer is operated by employing three velocity sensitive Raman pulses($\pi/2$-π-$\pi/2$), which split, redirect and recombine the atomic wavepackets. The total laser

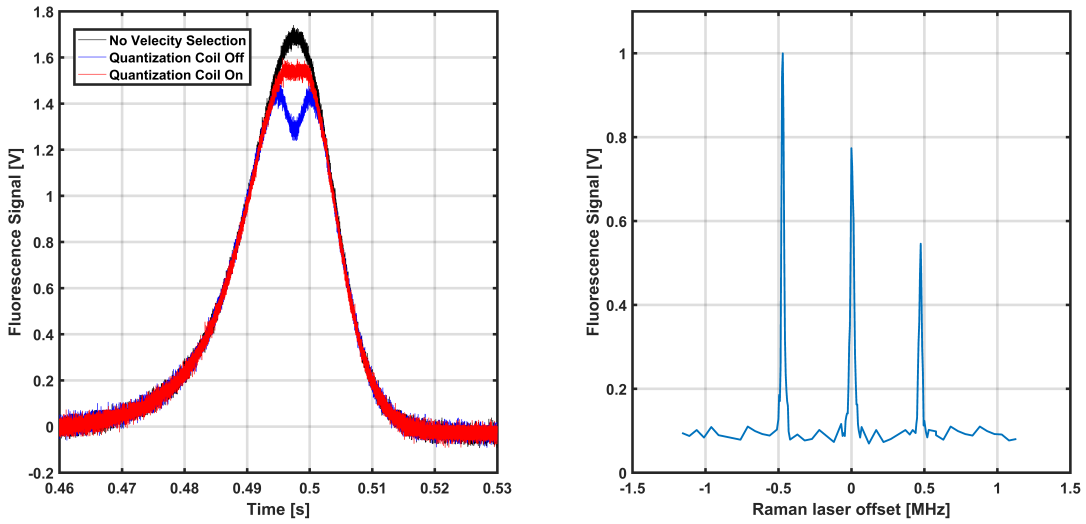

(a) (b)

Figure 4.16: Results of the velocity selection and the spectrum of sublevels.

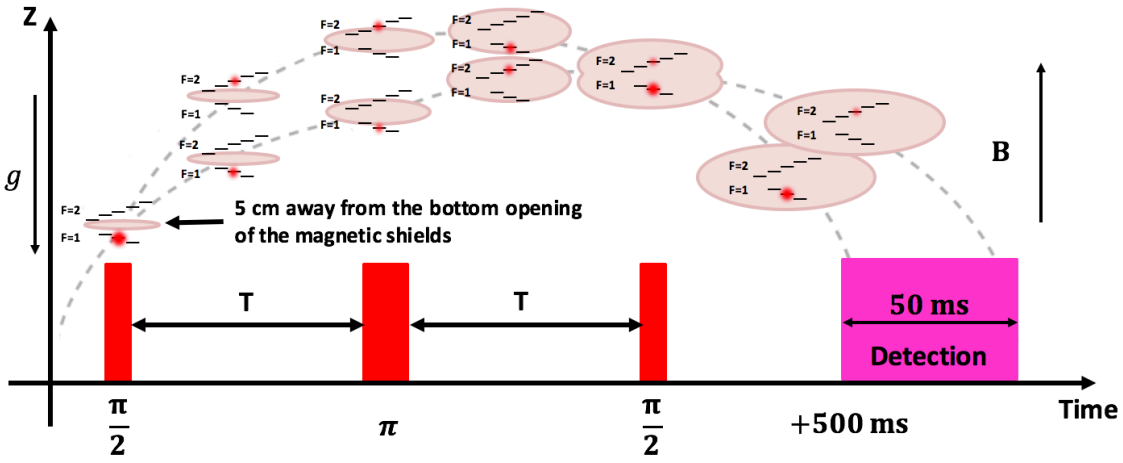

Figure 4.17: The sketch of the Mach-Zehnder atom interferometer sequence. During the flight, the atomic cloud expands freely, which is visualized by the area of the ellipse in pink. The evolution of the internal state is represented by the population distribution among the internal sublevels. In addition, due to momentum, the atomic clouds split, reflect and recombine in the trajectory.

power is 240 mW with a beam size 30 mm in diameter ($1/e^2$ diameter) but the intensity ratio between Raman laser beams needs to be adjusted carefully to cancel the AC Stark shift (see section 5.3.3). To suppress the spontaneous radiation, the detuning of Raman laser Δ is chosen to be 2 GHz red-detuned from the state $|F^{'} = 1\rangle$, resulting in π pulse duration equal to 26 μs. Fig. 4.17 depicts the timing sequence and the corresponding manipulation of atomic wavepackets in internal and external states. Each Raman pulse has rectangular shape in time with a separation equal to T. Considering the edge effect of the magnetic shields and quantization coil, the first $\pi/2$ Raman pulse is triggered on the place which is 5 cm away from the bottom opening of the magnetic shields. The cloud is coherently manipulated into a superposition of states $|F = 1, m_F = 0\rangle$ and $|F = 2, m_F = 0\rangle$ with different velocities owing to the recoil velocity. A π pulse then inverts the internal and external states. In the end of the atom interferometry, the two atomic wavepackets converge spatially and are interfered by the third Raman pulse. At t=500 ms, the detection laser is turned on for 50 ms to detect the transition probability. As discussed in Chapter 2, in order to compensate the Doppler shift in free fall, the frequency difference between the Raman beams (namely the RF frequency applied on the modulator) is chirped at a rate $\alpha \approx 2\pi \times 25.1$ MHz/s. The population distribution in different internal hyperfine states at the outputs is related to the gravity by:

$$P_{|F=2,m_F=0\rangle} = \frac{1}{2}[1 - \cos(k_{eff} g T^2 - \alpha T^2)] \tag{4.17}$$

Fig.4.18 shows the population of atoms in state $|F = 2, m_F = 0\rangle$ by scanning the chirp rate with T equals to 10 ms, 15 ms and 30 ms respectively. In the central fringe, the atomic population coincides at a crest. Thus the phase shift induced by Doppler effect is compensated, which is independent of T. After fitting the data, we obtain the chirp rate of interest at $\alpha = 2\pi \times 25164858$ Hz/s $\pm$ 12 Hz/s. The local gravity g is determined as 9.817239(4) m/s^2 is obtained.

Improvement

After realization of the atom interferometer, a lot of efforts have been devoted to increasing the sensitivity by increasing the interrogation time T. Before the implementation of the shield box for the vibration isolator, T was limited below 50 ms. Beyond that, the fringe was completely washed out due to the increased vibration noise from the retro-reflecting mirror. After improving the performance of the vibration isolator, T was increased to 120 ms. In addition, the power of the cooling laser was doubled by replacing the previous tapered amplifier by one with a higher gain (Thorlabs, TPA780P20), leading to increase the launching efficiency and improvement of the signal-to-noise ratio of the fringe. Fig. 4.19 shows the fringes with T=100

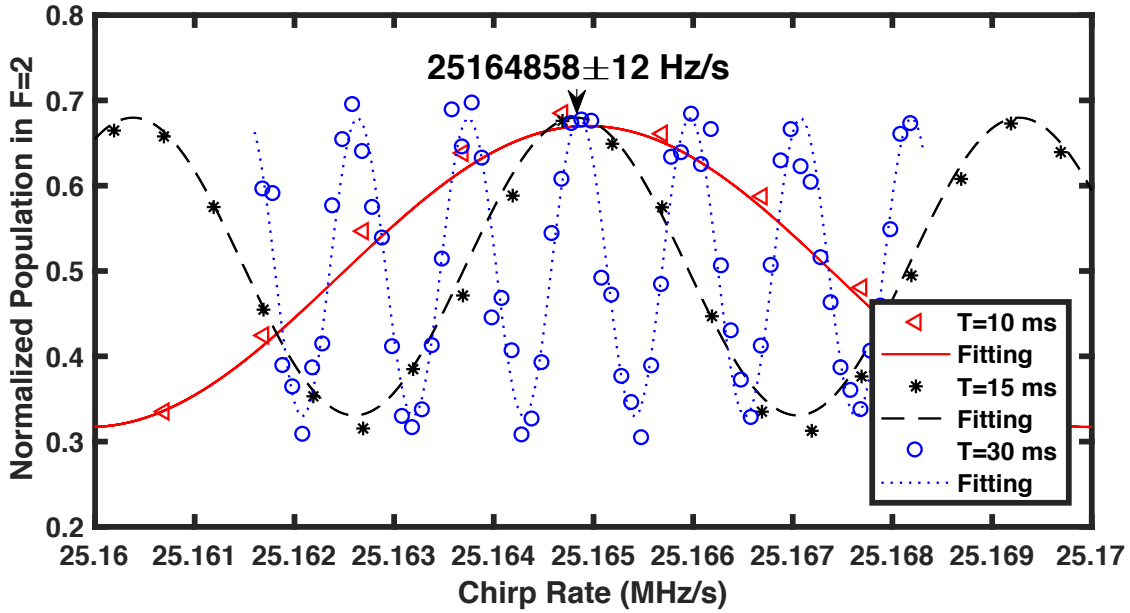

Figure 4.18: Mach-Zehnder atom interferometer fringes as a function of chirp rate. The same measurement is repeated with T equal to 10 ms, 15 ms and 20 ms respectively. The center fringe is indicated by arrow, where the interferometry phase induced by local gravity is cancelled. After fitting the data, the chirp rate at central fringe is 25164858 ± 12 Hz.

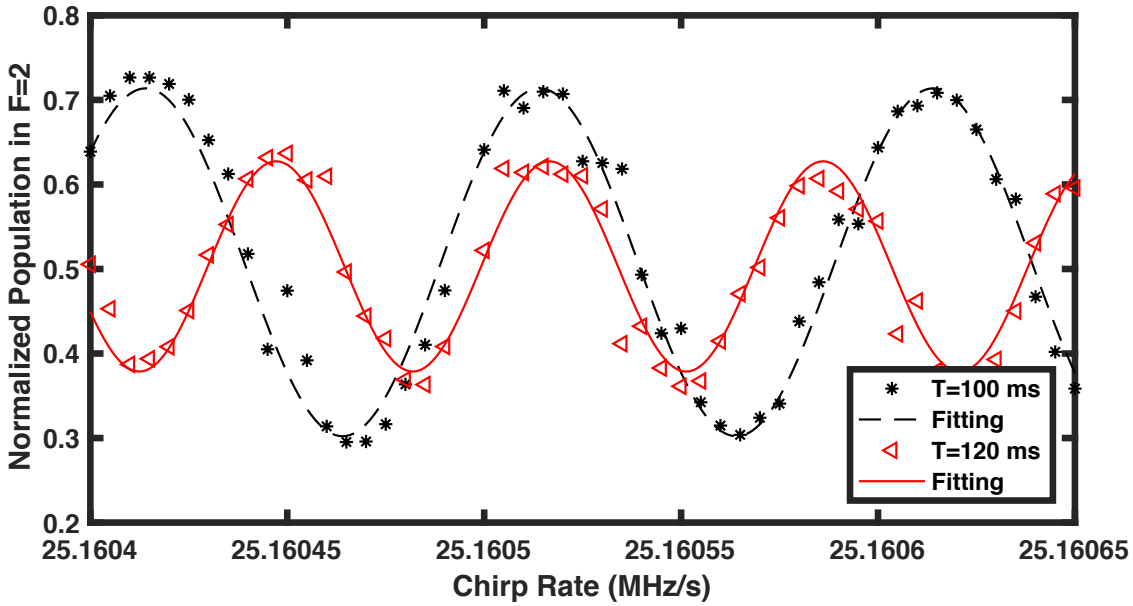

Figure 4.19: Mach-Zehnder atom interferometer fringes with T equal to 100 ms and 120 ms respectively.

and 120 ms. The measurement was performed at a rate of 0.5 Hz. Each point is an average of three shots. After fitting the data, we obtain the gravity uncertainty of 15 μGal when T=120 ms. Considering the total integral time of the two measurement, we achieve a sensitivity [1]of 225 $\mu\text{Gal}/\sqrt{Hz}$ when T=120 ms. The sensitivity limitations will be discussed in chapter 5.

4.4.4 Spatial Interference Elimination

In the EOM scheme, Raman lasers consist of a carrier frequency and an infinite number of sidebands separated by the RF driving frequency. Thus the Raman transition can be driven by at least two pairs of frequency combinations ($\omega_c - \omega_m$, ω_c) and (ω_c, $\omega_c + \omega_m$), where ω_c is the carrier frequency and ω_m is the RF driving frequency. As a consequence, the effective Rabi frequency has a spatial dependence with a periodicity of $\lambda_{rf}/2$, where λ_{rf} is the wavelength of the RF applied[94, 126]. In addition, the multiple Raman transitions also induce a phase shift which is spatially dependent in the atom interferometry [110]. In contrast, Raman laser based on OSSB scheme can suppress the unwanted laser considerably. Thus the interference caused by the unwanted laser frequencies in EOM scheme can be eliminated. To verify this conclusion, we make a comparison measurement in atom interferometry experiment with Raman laser based on EOM and OSSB scheme respectively, the setup of which is shown in Fig.4.20. In the measurement, only the modulator is changed by either EOM or IQ modulator. The detuning Δ is set to be 2 GHz red-shift from the $|F^{'}\rangle$=1 state whilst the total Raman laser power is the same. The RF frequency applied on both the EOM and IQ modulator is 6.834 GHz.

Spatial Dependent Raman Transition

Raman pulses were applied at different positions along the longitudinal direction in the interferometry region. The pulse duration is set at 50 μs, which corresponds to the π pulse duration at the start point. The RF frequency applied to the EOM and I/Q modulator is equal to the separation between the ground state hyperfine levels F = 1 and F = 2 ($\approx$ 6.834 GHz). Figure 4.21 shows the spatial dependence of the Raman transition. The wavelength of oscillations is measured to be 22 mm which matches with the half wavelength of the RF signal. The amplitude of the Raman transition was reduced a factor of two at the valley compared with the crest. The same measurement was repeated in the FC-OSSB scheme, showing that the spatial dependence is removed to below the experimental noise level. The fluctuation of the Raman transition is less than 10%, which is induced by other perturbation, and shows no oscillatory spatial structure. Although

[1]The definition is made in section 5.1.2.

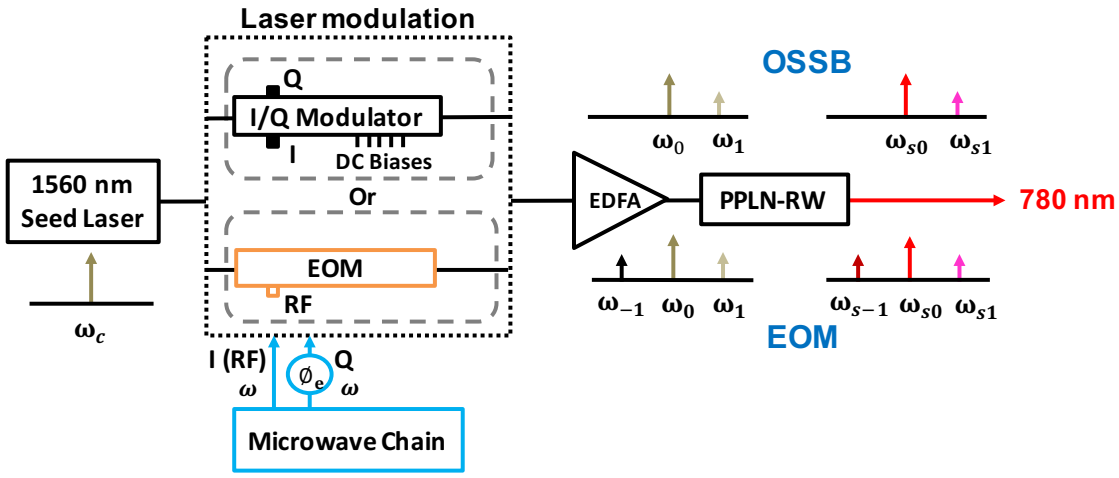

Figure 4.20: The Raman laser system for measuring the spatial dependence of the Raman transition probability. In the measurement, only the modulator are exchanged between IQ modulator and EOM for the OSSB scheme and double-sideband scheme respectively. The schematics of the spectrum in the two laser schemes are visualized.

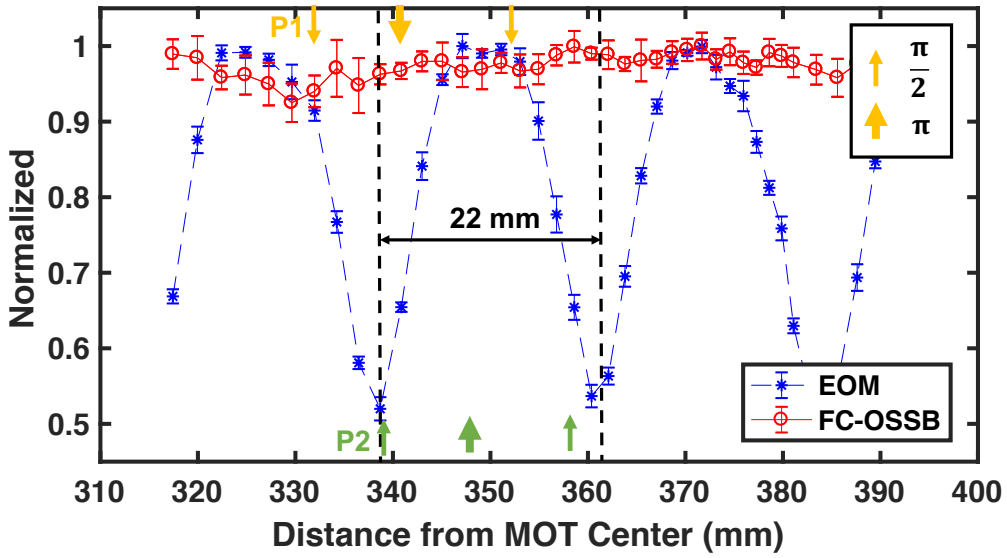

Figure 4.21: Measurement of spatial dependent Raman transition. Raman pulses were applied at different positions along the longitudinal direction in the interferometry. OSSB and EOM schemes are employed respectively to generate the Raman lasers. All the pulse duration is fixed to be 50 μs in the measurement. When the Raman lasers are generated by EOM scheme, the wavelength of oscillations is measured to be 22 mm which matches with the half wavelength of the RF signal. The amplitude of the Raman transition was reduced a factor of two at the valley compared with the crest. The same measurement was repeated in the FC-OSSB scheme, showing that the spatial dependence is removed to below the experimental noise level. The fluctuation of the Raman transition is less than 10%, which is induced by other perturbation, and shows no oscillatory spatial structure. Two positions P1 (yellow) and P2 (green) are selected as a the test positions for measuring the spatial phase shift in the next section. The set of $\frac{\pi}{2} - \pi - \frac{\pi}{2}$ pulses are added on the positions which are indicated by arrow in the same color.

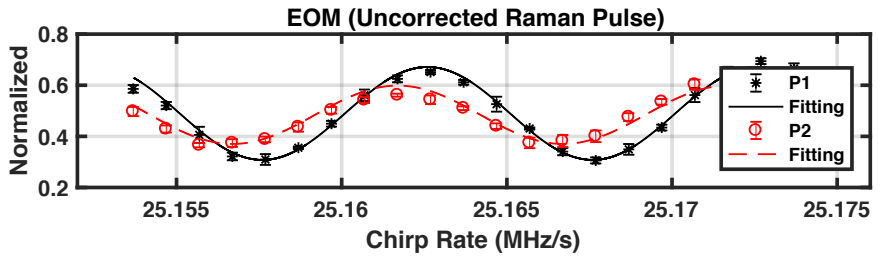

(a)

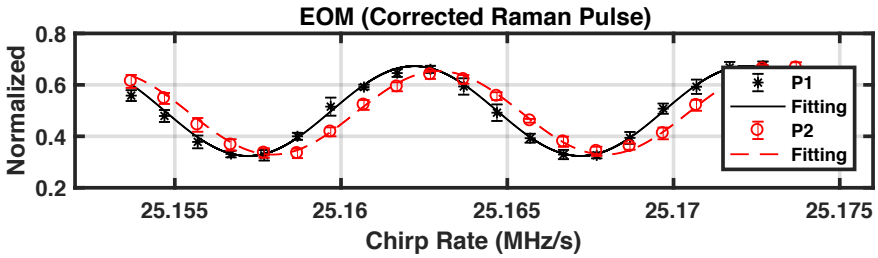

(b)

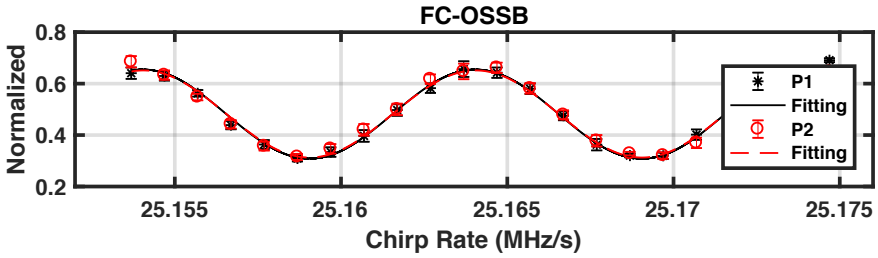

(c)

Figure 4.22: The interferometric fringes from different Raman laser schemes. From top to bottom, the EOM(Uncorrected Raman Pulase) scheme assuming single global Rabi frequency, the EOM(Corrected Raman Pulase) scheme compensating local Rabi frequency variation, and FC-OSSB.

the interference effect in EOM scheme can be reduced with small detuning ($\Delta < 1$ GHz), this increases contributions from spontaneous emission which can lead to loss the fringe contrast in atom interferometry experiments.

Phase Shift and Contrast

The position dependent phase shift induced by the unwanted laser frequencies in atom interferometry [110] can also be eliminated by employing Raman laser generated based on OSSB scheme. To evaluate the performance of the OSSB system, both schemes were used to operate a Mach-Zehnder atom interferometer at two different sets of positions, P1 and P2, which are labelled in Fig. 4.21. The time separation between pulses was set to 10 ms. The sideband power ratio ω_{s1}/ω_{s0} is chosen to be 1/2 to cancel the first order AC Stark shift. Figure 4.22 shows the atom interferometric fringes acquired by sweeping the chirp rate α under different

modulation configurations. In order to further investigate the effect arising from spatially varying Raman transition in EOM scheme, the measurements are performed under two different assumptions: (1) single global Rabi frequency; (2) spatially dependent Rabi frequency. In the first case, the Raman π and $\pi/2$ pulse durations are set based on the Rabi frequency at the first position of P1. In the second case, all the pulse durations are set by the local Rabi frequency measurements. In the FC-OSSB scheme, the pulse durations are set by the Rabi frequency at the first position of P1. By fitting the data, the phase shifts and the contrasts for different conditions are extracted for comparison. The results are summarized in the table 4.1.

Table 4.1: The phase shifts and the contrasts of the interferometric fringes from different Raman laser schemes. The results for P1 and P2 are marked by black and red respectively. EOM(U): EOM(Uncorrected Raman Pulase); EOM(C): EOM(Corrected Raman Pulase).

	Phase Shift (mrad)		Contrast	
	P1	P2	P1	P2
EOM(U)	1509	2077	22%	12%
EOM(C)	1759	1294	20%	19%
OSSB	597	596	21%	20%

With the EOM scheme, the fringes measured at P1 and P2 shift away from the fringes measured with the FC-OSSB scheme, regardless of whether the Raman pulses duration is corrected or not. Without correcting the Raman pulse duration in the EOM scheme, the phase measured at P1 and P2 has a relative phase difference 568 mrad. In addition, the contrast is reduced from 22% to 12%, nearly a factor of two decrease between P1 and P2. After correcting the Raman pulse duration, the fringe contrast at P2 can be recovered to 19% but there is still a spatially dependent phase difference at both P1 and P2. However, with the FC-OSSB scheme, the fringe at P2 is shifted by 1 mrad with a small contrast decrease around 1% compared with the one at P1. As proposed in the paper [110], the EOM scheme is still adoptable for atom interferometry application in high-precise gravity measurement by numerically calculate the phase shift induced by the unwanted laser lines in the EOM scheme, which demands the atom interferometer parameters are precisely estimated. However, the OSSB approach has been shown to effectively remove these concerns, and others, without adding additional complexity to the laser system.

4.5 Summary

This chapter has discussed the construction of the essential components of the atom interferometer. The laser system based on OSSB scheme supplies the Raman laser beams. While the single-sideband modulation is degraded due to the SHG process, the first order sideband is still suppressed by -21dB. Thus the spatial

interference induced by the unwanted laser lines is reduced significantly. Employing the Raman laser based on OSSB scheme, the Mach-Zehnder atom interferometer was realized. After employing the shield box for the vibration isolator, the interrogation time T was increased to 120 ms, allowing a sensitivity of 225 μGal/$\sqrt{\text{Hz}}$ to be achieved.

CHAPTER 5

ANALYSIS AND CHARACTERISATION

In this chapter, we start to evaluate the current limitation of the experiment in terms of the sensitivity and accuracy. This also offers guidance for the further improvement in the future. In the following section, we firstly introduce some equations and terminologies, providing definition for the reader. We then calculate the potential phase noise present in the experiment such as that due to the detection, residual vibration and Raman lasers. In the remaining sections, we will focus on analysing the interferometer phase shift and estimating the systematic error of the gravity measurement. Finally, the budgets of the systematic noise and errors are listed.

5.1 Definitions

5.1.1 Noise and Errors

As the introduction in chapter 2, the transition probability at the interferometer outputs can be simply described by a trigonometric function:

$$P = A(1 + C\cos(\Phi)) \tag{5.1}$$

where A is the mean transition probability, C is the contrast and Φ is the interferometer phase. The normal fringe versus the interferometer phase is depicted in Fig. 5.1. In order to achieve the highest phase sensitivity, we operate the experiment at the steepest slope of the fringe, i.e. the midfringe where $\Phi = \pm\pi/2$. Around this point, the transition probability has an approximatively linear dependence on the phase variance:

$$\partial P = -AC\sin(\Phi)\partial\Phi = -AC\partial\Phi \tag{5.2}$$

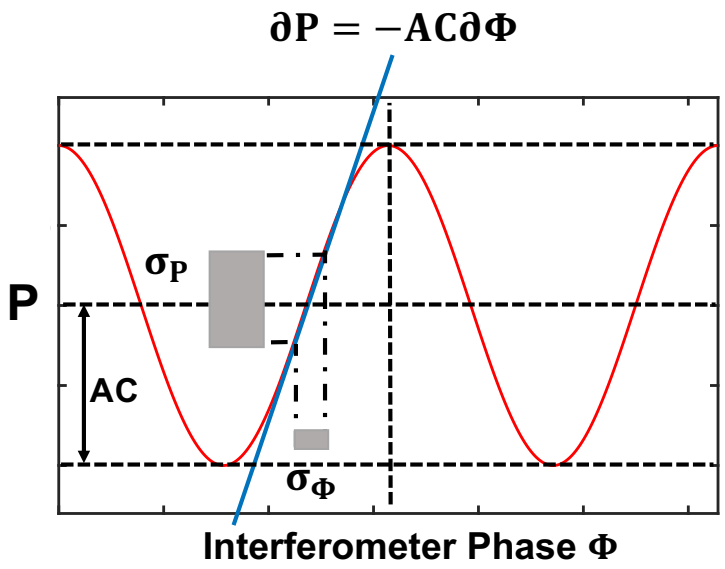

Figure 5.1: Illustration of the atom interferometry fringe versus the interferometer phase. The amplitude of the oscillation is AC. On the slope of the fringe, an interferometer phase noise σ_Φ can induce the fluctuation of the transition probability by σ_P.

Given an interferometer phase noise σ_Φ, the induced fluctuation of the transition probability on the slope is $\sigma_\Phi/2$, where we assume $A = 1/2$ and $C = 100\%$. If substituting the Doppler phase shift $\Phi = k_{eff}gT^2$ into above equation, the variability of gravity measurement σ_g induced by the interferometer phase noise can be given by:

$$\sigma_g = \frac{\sigma_\Phi}{2k_{eff}T^2} \tag{5.3}$$

Similarly, if a phase bias $\delta\Phi$ is present in the experiment, the gravity error is calculated by $\delta g = \delta\Phi/2k_{eff}T^2$. This is how we calculate the noise and errors of gravity measurement in the following sections.

5.1.2 Terminologies

In the field of metrology, some terminologies are defined as a standard to assess the systematic specifications of an instrument. However, some of these terminologies are indistinct in the field of atom interferometry and even differ from the metrological definition. In this thesis, we follow the terminologies definition in the reference [127, 128] and also take the common usage in other groups into consideration.

Precision, Sensitivity and Resolution

Precision is interchangeable with terms like repeatability and short-term variability, which describes the variance of repeated measurements under identical conditions. It is ascribed to the random noise of the instrument. In the field of atom interferomtery, resolution and sensitivity are also popular to evaluate the performance of the instrument. According to the usage in the reference [129, 130, 131], the sensitivity is often expressed in unit of g per shot, $g/\sqrt{Hz}$ or g at 1s, which means the smallest observable change of signal either in a single measurement or in unit time. Averaging multiple measurements can eventually increase the sensitivity until reaching the instrumental or environmental noise floor. Then resolution is used to specify the measurement uncertainty after a certain integration time, which is expressed in unit of g or μGal [25, 132] in an atom interferometer. To some degree, we can regard the sensitivity as the resolution when the integrating time is 1 s. However, in metrology, sensitivity is the quotient of the change in an indication of a measuring system and the corresponding change in a value of a quantity being measured and resolution is the smallest measurable change which causes perceptible change in the indication. In this thesis, in order to comply with the established custom of terminologies usage in atom interferometry, we use the term sensitivity to define the gravity uncertainty in single measurement. Its value is estimated in section 5.2 by evaluating the standard deviation in gravity measurement (σ_g) caused by the variant of noise present in our experiment. Resolution is used to evaluate the optimal gravity uncertainty after integrating a certain time and calculating the short-term and long-term variability.

Stability

Due to the environmental changes and instrumental drift, the variability exhibited by the measurement from day-to-day is different. In particular, with some time-dependent noise, the measurement data is non-stationary, which means they are not evenly distributed across the frequency band. This results in the standard deviation of the long-term data not converging. To estimate both the short-term and the long-term variability of the gravimeter in time domain, Allan deviation is employed here [133].

Assume we have a sequence of equally spaced gravity measurement $g_n = g(t_n)$ with $t_{n+1} = t_n + \tau$, where τ is the interval between two consecutive measurements. The Allan deviation has the form of two-sample variance [25]:

$$\sigma_g^2(2,\tau) = \frac{1}{2}\langle (g_{n+1} - g_n)^2 \rangle \tag{5.4}$$

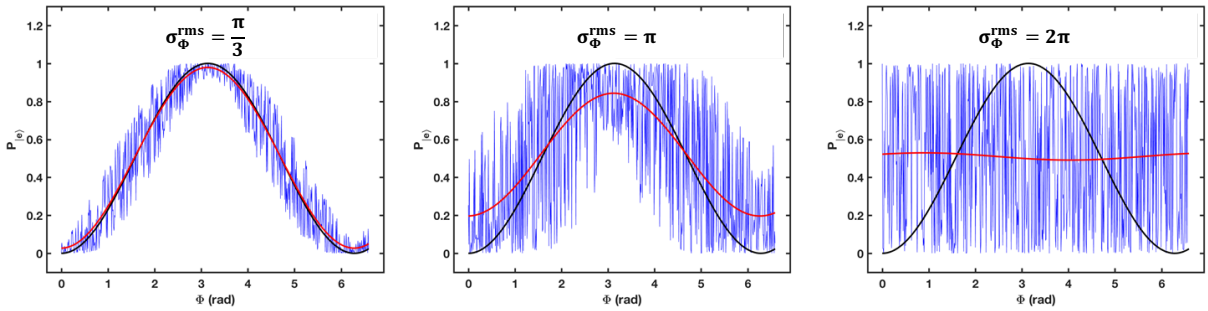

Figure 5.2: Illustration of the fringe visibility with varying amplitude of phase noise. The purple trace is simulated date by adding the phase noise with a standard deviation σ_Φ^{rms} into the Equ. 5.1. The curve in black is the fringe without any phase noise while the one in red is the curve fitting to the data.

For long time separations $t = N\tau$, the Allan deviation is given by:

$$\sigma_g^2(2,t) = \sigma_g^2(2,N\tau) = \frac{1}{2}\langle(\sum_{k=0}^{N-1}\frac{g_{n+k}}{N} - \sum_{k=N}^{2N-1}\frac{g_{n+k}}{N})^2\rangle \tag{5.5}$$

If the noise of consecutive measurements g_n is uncorrelated, then we have

$$\sigma_g(2,N\tau) = \frac{1}{\sqrt{N}}\sigma_g(2,\tau) \tag{5.6}$$

One benefit of the Allan deviation is that it can be used to identify different measurement noise sources [134, 135].

Signal-to-noise Ratio

The signal-to-noise ratio (SNR) of the experimentally observed interferometry fringes can affect the mathematical fitting uncertainty and the gravity measurement precision accordingly. We can relate the the variability of gravity measurement to the SNR of the interferometer fringe. Suppose neither A nor C fluctuate, the SNR is defined by:

$$SNR = \frac{AC}{\sigma_P} = \frac{1}{\sigma_\Phi} = \frac{1}{k_{eff}T^2\sigma_g} \tag{5.7}$$

Fig. 5.2 simulates the atom interferometer fringes with varying phase noise σ_Φ based on Equ. 5.1. Transition probability with and without noise are plotted in blue and red respectively. With the phase noise increasing, the contrast of the fitted curve (black) is decreased as well as the SNR. When the phase noise is $\pi/3$, the SNR is 100 while the SNR is reduced to about 3 when the phase noise is π. The fringe is completely washed out when the phase noise is add up to 2π. Therefore, to guarantee the fringe readable, we have to limit the

phase noise to less than 2π.

Bias

Bias is similar to accuracy, characterizing the measurement offset from the true value. The discrimination is that accuracy is a qualitative term referring to whether there is agreement between gravity measured by gravimeter and its true value while bias is a quantitative term describing the difference. We adopt the term bias to access the measure of the systematic errors. In the section 5.3, we firstly analyse the systematic errors and estimate the bias value. In the future, the bias will be identified by the comparison with other reference standards like FG-5, which is in preparation (see chapter 6).

5.2 Noise

The noise appearing in atom interferometers can be organized in two classes, the noise due to the detection of the quantum state of the atoms and the noise caused by the interferometer itself. In the atom interferometer, with uncorrelated atoms, the fundamental measurement noise is the quantum projection noise (QPN), which is uncertainty to find atoms in a state. This intrinsic noise defines the ultimate sensitivity of the instrument. In practice, the measurement variability is often restricted by other noise like detection noise, seismic vibration, Raman laser phase noise, etc.

5.2.1 Quantum Projection Noise

At the output of the atom interferometer, the atoms are in a superposition of states $|F = 1, m_F = 0\rangle$ and $|F = 2, m_F = 0\rangle$. The population distributed in the two hyperfine states is probed by fluorescence detection. However, for an uncorrelated ensemble of atoms, the population measurement is uncertain and limited by the quantum projection noise (QPN) [136], which limits the sensitivity of an atom interferometer without squeezing. For N atoms in detection, the variance of the transition probability is $\sigma_P = \sqrt{P_2(1-P_2)/N}$, where $P_2 = 1/2$ is the probability of the atoms in the state $|F = 2, m_F = 0\rangle$ at midfringe. Substituting the above equation into Equ. 5.3, the interferometry phase noise due to QPN is derived by:

$$\sigma_g = \frac{1}{k_{eff} T^2 \sqrt{N}} \tag{5.8}$$

where k_{eff} is effective wave vector of Raman laser and T is the interval between Raman pulses. In our experiment, there are $\sim 3 \times 10^6$ atoms in detection. Thus the ultimate sensitivity is charactered by $\sigma g \approx$

0.24 μGal when T=120 ms.

Photon shot noise

Due to the particle nature of the laser, counting the number of photons incident on the photodiode has a statistical quantum fluctuation, which follows a Poisson distribution [137]. The standard deviation is equal to the square root of the average number of photons: $\sigma_{photon} = \sqrt{N_{photon}}$. Similar to calculating the QPN, the photon shot noise in the atom interferometer is:

$$\sigma_{PSN} = \sqrt{\frac{P_{F=2}(1 - P_{F=2})}{N \times n_{photon}}} \tag{5.9}$$

In above equation, $n_{photon} = (R_{sc} \times \tau \times A)/4\pi$ is the mean number of photons hitting on the photodiode per atom, where R_{sc}, R_{sc} and A are the same definition in Equ. 3.4. In order to reach the quantum projection noise regime, at least 1 photon per atom should be detected, i.e. $n_{photon} \geq 1$. In the experiment, the solid angle and detection duration are constants, which are 0.54 and 800 μs respectively. The detection beam is 2 MHz red-detuned. Assume $I = 3I_{sat}$, the n_{photon} is calculated to be about 436 photons/atom. Thus the photon shot noise is much lower than the atom shot noise. Its contribution can be neglected.

5.2.2 Vibration Noise

The vibration on the retro-reflecting mirror is the primary noise source to limit the interferometer sensitivity in our experiment. In our lab environment, without any method to shield the mirror (placing the mirror on the optical table), the interferometer interrogation time T is limited below 5 ms. Above 5 ms, the atom interferometer fringe is completely washed out. After introducing the passive vibration isolator (MinusK), T is increased to 50 ms. Especially after the platform is set up as the way we investigated (see chapter 4), T is increased to 120 ms. Fig. 5.3 shows the residual vibration measured on the vibration isolator as well as the one measured on the floor. As described in section 2.3.3, we can estimate the error of gravity measurement related to the vibration noise by using formula:

$$\sigma_g = \frac{\sigma_\Phi}{k_{eff} T^2} = \sqrt{\int_0^\infty \mid H_\phi \mid^2 \frac{1}{T^4 \omega^4} S_a(\omega) d\omega} \tag{5.10}$$

where $S_a(\omega)$ is the power spectral density of vibrational acceleration and H_ϕ is the transfer function. Due to the low-pass filters property of transfer function, the vibration is weighted with roll-off at frequencies higher than 1/T. For T=120 ms, vibration above 10 Hz is effectively filtered as the red curve shown in Fig. 5.3.

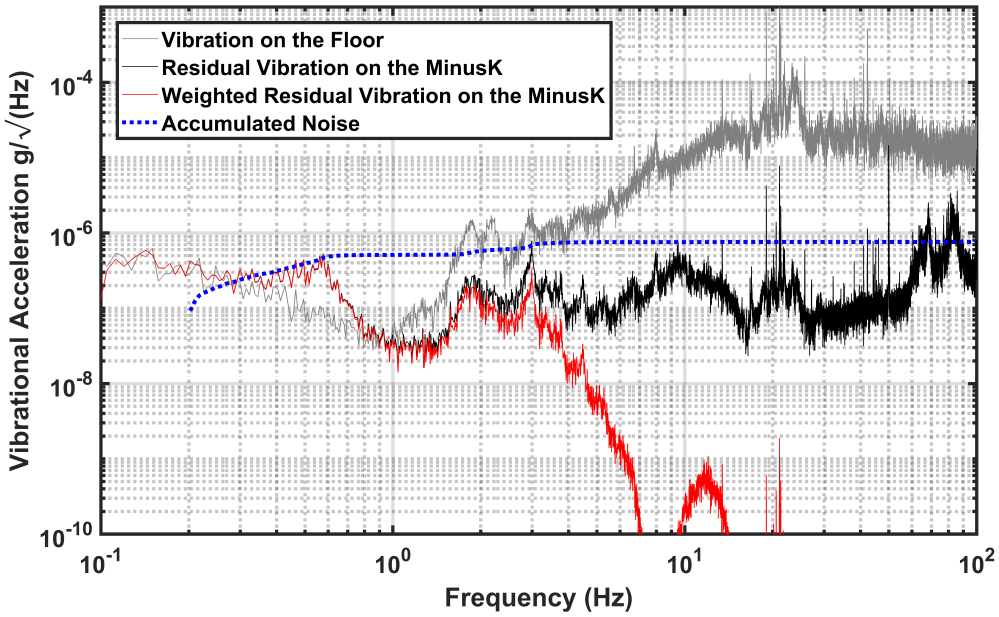

Figure 5.3: Amplitude spectrum density of the vibration noise in our lab. Vibration on the floor and platform are measured at the same time and plotted in silver and black respectively. The weighted vibration noise is plotted in red with T=120 ms.

The blue dotted line is the accumulated σ_g^{rms} from low to high frequencies. Because of the vertical resonance frequency of the vibration isolator at 0.5 Hz, vibration at frequency between 0.1 Hz and 1 Hz is amplified and accounts for the major phase noise. Therefore in recent experiment, when T=120 ms, the interferometer phase noise due to the seismic vibration is 407 mrad, amount to the sensitivity is of 170 μGal.

5.2.3 Raman Laser Noise

Influence of Raman Phase Noise

Our Raman laser is generated by the optical single sideband modulation (see section 4.1). Thanks to inherent phase coherence of this modulation technique, we avoid suffering from laser phase noise induced by the electronics of the phase locking. Besides, since the laser out of the modulator undergoes the same optical paths, the phase coherence is maintained all the time. Therefore we can regard the noise from the RF reference as the remain noise source. As presenting in section 4.1.3, the RF reference is generated by 7 GHz mixed with the RF signal out of the external RF source, which is arbitrary function generator (AFG) in this measurement. We then use the signal source analyser (SSA, Agilent N9030B) to measure the phase noise. As shown in Fig. 5.4, the red curve represents the phase noise spectral density of the Raman laser which

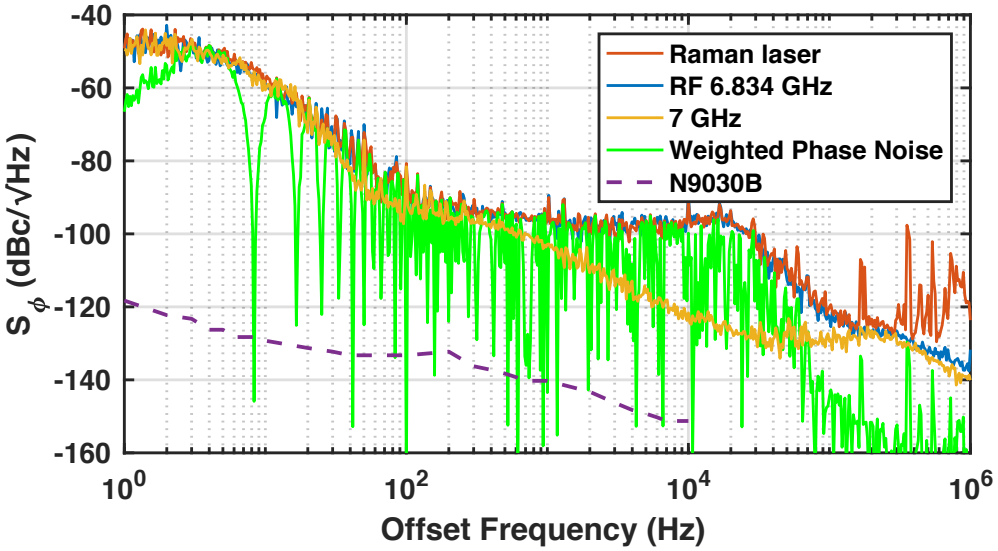

Figure 5.4: Measurement of the phase noise in Raman laser system. The measurement was performed with the aid of a signal source analyser (Agilent, N9030B). The phase noise of the signal source analyser at 6.834 GHz is plotted in dashed line, which is converted according to the phase noise at 10 GHz in the data sheet [138].

is measured after the PPLN RW. We also measured the phase noise of the RF reference 6.834 GHz (blue curve) and the 7 GHz (yellow curve) for comparison. Below 100 kHz, the phase noise spectral density of the Raman laser overlaps the one of the RF reference very well. The bump at 20 kHz is caused by the phase noise of the AFG. Above 100 kHz, the phase noise of Raman laser is higher than the one of RF reference, which can be explained by the intensity noise of the seed laser. However, the transfer function of the atom interferometer works as a low-pass filter. The weighted phase noise shown in green curve in the figure with the cut-off frequency 38 kHz when the Raman π pulse duration is 25 μs. Thus we can neglect the phase noise contribution above 100 kHz. We recall Equ. 2.47 to calculated the sensitivity limitation of the gravity measurement due to the Raman laser phase noise:

$$\sigma_g = \frac{\sigma_\Phi}{k_{eff}T^2} = \sqrt{\int_0^{+\infty} \frac{|H(2\pi f)|^2 S_\phi(f) df}{k_{eff}T^2}} \tag{5.11}$$

where $S_\phi(f)$ is the phase noise spectral density of the Raman laser and $H(2\pi f)$ is the weighting function. Given T=120 ms, the induced interferometer phase noise is 18 mrad and the according sensitivity is 7.7 μGal.

Influence of Raman Intensity

The Raman laser intensity is not actively stabilized in the experiment. The fluctuation of the intensity then contributes to the interferometer phase noise by changing the Rabi frequency. Assume that the transition probability relates to the Rabi frequency is given by $P = A(1 + C\cos(\Omega\tau))$, where Ω is the Rabi frequency, τ is the Raman pulse duration, C is the fringe contrast and AC is the fringe amplitude. When the relative intensities between Raman beams is fixed, the standard deviation of the transition probability due to the total Raman laser intensity change is given by:

$$\sigma_P = -\sigma_\Omega AC\tau\sin(\Omega\tau) \tag{5.12}$$

Suppose the fringe contrast C=1, after employing the $\pi/2$ pulse, the variance of the transition probability is

$$\sigma_{P,\pi/2} = \sigma_\Omega\tau = \frac{\pi\sigma_\Omega}{2\Omega} = \frac{\pi\sigma_I}{2I} \tag{5.13}$$

where I is the total Raman laser intersity. In a complete interferometer sequence ($\pi/2 - \pi - \pi/2$), since the intensity fluctuation is independent for these three pulses, the variance is given by [25]:

$$\sigma_P = \sqrt{\sigma^2_{P,\pi/2} + \sigma^2_{P,\pi} + \sigma^2_{P,\pi/2}} = \frac{\sqrt{3}\pi\sigma_\Omega}{2\Omega} = \frac{\sqrt{3}\pi\sigma_I}{2I} \tag{5.14}$$

At the midfringe, the interferometer phase noise induced by the Raman intensity noise is $\sigma_\Phi = \frac{\sqrt{3}\pi\sigma_I}{I}$. We measured that the total Raman laser power changed 3% within one day, which was induced by the the polarisation fluctuation in the fibre delivery system. Assume the fluctuation of the Raman laser intensity is up to 3%, the corresponding interferometer phase noise is calculated to be 163 $m$rad.

Influence of Raman Laser Polarisation

The amplitude of the Raman transition also depends on the polarisation configuration of the Raman laser. As we introduced in section 4.4.1, the Rabi frequency is approximately given by:

$$\Omega_{eff} \cong \frac{e^2}{4\hbar^2\Delta}[\mathbf{E}_1 \times \mathbf{E}_2^*] \cdot M \tag{5.15}$$

where M is the dipole matrix elements. In our experiment, the polarisation-maintain fibre directs the laser with linear polarisation into the vacuum chamber and the $\lambda/4$ waveplate before the retro-reflection mirror at

the bottom converts the linear polarisation to the orthogonal polarisation. However, due to the imperfection of the coupling into the PM fibre or the temperature fluctuation of the environment, the polarisation of the incident Raman laser presents momentary shifting. Assume the shifting of the polarisation of the incident Raman is θ, then the angle between the incident and retro-reflected Raman laser is shifted by 2θ. According to the Equ. 5.15, the corresponding varying of the Rabi frequency is $\sigma_\Omega = 2\theta\Omega$. Recalling the transition probability formula $P = A(1 + C\cos(\Omega\tau))$, the fluctuation of the transition probability at the midfringe is thus given by:

$$\sigma_P = -AC\sin(\Omega\tau)\tau\sigma_\Omega = -\frac{\pi}{2}\theta \tag{5.16}$$

After substituting the polarisation extinction ratio of the Raman laser 30 dB into θ, we achieve that the fluctuation of the transition probability is 0.0016, amount to the interferometer phase shift is of 3.2 mrd and the sensitivity is of 0.67 μGal when T=120 ms .

5.2.4 Timing Noise

In our experiment, the timing is mandated to the digital signal sequence out of the hardware (sbRIO-9627, National Instrument), which is externally locked to the Rubidium clock (FS725, Stanford Research Systems). All the other electronic equipments are also synchronized to the Rubidium clock. Therefore the stability of the timing is substantially determined by the stability of the rubidium clock. As described above, if the Doppler phase shift is compensated by chirping the Raman frequency difference, the sensitivity to the timing of the Raman pulses is reduced. However, we operate the experiment at the midfringe, where the phase shift is proportional to squared in integration time T. If the interval of the Raman pulses jitters, a phase shift due to the fluctuation of T is given by:

$$\sigma_\Phi = 2k_{eff}(g - \alpha_m)T\sigma_T = \pm\pi\frac{\sigma_T}{T^2} \tag{5.17}$$

where α_m is the chirp rate at the midfringe. Based on the specifications of the Rubidium clock, the short-term stability is 2×10^{-11} at 1 s. Substituting into the above equation, the interferometer phase noise is 0.5 nrad when T=120 ms, which can be neglected in the experiment.

5.2.5 Tilting Noise

The entire apparatus was supported by the aluminium frame as shown in Fig.3.1. The Raman telescope is mounted on the top. If the aluminium frame has oscillation modes or the building tilts, the Raman laser

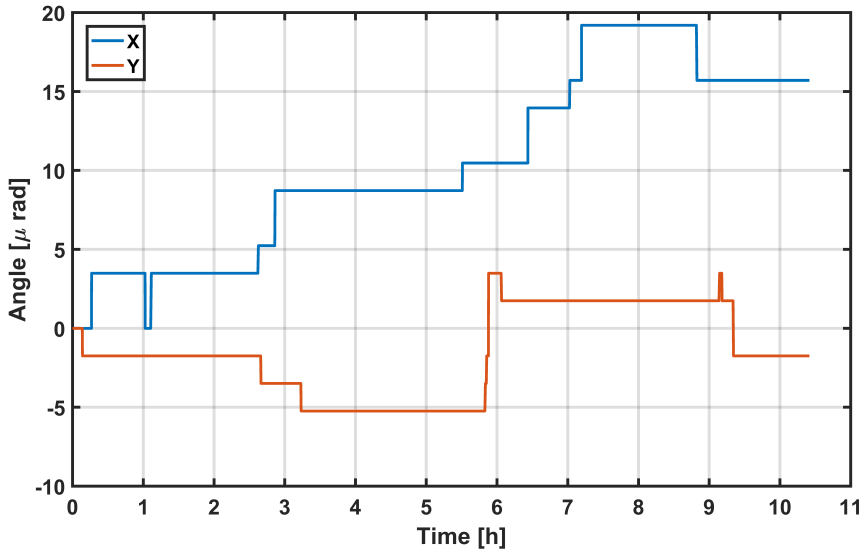

Figure 5.5: Measurement of the tilting of the aluminium frame over time.

vector swings around the gravity direction, resulting in measurement fluctuation. For small tilting angle, the interferometer phase noise can be estimated by the below equation:

$$\sigma_\Phi \approx k_{eff} g T^2 \sigma_\theta^2 \tag{5.18}$$

where σ_θ is the standard deviation of the angle fluctuation between the Raman laser and the direction of the gravity. In order to achieve a sensitivity of 1 μGal in a single measurement, the short-term fluctuation of the Raman laser vector should be less than 45 μrad. We measured the tilting of the aluminium frame by a two-axis inclinometer (DMP, Jewell Instruments LLC), which has a resolution to < 8.7 μrad. As shown in the Fig. 5.5, the tilting of the aluminium frame within a period of experiment duty cycle ($\approx 3s$) is less than the measurement resolution of the sensor. Assume $\sigma_\theta = 8.7$ μrad, the corresponding uncertainty of gravity measurement is 76 nGal, which can be ignored in recent experiment. However, the tower frame also develops a long-term incline (about 15 μrad in 10 hours), resulting in underestimating the gravity. This effect will be discussed in detail in below section 5.3.2.

5.3 Systematic Errors

In this section, we analyse the potential systematic errors. Some effects affect the measurement of gravity by modifying the Raman resonance condition (quadratic Zeeman effect, AC stark Stark effect, collisional

displacement), some determine the expression of the phase shift (vertical alignment of Raman laser, value of k_{eff}), and others directly affect the phase difference between lasers (beam aberrations, influence of the refractive index at the crossing of the cloud).

5.3.1 Magnetic Field

The first expected source of systematic errors comes from the Zeeman effect. Although the atoms are prepared in the magnetic-insensitive state $m_{F=0}$, the quadratic Zeeman effect is still present. Given an external magnetic field, the quadratic Zeeman shift is derived by the Breit-Rabi formula [84]:

$$U_m(z) = -\frac{\mu_B^2(g_J - g_I)^2}{2h\omega_{hfs}}B^2 = \kappa B(z)^2 \tag{5.19}$$

where κ is defined as the coefficient of the quadratic Zeeman shift. It is calculated κ=575.15 Hz/G^2 for the hyperfine sublevels $|F = 1, m_F = 0\rangle$ to $|F = 2, m_F = 0\rangle$ of the ^{87}Rb ground states $5^2S_{1/2}$. The corresponding phase shift can be calculated by:

$$\delta\Phi_{Zeeman} = 2\pi\kappa \int_{-\infty}^{+\infty} g(t)B(t)^2 dt \tag{5.20}$$

where $g(t)$ is the sensitivity function defined in chapter 2. In fact, thanks to the symmetry features of $g(t)$, a spatially uniform magnetic field doesn't contribute to the interferometer phase. However, as shown in Fig. 4.11, the magnetic field inside the magnetic shields is spatially inhomogeneous. As a consequence, several systematic errors are generated:

(1) The magnetic field gradient causes a force proportional to the energy gradients. Atoms are subject to an additional acceleration equal to:

$$\mathbf{a}_m = -\frac{\nabla U_m(z)}{m}\mathbf{z} = \frac{2h}{m}\kappa B\frac{dB}{dz}\mathbf{z} \tag{5.21}$$

Thus the gravity measured is biased by the parasitic acceleration.

(2) Due to the inhomogeneous magnetic field, the energy displacement is position-dependent, resulting in the resonance condition being also position-dependent. Considering the spatial separation of the two arms of the interferometer, the phase shifts due to the Zeeman effect are different between the two paths. The calculation based on the Equ. 5.20 is not accurate.

(3) Because of the magnetic gradient, the atomic trajectory in the interferometer are deformed by the

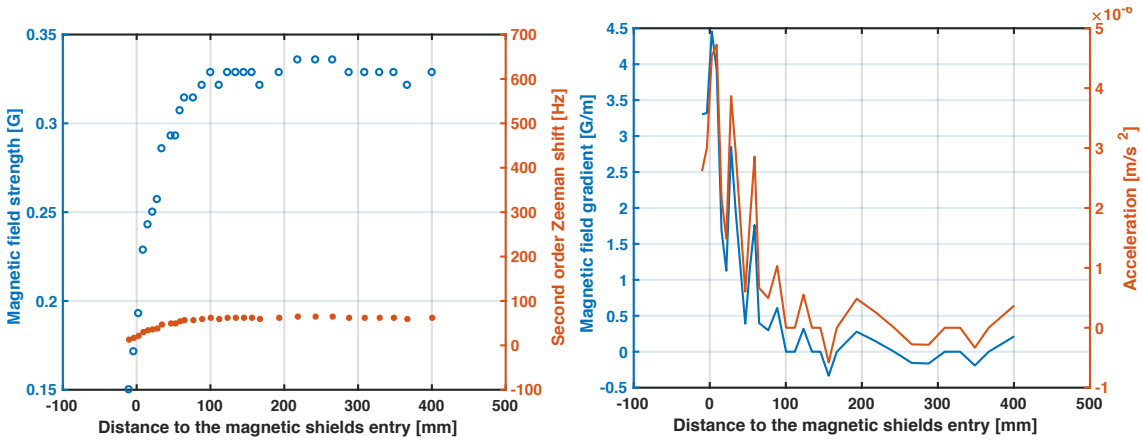

(a) (b)

Figure 5.6: Magnetic field strength and the gradient inside the magnetic shields, which was measured by magnetic-sensitive Raman transition.

magnetic forces. At the interferometer output, the centres of the wavepackets don't overlap. Phase error $\delta\Phi_{sep}$ arises.

We employ the magnetic-field-sensitive Raman transition to measure the magnetic field distribution inside the shields [139]. During the measurement, the quantisation coil current was set to be 0.1 A. Fig. 5.6a shows the longitudinal magnetic field and the second-order Zeeman shift accordingly. The magnetic field gradient and the additional acceleration are also derived and shown in 5.6b. Considering the seperation of the wavepackets in the two arms, we follow the atom interferometry in the path-integral description to calculate the phase shift at the outputs, which is expressed as [140]:

$$\Delta\Phi = k_{eff} \cdot (r_1 - 2\frac{r_{B2} + r_{A2}}{2} + \frac{r_{B3} + r_{A3}}{2}) - (\delta\omega_{1B} - \delta\omega_{1A} + \delta\omega_{2B} - \delta\omega_{2A} + \delta\omega_{3B} - \delta\omega_{3A})T \qquad (5.22)$$

where r is the central position of the wavepacket, $\delta\omega$ is the detuning of the Raman transition, the two arms of the atom interferometer are indicated by A and B, the $\pi/2 - \pi - \pi/2$ Raman pulses are indicated by number 1,2 and 3 respectively. In above equation, the first contribution is expressed as a function of the positions of the wavepackets when the Raman transition happens. This term is related to the deformation of the trajectories of the wavepackets. The second contribution can be generated by the displacement of the resonance condition induced. Since both the two terms are dependent on the positions, it is necessary to determine the trajectories of the wavepackets inside the magnetic shields during the integration time. Fig. 5.7 shows the atomic trajectory with (solid lines) and without (dotted lines) the magnetic force. At the output, the atomic clouds displace from the theoretical position by 14.8 nm. If we zoom in the outputs

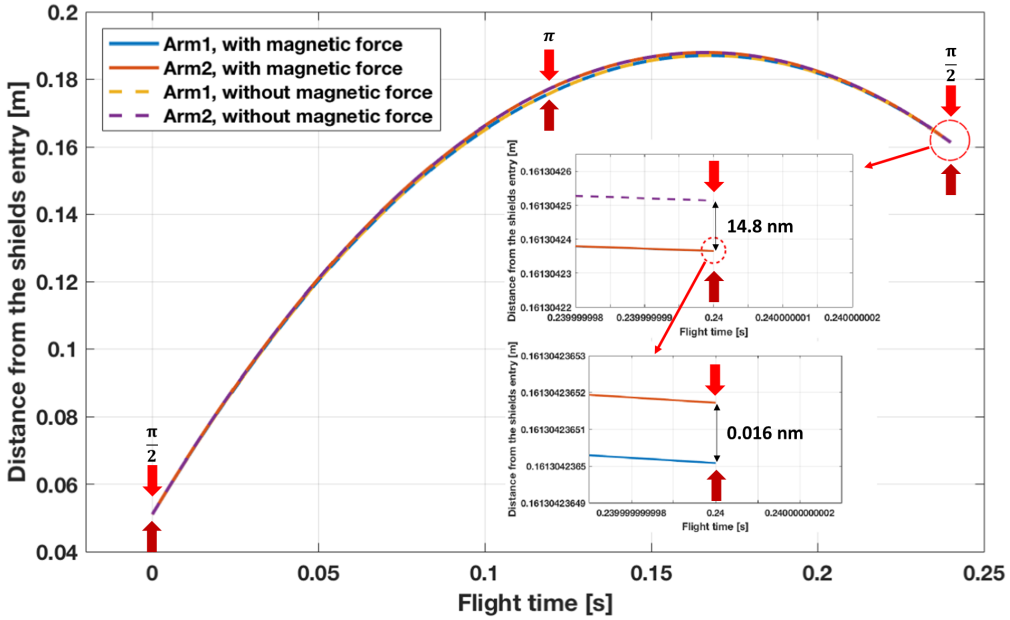

Figure 5.7: The atoms trajectory in atom interferometry sequence.

in presence of the magnetic force, the centres of the atomic clouds are separated by 0.016 nm. Since the maximum separation of the two arms are 1.4 mm, the atoms in the two arms experience the same Zeeman shift. Thus the phase shift from the second term of the Equ. 5.22 is neglected. Then we substitute the positions of the wavepackets into above equation, the interferometer phase shift induced by the magnetic field gradient is 202 mrad, corresponding to a systematic error of 87 μGal.

5.3.2 Raman Laser Alignment

The direction of the inertial force measured in the atom interferometry is determined by the orientation of the effective Raman wave-vector $\mathbf{k}_{eff}$, which is equal to the difference between the vectors of Raman beams $\mathbf{k}_1$ and $\mathbf{k}_2$. According to the scalar product of the Doppler shift $\delta\Phi = \mathbf{k}_{eff} g T^2$, the gravity is underestimated if the Raman beams are misaligned with the vertical direction. As shown in Fig. 5.8, the systematic errors is mainly induced by inclination of the Raman telescope and platform of the retro-reflection mirror: if the Raman laser telescope tilted by a angle θ and the platform is inclined by an angle α, the Raman laser incident beam $\mathbf{k}_1$ is tilted by θ and the orthogonal line of the surface of the retro-reflection mirror is inclined by θ with respect to the direction of gravity. Consequently, the retro-reflected beam $\mathbf{k}_2$ is tilted by $2(\theta + \alpha)$ relative to

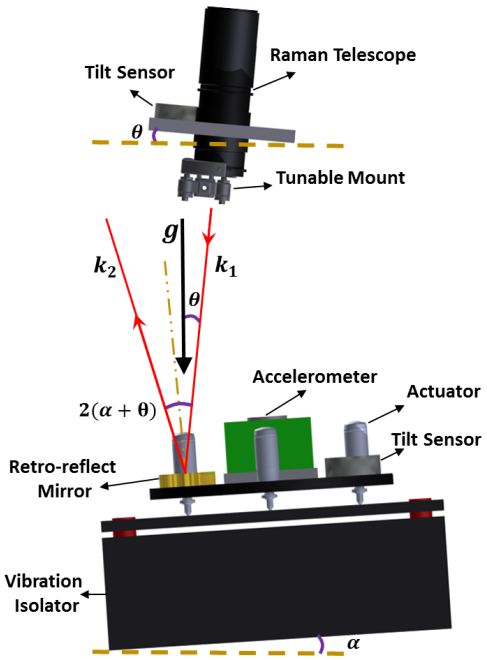

Figure 5.8: Illustration of the retro-reflection setup of the Raman laser beams.

the incident beam $\mathbf{k}_1$. In this case, the measured gravity is given by:

$$g_{//} = \frac{\mathbf{k}_{eff} \cdot \mathbf{g}}{|\mathbf{k}_1| + |\mathbf{k}_2|} = \frac{(\mathbf{k}_1 - \mathbf{k}_2) \cdot \mathbf{g}}{|\mathbf{k}_1| + |\mathbf{k}_2|} = \frac{k_1 \cos(\theta) + k_2 \cos(2a + \theta)}{k_1 + k_2} g \tag{5.23}$$

Then the systematic error on g is derived by:

$$\begin{aligned} \delta g = g - g_{//} &= \frac{k_1(1 - \cos(\theta)) + k_2(1 - \cos(2\alpha + \theta))}{k_1 + k_2} g \\ &= (\frac{\theta^2}{2} + \frac{k_2}{k_1 + k_2}(2\alpha^2 + 2\alpha\theta))g \\ &\approx (\frac{\theta^2}{2} + \alpha^2 + \alpha\theta)g \end{aligned} \tag{5.24}$$

In order to achieve an accuracy of $\delta g/g = 10^{-9}$ for the atom interferometer, the tilting need to be controlled with an accuracy better than 50 μrad. In our experiment, we align the Raman beams by a Michelson interferometer. The procedure is visualised in Fig.5.9.

We firstly performed the Michelson interferometer to approximately align the incident beam k_1 with the vertical. As shown in Fig. 5.9a, a beam splitter is inserted into the Raman beam path to direct a fraction of light to the other output. A hollow corner cube is placed on the sides to retro-reflect the fraction of light with a deviation less than 5 μrad. The reference mirror on the bottom of the chamber is replaced by a

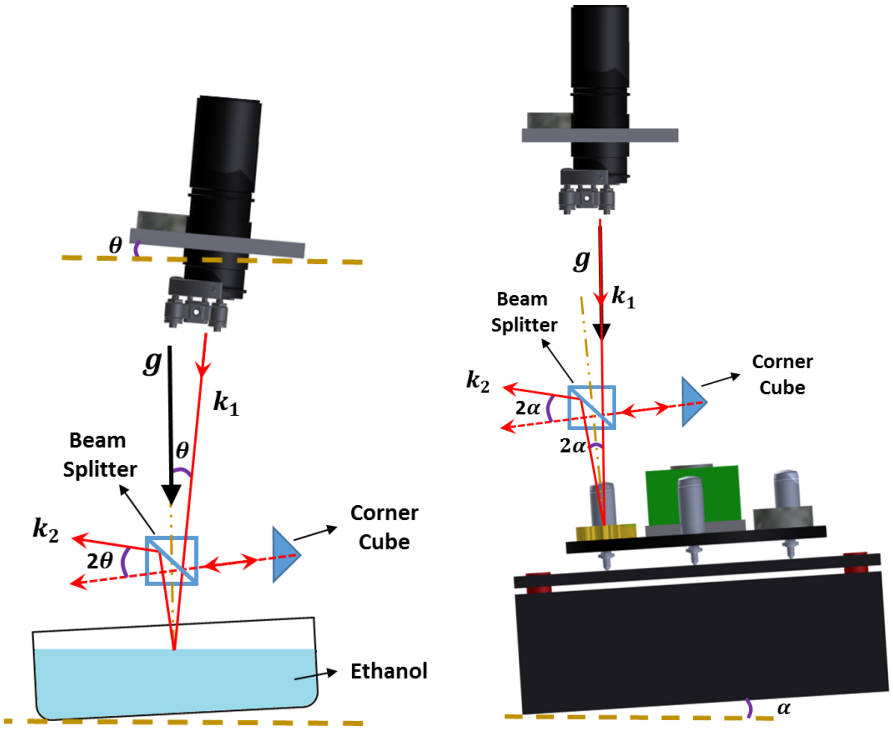

(a) (b)

Figure 5.9: The procedure of Raman laser alignment. In Fig. 5.9a, the liquid mirror is used as the reference to align the incident light vertical. In Fig. 5.9b, the liquid mirror is replaced by the reference mirror platform to align the reflected light vertical.

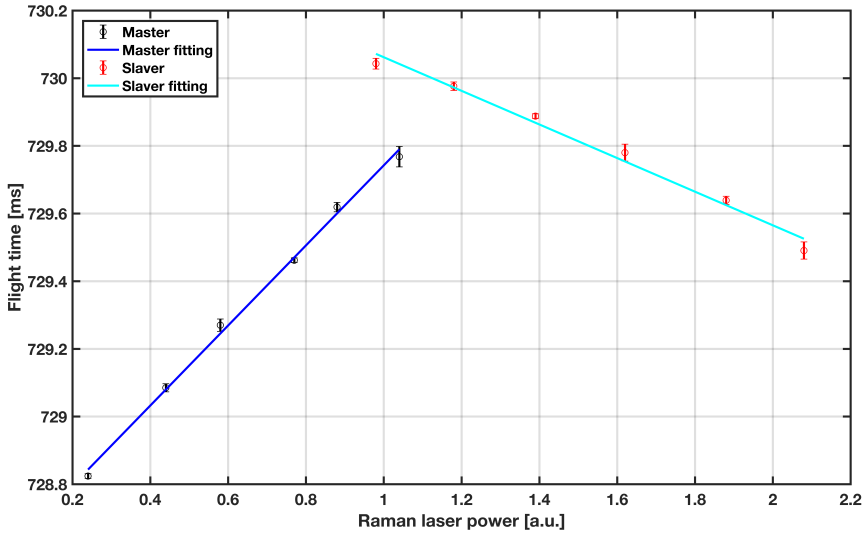

Figure 5.10: The shifting of flight time when atoms are detected versus the power of Raman master and slave laser. Solid lines are least squares linear fits to the data.

liquid mirror. Its surface is horizontal, so that the retro-reflection can only be parallel to the incident beam automatically if the incident beam is perfectly vertical. Then both the retro-reflected beams are focused onto the CCD camera to optimise the overlap. Considering that the surface of the liquid may agitate, we employ the viscous Ethanol with a density of 99%. On the other hand, the container is chosen consciously to be big enough to suppress the surface bend in the center because of the tension. However the interference fringes are still too blurred to be observed on the CCD chip. We therefore have to only minimize the separation of the beams at a great distance. This leads to an uncertainty of 100 μm over 1 m, that is $\theta \approx 100$ μrad.

We then replace liquid mirror by the reference mirror platform and repeat the above procedure. After this initial alignment, we can reduce the θ and α with a uncertainty 100 μrad. Substitute into Equ. 5.24, the error on g is estimated to be 25 μGal if the both angles have the same sign.

5.3.3 AC Stark Shift

As we present in section 2.2.3, the ratio between the intensity of the Raman master and slaver laser needs to be set to the value which cancels the AC stark shift. In principle, for a Raman detuning Δ=-2 GHz, the light shift is cancelled by setting the intensity ratio equal to 2.3. The actual ratio is determined experimentally by the method as below [132].

With a fixed detuning of the Raman lasers, the resonance frequency of the Raman transition is determined

by:

$$\delta\omega = \omega_{HFS} + \alpha I_m + \beta I_s + \delta\omega_{others}. \tag{5.25}$$

where ω_{HFS} is the unperturbed hyperfine splitting and $\delta\omega_{others}$ is the frequency shift induced by others like recoil shift. Due to the above detuning, the fraction of atoms selected in the velocity profile is related to the light shift. Thus the arrival time at the detection chamber also depends on the light shift. Fig. 5.10 shows the results of the arrival time when we fix I_m and change I_s and vice versa. The proper ratio of the Raman laser intensity is determined by the ratio of coefficients α and β:

$$\frac{I_M}{I_s} = -\frac{\beta}{\alpha} \tag{5.26}$$

After the linear fitting, we achieve that the intensity ratio is 2.38 when the Raman laser is red detuned of 2 GHz to the transition $|F = 2\rangle \rightarrow |F^{'} = 1\rangle$, which is in good agreement with the ratio provided by the theoretical calculation in section 2.2.3.

5.3.4 Two-photon Light Shift

In the retro-reflection configuration, there are two pairs of counter-propagating Raman lasers with opposite wavevectors able to drive the two-photon Raman transition. When the frequency difference of one pair is tuned to be resonant with the hyperfine states, the Raman transition is driven. However, the other pair which is off-resonant induces a light shift on the couped states. This effect is called two-photon light shift (TPLS) [141]. During a Raman pulse, TPLS is given by:

$$\delta\omega_{TPLS} = \frac{\Omega_{eff}^2}{\pm 8\mathbf{k}_{eff}\cdot\mathbf{v}} + \frac{\Omega_{eff}^2}{4(\pm 2\mathbf{k}_{eff}\cdot\mathbf{v} + 4\omega_r)} \tag{5.27}$$

where $\mathbf{v}$ is the velocity of the atomic cloud, ω_r is the recoil shift and the sign refers to the direction of the wavevector. It is shown that the TPLS is proportional to the laser intensity and inversely proportional to the velocity of atomic cloud. The systematic error can be estimated with the sensitivity function. Considering that the TPLS only takes place during the Raman laser present, an additional function $h(t)$ is employed with $h(t)$=1 during the Raman pulse and $h(t)$=0 in other time. Then the phase shift due to TPLS effect is estimated by the equation below:

$$\delta\Phi_{TPLS} = \int_0^{2T} g(t)h(t)\delta\omega_{TPLS}dt \tag{5.28}$$

Since the duration of the Raman pulse is neglected compared with the interval of pulses T, the TPLS is considered to be constant during the Raman transition. Assuming that $\Omega_{eff}\tau = \pi/2$, the phase shift is given by:

$$\begin{aligned}\delta\Phi_{TPLS} &= \frac{\delta\omega_{TPLS}(2T)}{\Omega_{eff}} - \frac{\delta\omega_{TPLS}(0)}{\Omega_{eff}} \\ &= \frac{\Omega_{eff}}{4k_{eff}}(\frac{1}{v(2T)} - \frac{1}{v(0)})\end{aligned} \tag{5.29}$$

In our experiment, the velocity of the atomic cloud is 2.2 m/s at the first Raman pulse which is trigged on 55 ms after the launch while the velocity at the last pulse is 0.15 m/s. Thus we can neglect the phase shift induced by the two-photon shift in the last pulse. The phase shift due to the two-photon light shift is simplified to:

$$\delta\Phi_{TPLS} = -\frac{\Omega_{eff}}{4k_{eff}v_0} \tag{5.30}$$

Substituting the effective Rabi frequency $\Omega_{eff}/2\pi = 25$ kHz and the velocity v_0=2.2 m/s into above equation, the interferometer phase shift induced by the TPLS is predicted to be in the order of $\delta\Phi_{TPLS} = 11$ mrad, i.e. a bias on gravity measurement of approximately 27.5 μGal.

5.3.5 Coriolis Force

Our laboratory is based on the rotating frame of the Earth. When performing an inertial measurements in such a non-inertial reference system, a fictitious inertial force, Coriolis force, manifests in the measured acceleration of an uncoupled test mass. The amplitude is given by:

$$a_{Coriolis} = 2\Omega_{Earth} \times \mathbf{v} \tag{5.31}$$

where $\Omega_{Earth} = 72.7\mu rad/s$ is the rotation of the Earth and $\mathbf{v}$ is the velocity of the test mass. Fig. 5.11 shows the relative position of our apparatus with respect to the Earth. Since the direction of the inertial measurement is determined by the Raman laser wavevector $\mathbf{k}_{eff}$, only atoms with the horizontal velocity of the east-west direction $\mathbf{v}_{w-e}$ implies a Coriolis force which has a non-zero projection along the wavevector $\mathbf{k}_{eff}$. As a consequence, not only the contrast of atom interferometry fringe is decayed but also a systematic error arises in the gravity measurement [142]. Replacing $\mathbf{g}$ by $\mathbf{a}_{coriolis}$ in the Mahnder phase equation, the resulting phase shift is:

$$\delta\Phi_{coriolis} = 2\Omega_{earth} \cdot (\mathbf{v}_{w-e} \times \mathbf{k}_{eff})T^2 \tag{5.32}$$

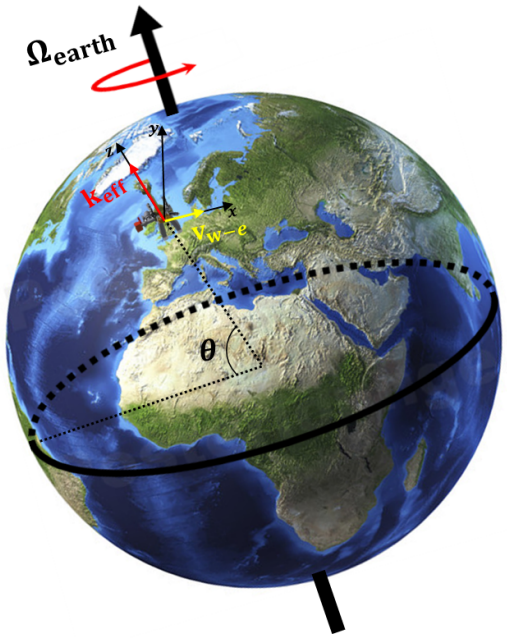

Figure 5.11: Illustration of the relative position of the apparatus with respect to Earth's rotation axis. The local latitude is θ. The direction of the Raman laser vector is indicated in red arrow. Atoms moves along west-east direction with velocity v_{w-e}.

In our experiment, the horizontal velocity of the atoms is estimated by measuring the shift of cloud center position during free fall. The standard absorption image technique is employed to photograph clouds at variant free fall time (The cloud image is perpendicular to the vertical). As shown in Fig.3.15, the cloud center drifts 0.2 mm in 15 ms, corresponding to a horizontal velocity $v_H = 13$ mm/s. Assume $\mathbf{v}_{w-e} = \mathbf{v}_H$ and substituting $\mathbf{v}_H$ and the local latitude ($52^o27^{'}05^{''}$ for Birmingham) into above equation 5.32, we get a systematic error of 186 μGal.

5.3.6 Environment Effect

The gravity value is highly dependent on the locations. In addition to the subsurface mass of the earth, varitions in latitude, elevation, terrain and time also have substantial imapct on the local gravity. Table A.1 summarizes some of the most important effects [27]. By default, we don't include these environmental effects into the estimation of the systematic errors when we operate the absolute gravity measurement. However, with the knowledge of the gravity anomaly at the observed locations, we are able to distinguish the instrument drift and compare the gravity measurements at different times and locations. Here we investigate some environmental effects which are related to the geographical environment at the sites of our lab .

Table 5.1: Uncertainties in Determining Environmental Sources Terms of Gravity

Source	Signal Range (μGal)	Uncertainty (μGal)	Time Scale
Solid Earth tides	300	0.2-0.5	Diurnal
Equilibrium ocean loading	20	0.2	Diurnal
Air pressure	8	1-5	Hours-Diurnal
Water-table	Site-dependent	Site-dependent	Seasonal
Polar motion	10	<0.01	12.14 months

Tide Effects

A primary source of temporal variations in gravity is the Earth tides due to the gravitational forces of the Moon and Sun and the rotation of Earth. The cumulative force of the tidal attraction exerts on the Earth varies in a periodic of roughly 12 hours, dependent on the relative positions of the three bodies. The maximum variation of the tidal acceleration within 24 hours is about 0.33 mGal. In a model of rigid Earth, the instantaneous tidal acceleration can be calculated by a sum of time-dependent cosine functions [4]. However, the tidal forces induce an elastic deformation of the earth's body. Especially, at a site adjacent to the oceans, the ocean loading also cause extra deformation. These deformations lead to additional gravity variations, resulting in the theoretical calculations discrepant with the observed earth tides in phase and/or amplitude. More sophisticated models are avaiable to predict the tides.[143]. In the future, we operate a continuous gravity measurement with our atom interferometer gravimeter and FG5 at the same region. Thus errors between the actual Earth tide and the theoretical estimation can be evaluated based on the measurements of the two instruments.

Gravity Gradient

The gravity is not spatially uniform. Theoretically, according to the Newton's law of universal gravitation, the gravity is inversely proportional to the square of the distance between test mass and the earth. Thus a vertical gravity gradient of approximately -300 μ Gal/m exhibits at the surface of the earth. The vertical distance of our interferometer is of the order of 15 cm, which refers to a gravity variation about 45 μ Gal. We must therefore take this effect into account. In fact, the practical gradient value is site-dependent. However, due to lack of the knowledge of the gradient in our lab, we use the theoretical gravity gradient to estimate its contribution to the systematic errors. As in the case of the magnetic field gradient, the phase shift induced by the gravity gradient can be derived with the path integral formalism and the first order is given by [25]:

$$\delta\Phi_{gradient} = \gamma k_{eff} T^3 (\frac{7}{12} gT - v) \tag{5.33}$$

where γ is the local gravity gradient, v is the velocity of the atomic cloud at the first Raman pulse. Substituting the experimental parameters (γ =-300 μGal, v = 2.2 m/s and T=120 ms) into above equation, the systematic error due to the gravity gradient is -126.4 mrad, corresponding to -54 μGal.

For a gravimeter with an accuracy of 10 μGal, the gravity gradient value must be measured with an uncertainty less than 55 μGal/m. A precise gradiometer is expected to measure the non-linearity of the gravity at the gravimeter position in the future.

Atmospheric Pressure

The variation of the atmosphere pressure affects on the Earth gravity field through two effects: The mass of the gas above the experiment exerts an attractive force opposite to that of the Earth on the atoms directly and hence reduces the value of the measured g. On the other hand, the air over the site induces the elastic deformation the Earth, changing the gravity indirectly. The second one is negelected here since its effect much smaller than our recent targeted accuracy. The amplitude of the gravity variation is approximately $\Delta g = -0.36$ μGal/mbar (the zero correction pressure is conventionally set at 1013.25 hPa) [144]. In typical weather, from an anti-cyclonic situation to a low-pressure situation, the variation of pressure can reach fifty millibars. The corresponding gravity variation is 15 μGal. Thus a barometer has been installed next to the gravimeter to ensure the long-term stability. The absolute gravity measured can be corrected by the formula:

$$\delta g_{air} = \kappa_{air}(P - P_n) \tag{5.34}$$

where P is measured pressure and P_n is the nominal pressure which is given by:

$$P_n = 1013.25(1 - \frac{0.0065h}{288.15 \text{ m}})^{5.2559} \tag{5.35}$$

where h is the topographic elevation in meters.

Precipitation

The precipitation is extremely variable in the British Isles. For rainfall, it typically occurs about one day in three in England. The rainfall can't only change the levels of the lakes and rivers but also increase the moisture content and groundwater level, resulting in an effect on the local gravity. The effect can be evaluated by equation [145]:

$$\delta g_p = +0.04192 \text{ g/cm}^2 \cdot d \quad \text{mGal} \tag{5.36}$$

where d is the mean density of the water slab in g/cm^3. For rainwater, d is substituted by 1 g/cm^3. Thus 10 cm of rainfall on the earth surface could increase the gravity by about 4 μGal.

5.4 Summary

This chapter analysed the sensitivity limitation and estimates the accuracy of the gravity measurements from the current experiment. The systematic unvertainty is listed in table 5.2. The primary limitation of the sensitivity is due to residual vibration, which generates an interferometry phase noise of 407 mrad, corresponding to a sensitivity of 170 μGal in a single measurement. To reduce the vibration further, an active vibration isolator with lower resonance frequency is under development [146]. The second biggest term is contributed by the intensity noise of the Raman laser, which is induced by the polarisation fluctuation in the fibre delivery system. This problem can be overcome by employing an active control scheme in the future [80]. After suppressing the above interferometer phase noise, the sensitivity is expected to increase to the level of 10 μGal in single measurement.

Table 5.3 shows the systematic errors budget. The biggest contribution is from the Coriolis effect, which generates a systematic error of 186 μGal. It is subtle to adjust the launching direction vertically. In practice, we can also revolve the apparatus until $\mathbf{v}_H$ is perpendicular to the East-West direction. Thus the Coriolis effect can be minimized. After the Coriolis effect, the most important phase shift is induced by the magnetic field gradient, which induce a systematic error of 87 μGal. In order to reduce this phase shift, we can launch the atoms further inside the shields, where the magnetic field is more homogeneous. The others contribute a systematic bias of approximately 30 μGal. In fact, the explicit value of the above systematic errors can be calculated precisely. The post-correction can be employed on the final gravity measurement.

Table 5.2: Systematic Noise Budget

Source	Interferometer Phase Noise (mrad)	Sensitivity (μGal)	
Quantum Projection Noise	1	0.24	
Photon Shot Noise			Neglected
Vibration Noise	407	170	
Raman Phase Noise	17	7.3	
Raman Intensity Noise	133	56	
Raman Polarisation Noise	3.2	0.67	
Timing Noise			Neglected
Tilting Noise			Neglected
Total		179	

Table 5.3: Systematic Error Budget

Source	Interferometer Phase Shift (mrad)	Bias (μGal)
Magnetic Field Gradient	202	87
Raman Laser Alignment	58	25
Two Photon Light Shift	11	27.5
Coriolis Force	438	189
Total		218

CHAPTER 6

GRAVIMETER COMPARISON CAMPAIGN

The aim of the project is to build a high precision gravimeter which is comparable with the state-of-the-art gravimeters. After we achieved the sensitivity 225 μGal/$\sqrt{\text{Hz}}$, a comparison campaign was put on the schedule. In Aug. 2017, the entire experiment was transported to the NERC Space Geodesy Facility in Herstmonceux UK for comparison with an FG5 from micro-g Lacoste. Figure 6.1 shows the distance between Birmingham and Herstmonceux. The characteristics of our atomic gravimeter are desired to be ascertained via comparison. One of the main objectives is to ascertain the accuracy budget of our atomic gravimeter, which is the key characteristic of an absolute gravimeter. In addition, the new site has lower vibration noise compared with the one present in our lab (located in the second floor of the building by a road). The silent environment conduces to improve the sensitivity further. This comparison also acts as the first test of being a transportable calibration platform, which is the next step of the project. In the following chapter, we firstly present the package of the experiment. The mechanical parts are rebuilt to improve the transportability and stiffness. Afterwards the entire transporting process including loading and unloading is reviewed. In the last section, we discuss the protocol of our gravity comparison with multiple gravimeters.

6.1 Package and Transport

6.1.1 Experiment Package

From the beginning of the experiment, we gave consideration to the transportability all the way. The entire system was designed to consist of three parts with feasibility for package: the sensor head in aluminium frame, the free space optics on breadboard and the electronics in rack. These subs-system were loaded on a van for the transportation. Concerning the thrashing on the road and the limited space in the van, some

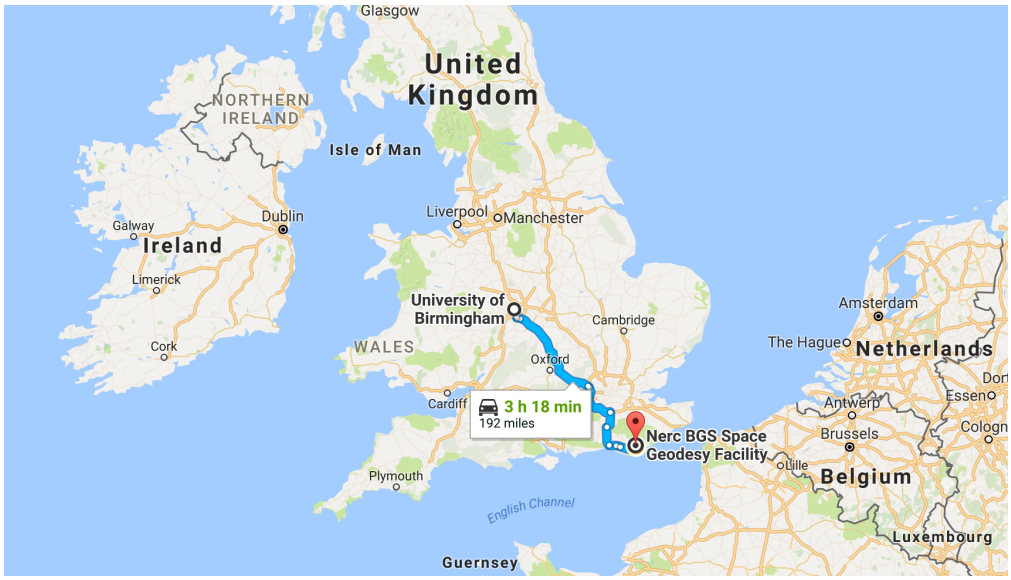

Figure 6.1: The transporting route from Birmingham to NERC Space Geodesy Facility in Herstmonceux via car. Cited from Google Map.

important modifications need to be made for the mechanical reinforcement and compactness.

Sensor Head

The previous sensor head was mounted on an aluminium frame as shown in Fig. 3.1. The defect of this design is that the sensor head just sat on the support pieces at three-point loosely, without any binding with other components. Thus in high-mobility and shaky environments, the sensor head has the risk to topple and fall. We then decided to rebuild the mechanical frame with thicker aluminium profile and redesign the support pieces. The latter is shown in Fig. 6.2. The new aluminium frame has dimensions of 1.7 m$\times$0.8 m$\times$0.6 m. The sensor head is mounted 0.4 m above the ground, which reserves the space for the vibration isolator platform. Although the entire apparatus is as heavy as 100 kg, four wheels attached on two sides allow single person to transport it. Another dominating change is the support pieces. Both the previous and new designs are zoomed in the sub-figures. In the new design, the support pieces are made of high density Polyethylene (PE300/PE-HWST), which has a density 0.947 g/cm^3 and a tensile strength at yield 25 MPa. This plastic material eliminates the troubles such as stray magnetic field, eddy current and leakage current. Instead of coarse contact in previous design, the new support pieces are screwed on the MOT chamber. In addition, a height-tunable post supplies an auxiliary support at the junction to ion pump. The entire vacuum apparatus is amounted on the aluminium frame like the Eiffel Tower pattern.

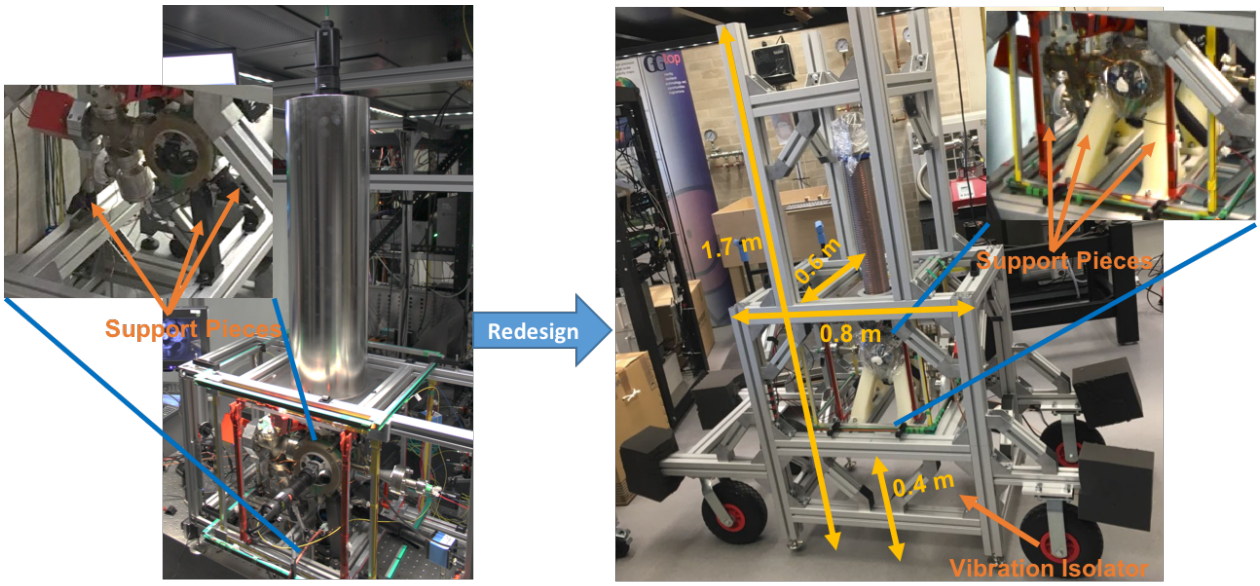

Figure 6.2: The change of the support frame for the sensor head. Two support pieces made of high density Polyethylene fix the vacuum apparatus on the aluminium profiles. A heigh-tunable post supplies a auxiliary support at the junction to the ion pump. Four wheels on the sides of the frame allow the transport by single person.

Free Space Optics

Originally the free space optics were set up on breadboards, which were amounted on the optical table. Some of the components also spread on the optical table. For transporting, we compressed all the optics components on two breadboards, which were amounted in stack in a moveable aluminium frame. The transform is shown in Fig.6.3. The entire aluminium frame has dimensions of 1.4 m×1.3 m×0.8 m with two breadboards spaced by 0.4 m. All the optics for atomic fountain including the laser modules, taped amplifier, laser locking and distribution are set up on the bottom breadboard while the upper breadboard is mainly for the Raman laser system including the OSSB apparatus, FP cavities and the laser distribution, locking and coupling setup. Vibration absorber rubber is placed beneath the breadboards for damping the shaking and preventing the deformation. On experiment, the two breadboards are lifted up at 0.8 m above the ground such that the case filled with electronics for the locking and reference frequency can be inserted at the bottom. During the transporting, the breadboards come down to lower the barycentre. Four wheels are mounted at the bottom, which allow the transport by single person.

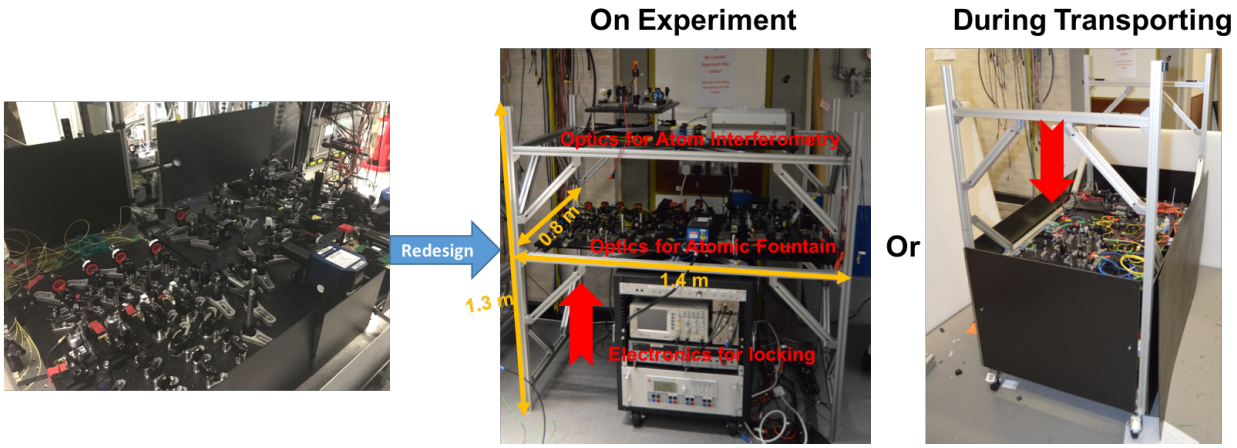

Figure 6.3: The aluminium frame for the free space optics. The components for atomic fountain and atom interferometer are mounted on the bottom and upper breadboard respectively. The breadboards are lifted up on experiment. The electronic for the locking and RF reference are placed underneath. During transporting, the breadboards come down to lower the barycentre.

6.1.2 Transporting Tour

The entire experiment was loaded in a van. Figure 6.4 shows the stages of loading, transportation and unloading of the apparatus from Birmingham to Herstmonceux.

6.2 Comparison Blue Print

6.2.1 Gravity Measurement Protocol

The operation of the atomic gravimeter starts from a scan of the complete fringes by altering the chirp rate of Raman laser for several values of T. According to the interferometer phase connected to the gravity $\Delta\Phi=(\mathbf{k}_{eff}g-\alpha)\mathrm{T}^2$, fringes overlap at a position where the chirp rate exactly cancels with the product of $\mathbf{k}_{eff}g$. Then gravity is extracted by scanning the desired chirp rate precisely. However, the measured gravity value includes systemic errors, which can not be inspected by the above method. During the comparison, we adopt a measurement protocol with a differential method to suppress some of the systemic errors. The first step is to achieve a gravity measurement with a resolution at the level of μGal. Before, we already achieved a sensitivity of 225 $\mu\mathrm{Gal}/\sqrt{\mathrm{Hz}}$, which was limited by the seismic noise in our lab. Based on the measurement of the CG5 in Birmingham and Herstmonceux, the seismic vibration in Herstmonceux is a few times lower than the one in our lab. Thus the sensitivity of our AI gravimeter is expected to arrive at few tens $\mu\mathrm{Gal}/\sqrt{\mathrm{Hz}}$. After an integration time of 100 s, we can achieve a measurement resolution of a few μGal.

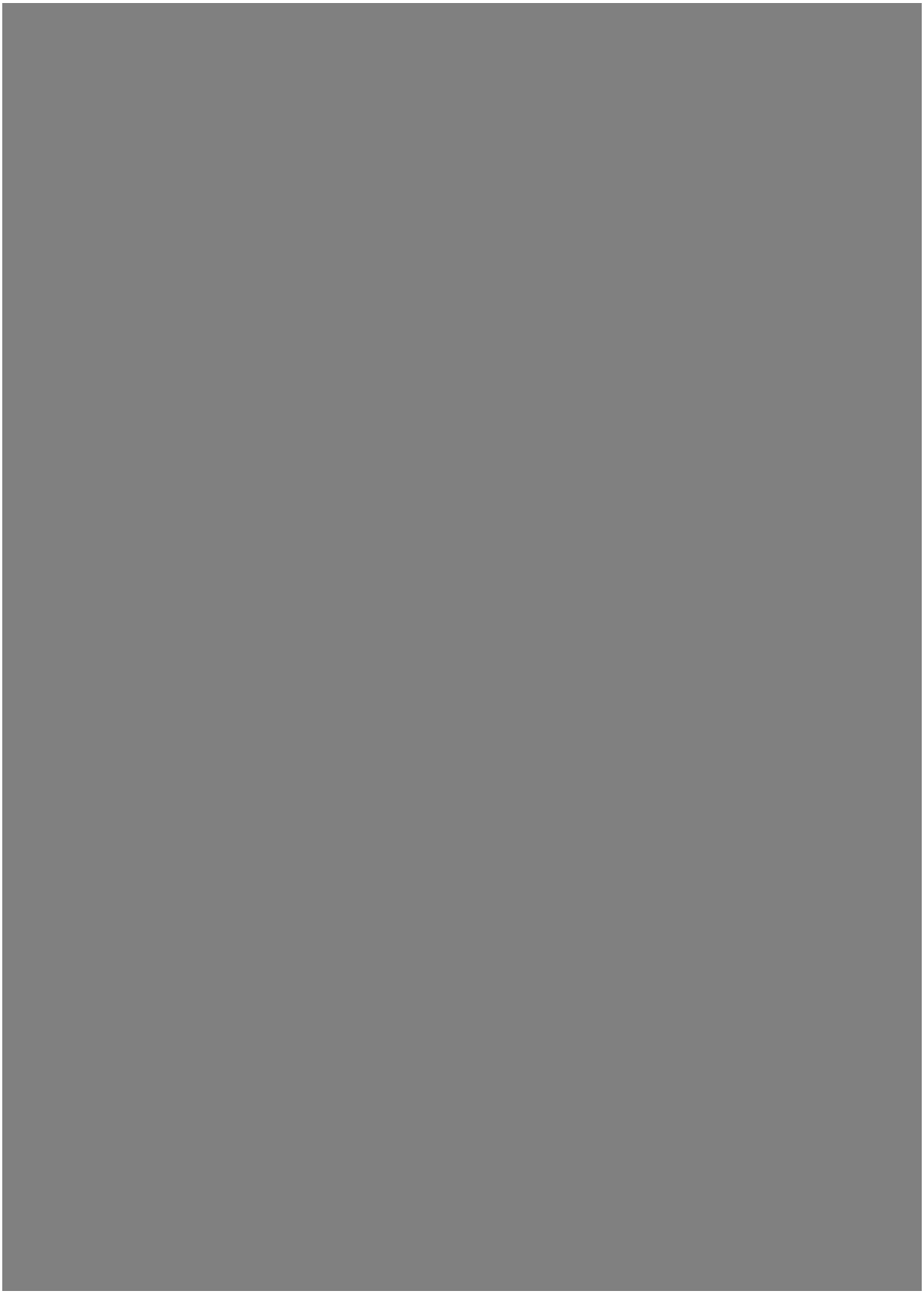

Figure 6.4: Review of the loading, transportation and unloading of the apparatus from Birmingham to Herstmonceux.

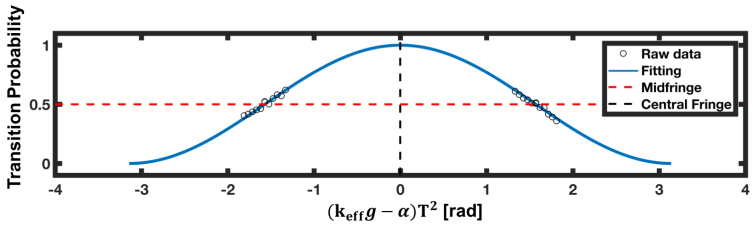

(a)

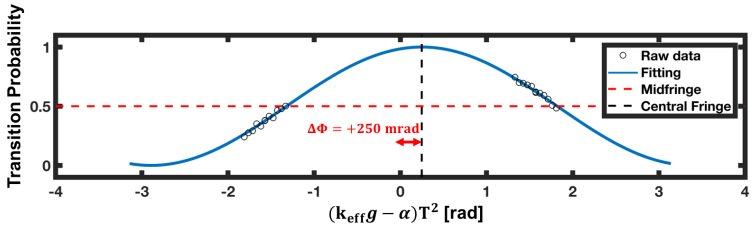

(b)

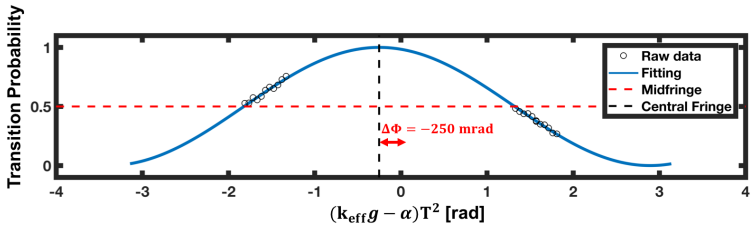

(c)

Figure 6.5: The virtualization of the gravity measurement. Gravity value is achieved by fitting the curve consist of 50 single measurements, which are distributed around the midfringes on the left and right slopes half and half. Figure 6.5a shows the atom interferometry fringe when interferometer phase is 0 while Fig. 6.5b and Fig. 6.5c show the fringes when interferometer phase is +250 mrad and -250 mrad respectively. The central fringe and midfringe are indicated by black and red dotted lines.

In the comparison, we will operate the measurement at 0.5 Hz. Thus each gravity value is a averaging of 50 single measurements, which will be realized by scanning a fringe with 50 points and fitting the data. The details are presented below.

(1) Once the correct chirp rate is determined, the variation of the remaining interferometer phase is limited to the interval (-π,π). The explicit value can be calculated from the distance away from central fringe. We operate the interferometer on the slopes to the left and right of the central point, where the sensitivity to phase fluctuation is maximal. For a single gravity value, a series of measurements consist of 25 points on the left slope and 25 points on the right slope. In the beginning, the chirp rate of 25 points on each slope are chosen as equally distributed around the chirp rate of the corresponding mid-fringe. The first gravity value is achieved by fitting the data consisting of 50 single measurements. Afterwards, the above chirp rates are repeated. The variation of the gravity is extracted by the shifting of the central fringe after fitting. The

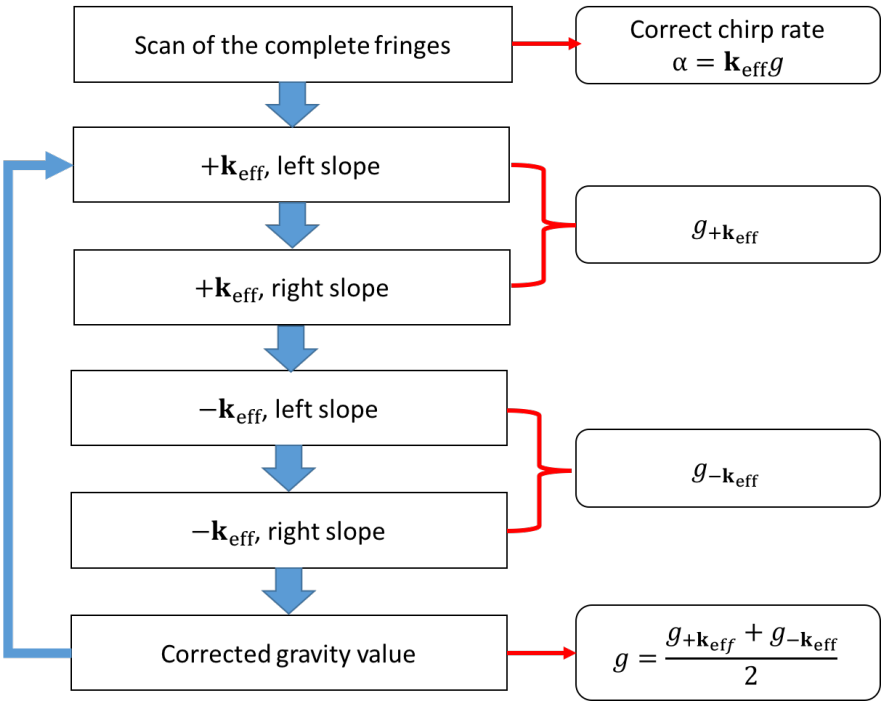

Figure 6.6: Flow chart of the gravity measurement with the scans of two fringes by measurements on the slopes. The final gravity value is the half-difference of the gravity with an normal and the inverting light vectors.

measurement is visualized in Fig. 6.5. In this way, we don't need to scan the entire fringe while preserving maximal sensitivity to phase fluctuations.

(2) Phase shift terms can be sorted based on the dependence of direction of the Raman laser wavevector. For example, the phase shift due to the alignment of Raman laser beams and Coriolis force are wavevector dependent while the AC Stark shift and Zeeman shift are wavevector independent. In the comparison, we operate the above scheme with an normal and the inverting wavevectors $+\mathbf{k}_{eff}$ and $-\mathbf{k}_{eff}$ alternatively. The corresponding phase shifts can be expressed as:

$$\begin{aligned} +\mathbf{k}_{eff} &: \Delta\Phi = k_{eff} g T^2 + \Delta\Phi(indep) + \Delta\Phi(dep) \\ -\mathbf{k}_{eff} &: \Delta\Phi = -k_{eff} g T^2 + \Delta\Phi(indep) - \Delta\Phi(dep) \end{aligned} \tag{6.1}$$

Half-difference of these phase shifts makes it possible to eliminate the term $\Delta\Phi$(indep). Finally each gravity value is calculated with up to 100 runs for the scans of two fringes by measurements on the slopes. The flow chart is shown in Fig.6.6. In our experiment, the operation rate of single measurement is 0.5 Hz. In principle, gravity measurement with above protocol requires 200 s for each data point for g.

6.2.2 Campaign Scheme

There will be five gravimeters involved in the comparison, which are two FG5, two CG5 and our atom interferometry gravimeter (AI gravimeter). Figure 6.7 shows the locations of each devices in the comparison room, which is under the ground. During the measurement, the AI gravimeter will output one gravity value every 4 mins. As a reference, we will also set the FG5 at the same operation rate, performing 1 drop every 4 mins. Furthermore, a trigger signal will be sent to both the AI gravimeter and FG5 for synchronization in the beginning of each single gravity measurement. In the mean while, the relative graivmeter CG5 will perform a measurement at a rate of 6 Hz, which contributes to supervise the transitory gravity anomaly. Another role of CG5 is that it will be used to measure the vertical gravity gradients. The gravity value measured with FG5 is given at a height of 122 cm while the AI gravimeter performs gravity measurement 100 cm above the ground. For the final comparison results, the gravity values will be given at the height of 111 cm above ground, which is the mean height of the absolute gravimeters. The transfer of g is calculated from the measured vertical gravity gradients by CG5 [37].

Due to the different rates of these devices, we can compare the short-term and long-term stability of our AI gravimeter. Although CG5 only measures the gravity variation relatively, it has high sensitivity and resolution. In the AI gravimeter, each gravity value is the result of a average over 60 points. In fact, after fitting the data, we can also calculate the gravity value at each point backward. In this way, we achieve a gravity measure at rate 0.5 Hz. Compare with the outputs of CG5, the short-term fluctuation of the AI gravimeter can be evaluated. On the other hand, the two kind of absolute gravimeters, FG5 and AI gravimeter, continuously perform at the same rate. Thus the long-term stability as well as the gravity accuracy of the AI gravimeter can be determined.

6.2.3 Normalized Detection Scheme

The above comparison campaign requires the long-time stability of the device. In the previous experiment, the gravity is measured by single state detection, which only probes the atoms number in the state $|F = 2\rangle$. In this method, the variation of the fluorescence signal is treated as the variation of the transition probability in state $|F = 2\rangle$. This is feasible due to the fluctuation of the total atom number in short time is neglected. However, due to the changes of environmental temperature, laser intensity, laser frequency, etc., the number of atoms fluctuates randomly and may drift in long time. Thus with single state detection, the atom number fluctuation contributes to the amplitude noise in interference signal. In order to overcome this problem, we need to detect the proportion of atoms in each hyperfine ground state after the interference process, which

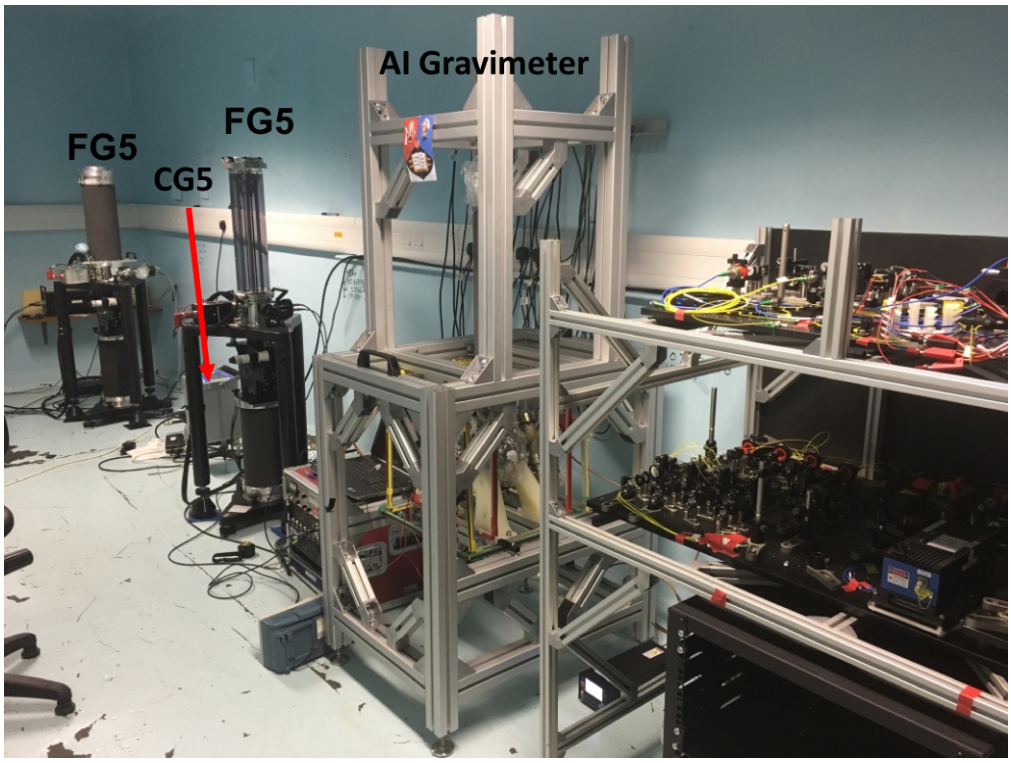

Figure 6.7: The locations of the gravimeters in the comparison room.

is independent of total atom number. A normalization detection is required before the comparison starts.

6.3 Summary

In this chapter, we have discussed the package and transport of our experiment for the comparison campaign. In order to avoid any damage or random tilting on the way, the aluminium frame to support the sensor head and optics were redesigned with higher mechanical stability and better transportability. The system has been settled in the comparison site and is under optimisation. The measurement protocols have been considered at first for preparing for the comparison.

CHAPTER 7

CONCLUSION AND OUTLOOK

7.1 Conclusion

This thesis presents the construction of an absolute gravimeter to act as a metrology reference based on atom interferometry with laser-coolded ^{87}Rb atoms. The set-up realizes an atomic fountain to launch 5×10^6 atoms at a temperature of 10 μK up to 0.4 m above the MOT centre. Higher launching is possible while the launching efficiency is limited by the beam size of the cooling laser. In order to overcome the polarisation issue in the fibre delivery system, free space optics were built to generate all the frequencies required for atom cooling, trapping and detection. After set-up of the atomic fountain, the clouds of atoms were used for gravity measurement with a Mach-Zehnder type atom interferometer. With the additions of magnetic shields, quantisation coils and a vibration isolation platform, the setup reaches a short-term sensitivity of 225 μGal/$\sqrt{\text{Hz}}$, which was limited by the vibration noise in the lab. After 300 s integration, the resolution was improved to 15 μGal. The systemic errors were also analysed. The preliminary accuracy was estimated of 218 μGal, which was limited by the Coriolis effect. These characterisations are not the ultimate performance and still require further optimisation. The improving is still carrying on whilst writing the thesis.

One of the highlights of this thesis is the demonstration of an IQ modulator based optical single-sideband (OSSB) laser system for atom interferometry. The suppression of the unwanted sidebands eliminates the spatial interference due to multiple Raman transitions. Therefore the Rabi frequency and fringe contrast maintain spatially stable. Raman laser beams generated by this technique are phase coherent, which contributes to improve the sensitivity of gravimeter. In addition, this technique cancels the spatially dependent interferometric phase shift, which reduces the errors in the absolute gravity measurement. We also demonstrated the carrier-suppressed single-sideband system, which is proposed as an agile optical frequency shifter.

Since all the components are fibre-coupled devices developed in telecommunication industry, the integration and robustness of the laser system make it promising for the transportable cold-atoms based sensors. A patent of optical frequency manipulation based on the OSSB technique has been filed (application number: GB1712072.6), which paves the way towards future application and exploitation.

Finally the entire experiment was packed and transported to the NERC Space Geodesy Facility in Herstmonceux. A gravimeter comparison campaign against FG5 and CG5 is in preparation. A higher sensitivity is expected from the atom interferometry gravimeter compared to the laboratory because of the lower vibration noise in the comparison site. The explicit accuracy will be determined after the comparison with FG5.

7.2 Outlook

The aim of the project is to build a high precision absolute gravimeter as a reference platform, the key specifications of which are the sensitivity and accuracy. Due to the time constraints of the PhD study, several possible improvements have not yet been implemented. I leave them as the prospects to advance the overall experiment in the future.

(1) Higher atom number and lower atomic temperature are desired to improve the signal-to-noise ratio of the interferometer fringe. To achieve higher loading rate, the system design includes a 2D-MOT and this needs to be implemented. The cooling performance with the current atomic fountain setup is limited by cooling laser power and beam size. Atoms can not be cooled and launched efficiently, resulting in quite a lot of atoms being lost along the path, especially at high launch velocity. To overcome this problem, enlarging the window size on the MOT chamber will be a solution. In addition, some interesting schemes can also be used to promote the cooling. For example, 1D Raman cooling can be employed to reduce the vertical temperature [147], or clouds constrained inside a dipole trap can reduce the ballistic expansion of the atomic cloud [148]. These schemes are also feasible without making significant changes to the current setup.

(2) The performance of the OSSB based laser system needs to be examined in detail. Although we also employed this laser system to perform atom interferometry, its effects on the sensitivity and accuracy of the gravity measurement are still a question. So far we noticed that the RF driving signal has a frequency-dependent phase shift, which is due to the group delay of the RF devices and the interference effect suffering from the back reflection of RF signal. This problem not only may cause unwanted sidebands but also alters the OPR of the +1st order sideband to carrier when we scanning the chirp rate in the atom interferometer sequence. Fortunately we can calculate precisely the induced the AC stark shift to operate a post-correction. We also can think about a programmable phase shifter to compensate this effect.

(3) As we present in chapter 4, the OSSB based laser system also can work as an agile optical frequency shifter. Thus a single laser to produce all the frequencies for the atom interferometer can be built. In addition, all the components are fibre devices from telecommunication industry. Thus the laser system will be much more compact, low cost and robust. But the polarisation in such fibre delivery system needs to be checked. Carefully splicing can avoid this risk [79].

(4) Some active control schemes are required. The primary phase noise in our experiment is contributed by the vibration noise. To isolate the vibration further, an active vibration isolator with lower resonance frequency is desired [146]. Others like the Raman laser power and apparatus tilting also need to be monitored and actively controlled [80].

(5) Improvements in the detection scheme towards the shot noise detection limit could be achieved by the simultaneous detection of the two ground states [149]. A cloud suspending technique is required to increase the spatial separation of the atoms in each state.

(6) Systemic errors needs to be learned in more detail. Currently we have only examined leading order systematic errors, and will assess additional terms as sensitivity and biases improve. For example, in high accuracy gravimeters, the systemic errors such as the wavefront aberration, gravity gradient, timing errors etc. need to be calculated precisely.

APPENDIX A

RUBIDIUM INFORMATION

Table A.1: ^{87}Rb properties including the D_2 ($5^2S_{1/2} \rightarrow 5^2P_{3/2}$) transition optical properties. Cited from [84].

Property	Symbol	Value
Atomic Number	Z	37
Atomic Mass	m	$1.443\ 160\ 60(11)\times10^{-25}$ kg
Wavelength (Vacuum)	λ	780.241 209 686(13) nm
Wave Numer (Vacuum)	$k_L/2\pi$	12 816.549 389 93(21) cm^{-1}
Lifetime	τ	26.24(4) ns
Decay Rate/Natural Line Width (FWHM)	Γ	38.11(6) $\times10^6$ $s^{-1}/2\pi\cdot$ 6.065(9) MHz
Recoil Velocity	v_r	5.8845 mm/s
Recoil Energy	ω_r	$2\pi\cdot$3.7710 kHz
Recoil Temperature	T_r	361.96 nK
Doppler Shift ($v_{atom} = v_r$)	$\Delta\omega_d(v_{atom} = v_r)$	$2\pi\cdot$7.5419 kHz
Doppler Temperature	T_D	146 μK
Clock transition Zeeman shift	$\Delta\omega_{clock}/B^2$	$2\pi\cdot$575.15 Hz/G^2
D_2 transition dipole matrix element	$\langle J = 1/2 \vert\vert er \vert\vert J^{'} = 3/2\rangle$	$3.584(4)\times10^{-29}$ C·m
Saturation Intensity ($\vert F = 2, m_F = \pm2\rangle \rightarrow \vert F^{'} = 3, m_F^{'} = \pm3\rangle$) (isotropic light polarisation)	I_{sat}	1.669(2) mW/cm^2

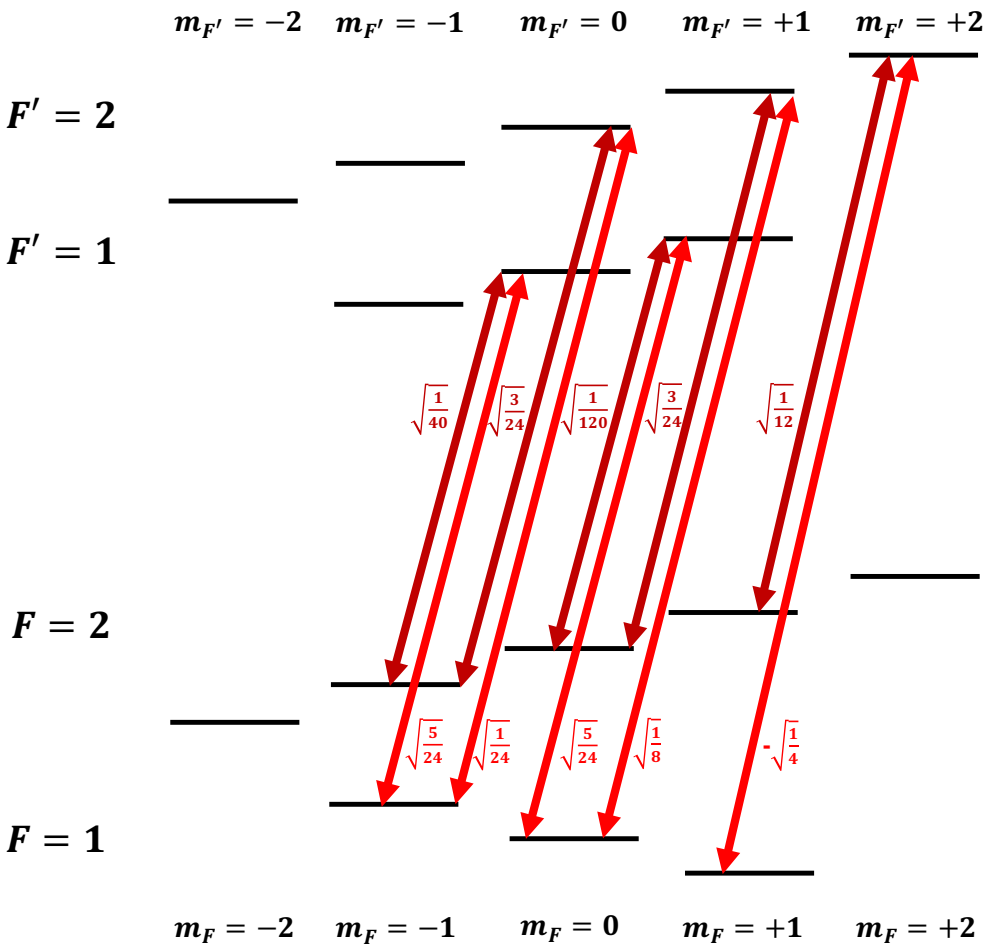

Figure A.1: Two-photon $\sigma^+ - \sigma^+$ transition between magnetic sublevels of $F = 1$ and $F = 2$ in ^{87}Rb D_2 transition. Multiples of dipole matrix elements $\langle J = 1/2||er||J' = 3/2\rangle$ are indicated. Modified from [123].

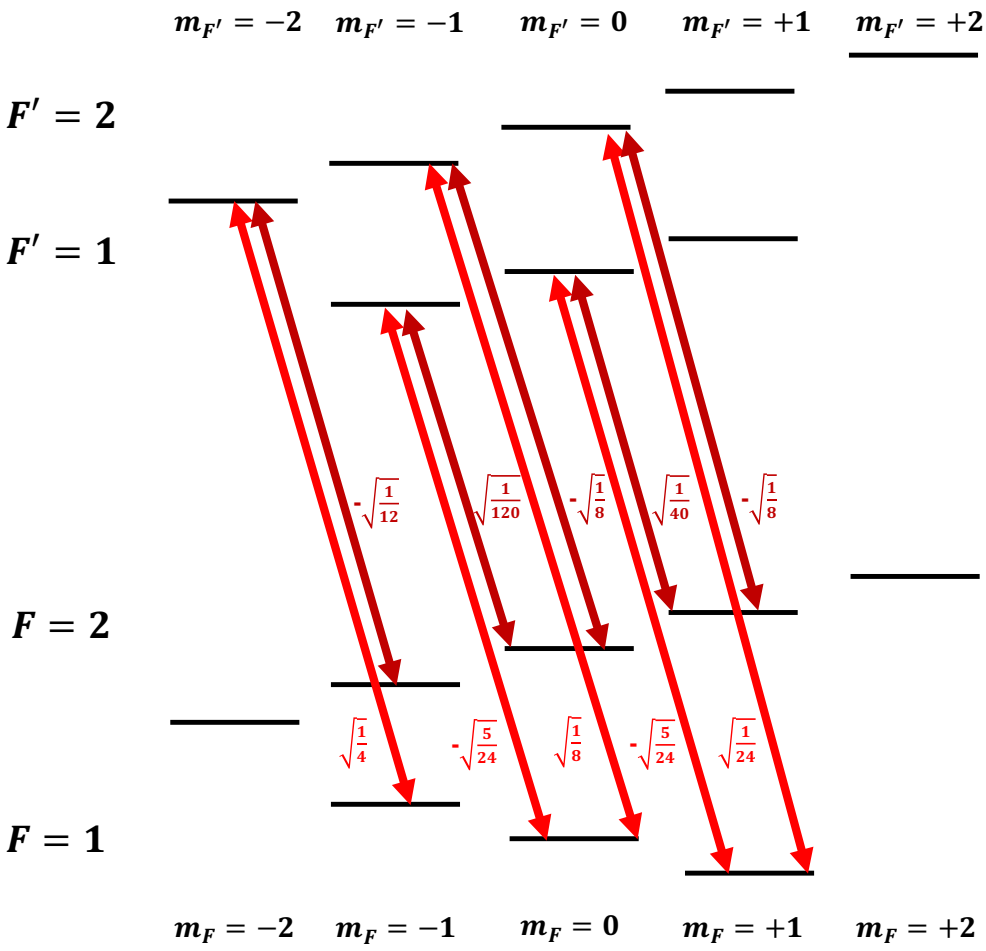

Figure A.2: Two-photon $\sigma^- - \sigma^-$ transition between magnetic sublevels of $F = 1$ and $F = 2$ in ^{87}Rb D_2 transition. Multiples of dipole matrix elements $\langle J = 1/2||er||J' = 3/2\rangle$ are indicated. Modified from [123].

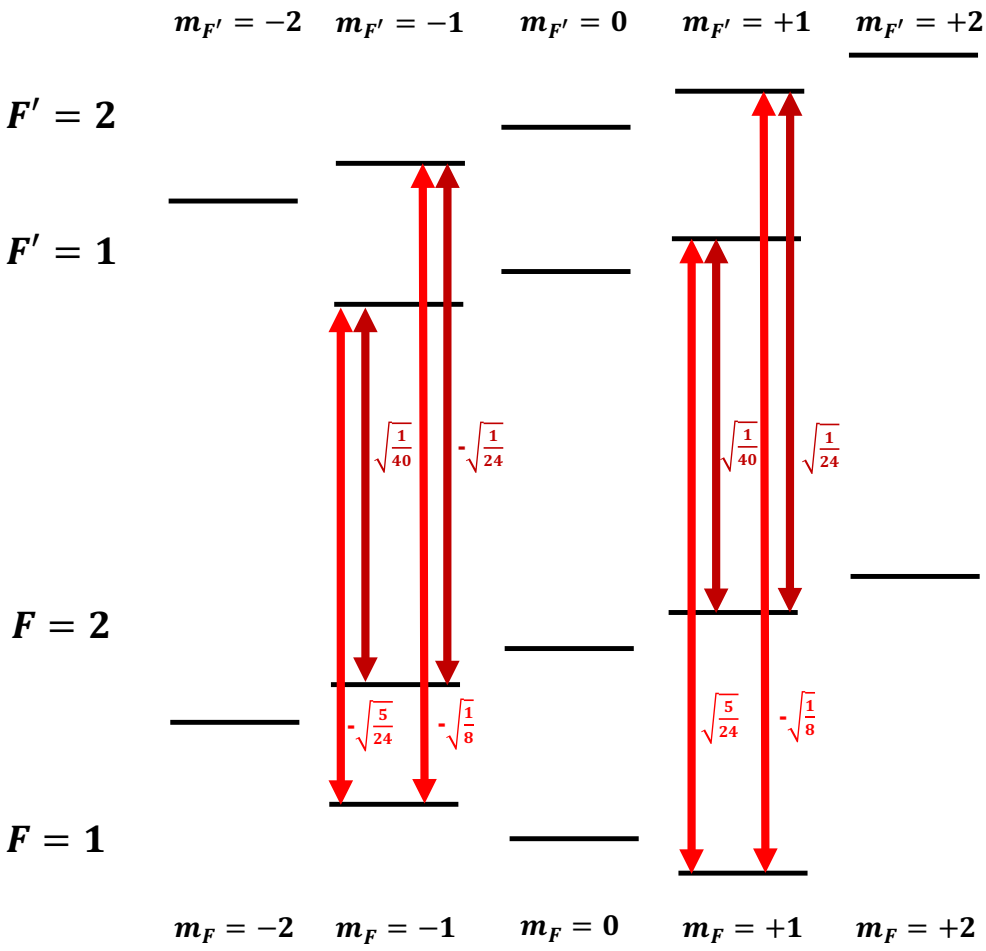

Figure A.3: Two-photon $\pi - \pi$ transition between magnetic sublevels of $F = 1$ and $F = 2$ in ^{87}Rb D_2 transition. Multiples of dipole matrix elements $\langle J = 1/2||er||J^{'} = 3/2\rangle$ are indicated. Modified from [123].

LIST OF REFERENCES

[1] *The Apollo 15 Hammer-Feather Drop.* https://nssdc.gsfc.nasa.gov/planetary/lunar/apollo_15_feather_drop.html.

[2] **LIGO Scientific Collaboration and Virgo Collaboration** Collaboration, B. P. Abbott et al., *Observation of Gravitational Waves from a Binary Black Hole Merger*, Phys. Rev. Lett. **116** 061102 (2016).

[3] W. J. Hinze, R. R. Von Frese and A. H. Saad, *Gravity and magnetic exploration: Principles, practices, and applications.* Cambridge University Press (2013).

[4] W. Torge, *Gravimetry*, Geodetic Activities Performed During the Period 1975-1978 (1979).

[5] R. Rummel, *Geoid and Gravity in Earth Sciences – An Overview*, Earth, Moon, and Planets **94** (1), 3–11 (2004).

[6] I. Marson, *A short walk along the gravimeters path*, International Journal of Geophysics **2012** (2012).

[7] I. Marson and J. E. Faller, *g-the acceleration of gravity: its measurement and its importance*, Journal of Physics E: Scientific Instruments **19** (1), 22 (1986).

[8] L. J. LaCoste Jr, *A new type long period vertical seismograph*, Physics **5** (7), 178–180 (1934).

[9] *gPhoneX Gravity Meter Webpage.* http://microglacoste.com/product/gphonex-gravimeter/.

[10] *CG5 Relative Gravimeter Webpage.* http://scintrexltd.com/product/cg-6-autograv-gravity-meter/.

[11] J. M. Goodkind, *The superconducting gravimeter*, Review of scientific instruments **70** (11), 4131–4152 (1999).

[12] W. Prothero Jr and J. Goodkind, *A superconducting gravimeter*, Review of Scientific Instruments **39** (9), 1257–1262 (1968).

[13] U. Riccardi, S. Rosat and J. Hinderer, *On the Accuracy of the Calibration of Superconducting Gravimeters Using Absolute and Spring Sensors: a Critical Comparison*, Pure and Applied Geophysics **169** (8), 1343–1356 (2012).

[14] S. Okubo, S. Yoshida, T. Sato, Y. Tamura and Y. Imanishi, *Verifying the precision of a new generation absolute gravimeter FG5Comparison with superconducting gravimeters and detection of oceanic loading tide*, Geophysical research letters **24** (4), 489–492 (1997).

[15] U. Riccardi, S. Rosat and J. Hinderer, *Comparison of the Micro-g LaCoste gPhone-054 spring gravimeter and the GWR-C026 superconducting gravimeter in Strasbourg (France) using a 300-day time series*, Metrologia **48** (1), 28 (2011).

[16] R. Middlemiss, A. Samarelli, D. Paul, J. Hough, S. Rowan and G. Hammond, *Measurement of the Earth tides with a MEMS gravimeter*, Nature **531** (7596), 614–617 (2016).

[17] *CG5 Brochure*. `http://www.allied-associates.co.uk/wp-content/uploads/2016/06/Scintrex_CG5-DIGITAL-Brochure-R1.pdf`.

[18] *The gPhoneX gravity meter Brochure*.
`http://www.microglacoste.com/pdf/Brochure-gPhoneX.pdf`.

[19] *iGrav Superconducting Gravity Meter Brochure*.
`http://www.gwrinstruments.com/pdf/igrav-brochure.pdf`.

[20] J. E. Faller and I. Marson, *Ballistic Methods of Measuring g - the Direct Free-Fall and Symmetrical Rise-and-Fall Methods Compared*, Metrologia **25** (1), 49 (1988).

[21] *FG5 Absolute Gravimeter Webpage*. `http://www.microglacoste.com/fg5.php`.

[22] M. Van Camp, T. Camelbeeck and P. Richard, *The FG5 absolute gravimeter: metrology and geophysics*, Physicalia Magazine, Journal of the Belgian Society **25** (3), 161–174 (2003).

[23] T. M. Niebauer, G. S. Sasagawa, J. E. Faller, R. Hilt and F. Klopping, *A new generation of absolute gravimeters*, Metrologia **32** (3), 159 (1995).

[24] A. Germak, S. Desogus and C. Origlia, *Interferometer for the IMGC rise-and-fall absolute gravimeter*, Metrologia **39** (5), 471 (2002).

[25] A. Peters, K. Y. Chung and S. Chu, *High-precision gravity measurements using atom interferometry*, Metrologia **38** (1), 25 (2001).

[26] M. Kasevich and S. Chu, *Measurement of the gravitational acceleration of an atom with a light-pulse atom interferometer*, Applied Physics B **54** (5), 321–332 (1992).

[27] T. M. Niebauer, G. S. Sasagawa, J. E. Faller, R. Hilt and F. Klopping, *A new generation of absolute gravimeters*, Metrologia **32** (3), 159 (1995).

[28] *A10 Absolute Gravimeter Webpage*. `http://www.microglacoste.com/a10.php`.

[29] *AQG Absolute Gravimeter Webpage*. `https://www.muquans.com/index.php/products/aqg`.

[30] P. R. Berman, *Atom interferometry*. Academic press (1997).

[31] K. P. Zetie, S. F. Adams and R. M. Tocknell, *How does a Mach-Zehnder interferometer work?*, Physics Education **35** (1), 46 (2000).

[32] G. Lamporesi, A. Bertoldi, L. Cacciapuoti, M. Prevedelli and G. M. Tino, *Determination of the Newtonian gravitational constant using atom interferometry*, Physical review letters **100** (5), 050801 (2008).

[33] M. O. Scully and J. P. Dowling, *Quantum-noise limits to matter-wave interferometry*, Phys. Rev. A **48** 3186–3190 (1993).

[34] Z.-K. Hu, B.-L. Sun, X.-C. Duan, M.-K. Zhou, L.-L. Chen, S. Zhan, Q.-Z. Zhang and J. Luo, *Demonstration of an ultrahigh-sensitivity atom-interferometry absolute gravimeter*, Phys. Rev. A **88** 043610 (2013).

[35] H. Müller, S.-w. Chiow, S. Herrmann, S. Chu and K.-Y. Chung, *Atom-Interferometry Tests of the Isotropy of Post-Newtonian Gravity*, Phys. Rev. Lett. **100** 031101 (2008).

[36] T. Farah, A. Clairon, A. Landragin, S. Merlet, F. P. D. Santo and A. Louchet-Chauvet, *Continuous g monitoring with atom interferometry*, in *2011 Joint Conference of the IEEE International Frequency Control and the European Frequency and Time Forum (FCS) Proceedings*, 1–4 (2011).

[37] A. Louchet-Chauvet, S. Merlet, Q. Bodart, A. Landragin, F. P. D. Santos, H. Baumann, G. D'Agostino and C. Origlia, *Comparison of 3 Absolute Gravimeters Based on Different Methods for the e-MASS Project*, IEEE Transactions on Instrumentation and Measurement **60** (7), 2527–2532 (2011).

[38] Y. Bidel, O. Carraz, R. Charrire, M. Cadoret, N. Zahzam and A. Bresson, *Compact cold atom gravimeter for field applications*, Applied Physics Letters **102** (14), 144107 (2013).

[39] P. A. Altin et al., *Precision atomic gravimeter based on Bragg diffraction*, New Journal of Physics **15** (2), 023009 (2013).

[40] F. Sorrentino, A. Bertoldi, Q. Bodart, L. Cacciapuoti, M. de Angelis, Y.-H. Lien, M. Prevedelli, G. Rosi and G. M. Tino, *Simultaneous measurement of gravity acceleration and gravity gradient with an atom interferometer*, Applied Physics Letters **101** (11), 114106 (2012).

[41] C. Freier, M. Hauth, V. Schkolnik, B. Leykauf, M. Schilling, H. Wziontek, H.-G. Scherneck, J. Mller and A. Peters, *Mobile quantum gravity sensor with unprecedented stability*, Journal of Physics: Conference Series **723** (1), 012050 (2016).

[42] B. Wu, Z. Wang, B. Cheng, Q. Wang, A. Xu and Q. Lin, *The investigation of a Gal-level cold atom gravimeter for field applications*, Metrologia **51** (5), 452 (2014).

[43] T. Kovachy, P. Asenbaum, C. Overstreet, C. Donnelly, S. Dickerson, A. Sugarbaker, J. Hogan and M. Kasevich, *Quantum superposition at the half-metre scale*, Nature **528** (7583), 530–533 (2015).

[44] L. Zhou, Z. Y. Xiong, W. Yang, B. Tang, W. C. Peng, K. Hao, R. B. Li, M. Liu, J. Wang and M. S. Zhan, *Development of an atom gravimeter and status of the 10-meter atom interferometer for precision gravity measurement*, General Relativity and Gravitation **43** (7), 1931–1942 (2011).

[45] J. Hartwig, S. Abend, C. Schubert, D. Schlippert, H. Ahlers, K. Posso-Trujillo, N. Gaaloul, W. Ertmer and E. M. Rasel, *Testing the universality of free fall with rubidium and ytterbium in a very large baseline atom interferometer*, New Journal of Physics **17** (3), 035011 (2015).

[46] S.-w. Chiow, T. Kovachy, H.-C. Chien and M. A. Kasevich, $102\hbar k$ *Large Area Atom Interferometers*, Phys. Rev. Lett. **107** 130403 (2011).

[47] J. M. McGuirk, M. J. Snadden and M. A. Kasevich, *Large Area Light-Pulse Atom Interferometry*, Phys. Rev. Lett. **85** 4498–4501 (2000).

[48] M. Weitz, B. C. Young and S. Chu, *Atomic Interferometer Based on Adiabatic Population Transfer*, Phys. Rev. Lett. **73** 2563–2566 (1994).

[49] R. Charrière, M. Cadoret, N. Zahzam, Y. Bidel and A. Bresson, *Local gravity measurement with the combination of atom interferometry and Bloch oscillations*, Phys. Rev. A **85** 013639 (2012).

[50] F. Sorrentino et al., *The Space Atom Interferometer project: status and prospects*, Journal of Physics: Conference Series **327** (1), 012050 (2011).

[51] B. Altschul et al., *Quantum tests of the Einstein Equivalence Principle with the STEQUEST space mission*, Advances in Space Research **55** (1), 501 – 524 (2015).

[52] J. Williams, S. wey Chiow, N. Yu and H. Mller, *Quantum test of the equivalence principle and space-time aboard the International Space Station*, New Journal of Physics **18** (2), 025018 (2016).

[53] T. Schuldt et al., *Design of a dual species atom interferometer for space*, Experimental Astronomy **39** (2), 167–206 (2015).

[54] H. Müntinga et al., *Interferometry with Bose-Einstein Condensates in Microgravity*, Phys. Rev. Lett. **110** 093602 (2013).

[55] S. Kulas et al., *Miniaturized Lab System for Future Cold Atom Experiments in Microgravity*, Microgravity Science and Technology **29** (1), 37–48 (2017).

[56] B. Barrett, L. Antoni-Micollier, L. Chichet, B. Battelier, T. Lévèque, A. Landragin and P. Bouyer, *Dual matter-wave inertial sensors in weightlessness*, Nature communications **7** (2016).

[57] *MAIUS 1 First Bose-Einstein condensate generated in space.* `http://www.dlr.de/dlr/en/desktopdefault.aspx/tabid-10081/151_read-20337/#/gallery/25194`.

[58] K. Bongs, R. Launay and M. Kasevich, *High-order inertial phase shifts for time-domain atom interferometers*, Applied Physics B **84** (4), 599–602 (2006).

[59] M. Schmidt, A. Senger, M. Hauth, C. Freier, V. Schkolnik and A. Peters, *A mobile high-precision absolute gravimeter based on atom interferometry*, Gyroscopy and Navigation **2** (3), 170 (2011).

[60] N. Poli, F.-Y. Wang, M. G. Tarallo, A. Alberti, M. Prevedelli and G. M. Tino, *Precision Measurement of Gravity with Cold Atoms in an Optical Lattice and Comparison with a Classical Gravimeter*, Phys. Rev. Lett. **106** 038501 (2011).

[61] A. Hinton et al., *A portable magneto-optical trap with prospects for atom interferometry in civil engineering*, Philosophical Transactions of the Royal Society of London A: Mathematical, Physical and Engineering Sciences **375** (2099), (2017).

[62] *iSense Integrated Quantum Sensors.* `https://www.isense-gravimeter.eu/introduction.html`.

[63] B. Fang et al., *Metrology with Atom Interferometry: Inertial Sensors from Laboratory to Field Applications*, Journal of Physics: Conference Series **723** (1), 012049 (2016).

[64] *Quantum Gravimeter QG-1.* `https://www.iqo.uni-hannover.de/iqo_qg1.html?&L=1`.

[65] M. J. Snadden, J. M. McGuirk, P. Bouyer, K. G. Haritos and M. A. Kasevich, *Measurement of the Earth's Gravity Gradient with an Atom Interferometer-Based Gravity Gradiometer*, Phys. Rev. Lett. **81** 971–974 (1998).

[66] T. L. Gustavson, A. Landragin and M. A. Kasevich, *Rotation sensing with a dual atom-interferometer Sagnac gyroscope*, Classical and Quantum Gravity **17** (12), 2385 (2000).

[67] P. Berg, S. Abend, G. Tackmann, C. Schubert, E. Giese, W. P. Schleich, F. A. Narducci, W. Ertmer and E. M. Rasel, *Composite-Light-Pulse Technique for High-Precision Atom Interferometry*, Phys. Rev. Lett. **114** 063002 (2015).

[68] B. Canuel et al., *Six-Axis Inertial Sensor Using Cold-Atom Interferometry*, Phys. Rev. Lett. **97** 010402 (2006).

[69] B. Barrett, A. Bertoldi and P. Bouyer, *Inertial quantum sensors using light and matter*, Physica Scripta **91** (5), 053006 (2016).

[70] L. A. A. B. E. C. B. F. S. G. R. G. J. H. D. H. A. L. G. L. J. L. N. M. M. P. I. R. P. B. B. Canuel, S. Pelisson, *MIGA: combining laser and matter wave interferometry for mass distribution monitoring and advanced geodesy*, (2016). `http://dx.doi.org/10.1117/12.2228825`.

[71] J. Stuhler, M. Fattori, T. Petelski and G. M. Tino, *MAGIAusing atom interferometry to determine the Newtonian gravitational constant*, Journal of Optics B: Quantum and Semiclassical Optics **5** (2), S75 (2003).

[72] A. Bertoldi, G. Lamporesi, L. Cacciapuoti, M. de Angelis, M. Fattori, T. Petelski, A. Peters, M. Prevedelli, J. Stuhler and G. M. Tino, *Atom interferometry gravity-gradiometer for the determination of the Newtonian gravitational constant G*, The European Physical Journal D - Atomic, Molecular, Optical and Plasma Physics **40** (2), 271–279 (2006).

[73] A. Wicht, J. M. Hensley, E. Sarajlic and S. Chu, *A Preliminary Measurement of the Fine Structure Constant Based on Atom Interferometry*, Physica Scripta **2002** (T102), 82 (2002).

[74] P. Cheinet, F. P. D. Santos, T. Petelski, A. Clairon, N. Dimarcq, D. Holleville and A. Landragin, *Cold Atom Absolute Gravimeter for the Watt Balance*, in *2004 Conference on Precision Electromagnetic Measurements*, 60–61 (2004).

[75] L. Zhou et al., *Test of Equivalence Principle at* 10^{-8} *Level by a Dual-Species Double-Diffraction Raman Atom Interferometer*, Phys. Rev. Lett. **115** 013004 (2015).

[76] J. M. Hogan et al., *An atomic gravitational wave interferometric sensor in low earth orbit (AGIS-LEO)*, General Relativity and Gravitation **43** (7), 1953–2009 (2011).

[77] P. Hamilton, M. Jaffe, P. Haslinger, Q. Simmons, H. Müller and J. Khoury, *Atom-interferometry constraints on dark energy*, Science **349** (6250), 849–851 (2015).

[78] A. Niggebaum, *Towards mobile quantum sensors for gravity surveys.* Ph.D. thesis, University of Birmingham (2016).

[79] A. G. Hinton, *Development of a transportable cold atom gradiometer.* Ph.D. thesis, University of Birmingham (2016).

[80] M. Hauth, *A mobile, high-precision atom-interferometer and its application to gravity observations.* Ph.D. thesis, Humboldt-Universität zu Berlin, Mathematisch-Naturwissenschaftliche Fakultät (2015).

[81] G. Rosi, *Precision gravity measurements with atom interferometry.* Ph.D. thesis, University of Piasa (2013).

[82] N. F. Ramsey, *A Molecular Beam Resonance Method with Separated Oscillating Fields*, Phys. Rev. **78** 695–699 (1950).

[83] M. Schmidt, *A mobile high-precision gravimeter based on atom interferometry*. Ph.D. thesis, Humboldt-Universität zu Berlin, Mathematisch-Naturwissenschaftliche Fakultät I (2011).

[84] D. A. Steck, *Rubidium 87 D line data*, (2001). `http://steck.us/alkalidata/`.

[85] P. Cheinet, B. Canuel, F. P. D. Santos, A. Gauguet, F. Yver-Leduc and A. Landragin, *Measurement of the Sensitivity Function in a Time-Domain Atomic Interferometer*, IEEE Transactions on Instrumentation and Measurement **57** (6), 1141–1148 (2008).

[86] P. Cheinet, *Conception and realisation of a cold atom gravimeter*. Theses, Université Pierre et Marie Curie - Paris VI (2006).

[87] P. Torsten, *Atom Interferometers for Precision Gravity Measurements*. Ph.D. thesis, Ph. D. thesis (University of Florence, 2005) (2005).

[88] C. Freier, *Measurement of local gravity using atom interferometry*, Master's thesis, Diploma thesis, Humboldt-Universität zu Berlin (2010).

[89] E. L. Raab, M. Prentiss, A. Cable, S. Chu and D. E. Pritchard, *Trapping of Neutral Sodium Atoms with Radiation Pressure*, Phys. Rev. Lett. **59** 2631–2634 (1987).

[90] C. J. Foot, *Atomic physics*, vol. 7. Oxford University Press (2005).

[91] P. D. Lett, W. D. Phillips, S. L. Rolston, C. E. Tanner, R. N. Watts and C. I. Westbrook, *Optical molasses*, J. Opt. Soc. Am. B **6** (11), 2084–2107 (1989).

[92] M. A. Kasevich, E. Riis, S. Chu and R. G. DeVoe, *rf spectroscopy in an atomic fountain*, Phys. Rev. Lett. **63** 612–615 (1989).

[93] A. Bertoldi, G. Lamporesi, L. Cacciapuoti, M. de Angelis, M. Fattori, T. Petelski, A. Peters, M. Prevedelli, J. Stuhler and G. M. Tino, *Atom interferometry gravity-gradiometer for the determination of the Newtonian gravitational constant G*, The European Physical Journal D **40** (2), 271–279 (2006).

[94] M. A. Kasevich, *Atom interferometry in an atomic fountain*. Ph.D. thesis (1992).

[95] H. J. Davies, *An optically guided atomic fountain*. Ph.D. thesis, Durham University (1999).

[96] S. ichi Ohshima, T. Kurosu, T. Ikegami and Y. Nakadan, *Cesium Atomic Fountain with Two-Dimensional Moving Molasses*, Japanese Journal of Applied Physics **34** (9A), L1170 (1995).

[97] D. J. McCarron, S. A. King and S. L. Cornish, *Modulation transfer spectroscopy in atomic rubidium*, Measurement Science and Technology **19** (10), 105601 (2008).

[98] V. Singh, V. B. Tiwari, S. R. Mishra and H. S. Rawat, *A tunable Doppler-free dichroic lock for laser frequency stabilization*, Applied Physics B **122** (8), 225 (2016).

[99] E. Rocco, R. N. Palmer, T. Valenzuela, V. Boyer, A. Freise and K. Bongs, *Fluorescence detection at the atom shot noise limit for atom interferometry*, New Journal of Physics **16** (9), 093046 (2014).

[100] K. Dieckmann, R. J. C. Spreeuw, M. Weidemüller and J. T. M. Walraven, *Two-dimensional magneto-optical trap as a source of slow atoms*, Phys. Rev. A **58** 3891–3895 (1998).

[101] R. W. G. Moore, L. A. Lee, E. A. Findlay, L. Torralbo-Campo, G. D. Bruce and D. Cassettari, *Measurement of vacuum pressure with a magneto-optical trap: A pressure-rise method*, Review of Scientific Instruments **86** (9), 093108 (2015).

[102] P. Palittapongarnpim, *Characterization of Magneto-optical Trap For Experiments in Light-Atom Interfacing*. Ph.D. thesis, University of Calgary (2012).

[103] I. Yavin, M. Weel, A. Andreyuk and A. Kumarakrishnan, *A calculation of the time-of-flight distribution of trapped atoms*, American Journal of Physics **70** (2), 149–152 (2002).

[104] G. Santarelli, A. Clairon, S. Lea and G. Tino, *Heterodyne optical phase-locking of extended-cavity semiconductor lasers at 9 GHz*, Optics Communications **104** (4), 339 – 344 (1994).

[105] G. Tackmann, M. Gilowski, C. Schubert, P. Berg, T. Wendrich, W. Ertmer and E. M. Rasel, *Phase-locking of two self-seeded tapered amplifier lasers*, Optics Express **18** (9), 9258 (2010).

[106] M. Schmidt, M. Prevedelli, A. Giorgini, G. M. Tino and A. Peters, *A portable laser system for high-precision atom interferometry experiments*, Applied Physics B **102** (1), 11–18 (2010).

[107] S. H. Yim, S.-B. Lee, T. Y. Kwon and S. E. Park, *Optical phase locking of two extended-cavity diode lasers with ultra-low phase noise for atom interferometry*, Applied Physics B **115** (4), 491–495 (2013).

[108] L. Cacciapuoti, M. de Angelis, M. Fattori, G. Lamporesi, T. Petelski, M. Prevedelli, J. Stuhler and G. M. Tino, *Analog + digital phase and frequency detector for phase locking of diode lasers*, Review of Scientific Instruments **76** (5), 053111 (2005).

[109] P. Bouyer, T. L. Gustavson, K. G. Haritos and M. A. Kasevich, *Microwave signal generation with optical injection locking*, Optics Letters **21** (18), 1502 (1996).

[110] O. Carraz, R. Charrière, M. Cadoret, N. Zahzam, Y. Bidel and A. Bresson, *Phase shift in an atom interferometer induced by the additional laser lines of a Raman laser generated by modulation*, Phys. Rev. A **86** 033605 (2012).

[111] W. Li, X. Pan, N. Song, X. Xu and X. Lu, *A phase-locked laser system based on double direct modulation technique for atom interferometry*, Applied Physics B **123** (2), 54 (2017).

[112] *MXIQ-LN-40: Low Loss Dual Parallel Mach Zehnder Modulator.* `www.hikari-trading.com/opt/photline/file/mxiq_ln_40.pdf`.

[113] M. Izutsu, S. Shikama and T. Sueta, *Integrated optical SSB modulator/frequency shifter*, IEEE Journal of Quantum Electronics **17** (11), 2225–2227 (1981).

[114] S. Shimotsu, S. Oikawa, T. Saitou, N. Mitsugi, K. Kubodera, T. Kawanishi and M. Izutsu, *Single side-band modulation performance of a LiNbO3 integrated modulator consisting of four-phase modulator waveguides*, IEEE Photonics Technology Letters **13** (4), 364–366 (2001).

[115] M. Xue, S. Pan and Y. Zhao, *Optical Single-Sideband Modulation Based on a Dual-Drive MZM and a 120 Hybrid Coupler*, Journal of Lightwave Technology **32** (19), 3317–3323 (2014).

[116] R. W. Boyd, *Nonlinear optics.* Academic press (2003).

[117] R. C. Cumming, *The Serrodyne Frequency Translator*, Proceedings of the IRE **45** (2), 175–186 (1957).

[118] D. M. S. Johnson, J. M. Hogan, S. w. Chiow and M. A. Kasevich, *Broadband optical serrodyne frequency shifting*, Opt. Lett. **35** (5), 745–747 (2010).

[119] F. Theron, O. Carraz, G. Renon, N. Zahzam, Y. Bidel, M. Cadoret and A. Bresson, *Narrow linewidth single laser source system for onboard atom interferometry*, Applied Physics B **118** (1), 1–5 (2015).

[120] C. V. Rammeloo, *Optimisation of a Compact Cold-Atoms Interferometer for Gravimetry.* Ph.D. thesis, University of Birmingham (2017).

[121] *BM-10 Bench Top Vibration Isolation Platform.* `http://www.minusk.com/products/bm10-small-vibration-isolation-platforms.html`.

[122] N. Arias, V. Abediyeh, S. Hamzeloui and E. Gomez, *Low phase noise beams for Raman transitions with a phase modulator and a highly birefringent crystal*, Optics Express **25** (5), 5290 (2017).

[123] T. G. Petelski, *Atom interferometers for precision gravity measurements.* Ph.D. thesis, Paris 6 (2005).

[124] M. Kasevich, D. S. Weiss, E. Riis, K. Moler, S. Kasapi and S. Chu, *Atomic velocity selection using stimulated Raman transitions*, Physical Review Letters **66** (18), 2297–2300 (1991).

[125] G. Biedermann, *Gravity tests, differential accelerometry and interleaved clocks with cold atom interferometers.* Ph.D. thesis, Stanford University (2008).

[126] K. Takase, *Precision rotation rate measurements with a mobile atom interferometer*. Ph.D. thesis, Stanford University (2008).

[127] I. BiPM, I. IFCC, I. ISO and O. IUPAP, *International vocabulary of metrology–basic and general concepts and associated terms, 2008*, JCGM **200** 99–12 (2008).

[128] C. Croarkin, P. Tobias and C. Zey, *Engineering statistics handbook*. NIST iTL (2002).

[129] M. Hauth, C. Freier, V. Schkolnik, A. Senger, M. Schmidt and A. Peters, *First gravity measurements using the mobile atom interferometer GAIN*, Applied Physics B **113** (1), 49–55 (2013).

[130] N. Malossi, Q. Bodart, S. Merlet, T. Lévèque, A. Landragin and F. P. D. Santos, *Double diffraction in an atomic gravimeter*, Phys. Rev. A **81** 013617 (2010).

[131] J. L. Gout, T. Mehlstubler, J. Kim, S. Merlet, A. Clairon, A. Landragin and F. P. D. Santos, *Limits to the sensitivity of a low noise compact atomic gravimeter*, Applied Physics B **92** (2), 133–144 (2008).

[132] F. Sorrentino, Q. Bodart, L. Cacciapuoti, Y.-H. Lien, M. Prevedelli, G. Rosi, L. Salvi and G. M. Tino, *Sensitivity limits of a Raman atom interferometer as a gravity gradiometer*, Phys. Rev. A **89** 023607 (2014).

[133] M. A. Lombardi, *Fundamentals of time and frequency*, in *Mechatronics: An Introduction*, 10–1. CRC Press (2005).

[134] D. W. Allan, *Statistics of atomic frequency standards*, Proceedings of the IEEE **54** (2), 221–230 (1966).

[135] W. Riley, *Handbook of Frequency*. NIST (2008).

[136] W. M. Itano, J. C. Bergquist, J. J. Bollinger, J. M. Gilligan, D. J. Heinzen, F. L. Moore, M. G. Raizen and D. J. Wineland, *Quantum projection noise: Population fluctuations in two-level systems*, Physical Review A **47** (5), 3554–3570 (1993).

[137] M. Fox, *Quantum optics: an introduction*, vol. 15. OUP Oxford (2006).

[138] *N9030B PXA X-Series Signal Analyzer-Data Sheet*. `https://www.keysight.com/main/home.jspx?cc=US&lc=eng`.

[139] Q.-Q. Hu, C. Freier, B. Leykauf, V. Schkolnik, J. Yang, M. Krutzik and A. Peters, *Mapping the absolute magnetic field and evaluating the quadratic Zeeman-effect-induced systematic error in an atom interferometer gravimeter*, Phys. Rev. A **96** 033414 (2017).

[140] A. Gauguet, *Cold atoms gyroscope: limits on the stability and the accuracy due to the atomic beam splitters*. Theses, Université Pierre et Marie Curie - Paris VI (2008).

[141] A. Gauguet, T. E. Mehlstäubler, T. Lévèque, J. Le Gouët, W. Chaibi, B. Canuel, A. Clairon, F. P. Dos Santos and A. Landragin, *Off-resonant Raman transition impact in an atom interferometer*, Phys. Rev. A **78** 043615 (2008).

[142] S.-Y. Lan, P.-C. Kuan, B. Estey, P. Haslinger and H. Müller, *Influence of the Coriolis Force in Atom Interferometry*, Phys. Rev. Lett. **108** 090402 (2012).

[143] J. Zhou, C. Hwang, H. Sun, J. Xu, W. Zhang, R. Kao and T.-C. Cheng, *Precise determination of ocean tide loading gravity effect for absolute gravity stations in coastal area of China: Effects of landsea boundary and station coordinate*, Journal of Geodynamics **68** 29 – 36 (2013).

[144] J. B. Merriam, *Atmospheric pressure and gravity*, Geophysical Journal International **109** (3), 488–500 (1992).

[145] H. Seigel, I. Brcic and P. Mistry, *A guide to high precision land gravimeter surveys*, Scintrex Limited **222** (1995).

[146] M.-K. Zhou, Z.-K. Hu, X.-C. Duan, B.-L. Sun, L.-L. Chen, Q.-Z. Zhang and J. Luo, *Performance of a cold-atom gravimeter with an active vibration isolator*, Phys. Rev. A **86** 043630 (2012).

[147] J. Reichel, O. Morice, G. M. Tino and C. Salomon, *Subrecoil Raman Cooling of Cesium Atoms*, EPL (Europhysics Letters) **28** (7), 477 (1994).

[148] T. Bienaimé, G. Barontini, L. M. de Lépinay, L. Bellando, J. Chabé and R. Kaiser, *Fast compression of a cold atomic cloud using a blue-detuned crossed dipole trap*, Phys. Rev. A **86** 053412 (2012).

[149] G. W. Biedermann, X. Wu, L. Deslauriers, K. Takase and M. A. Kasevich, *Low-noise simultaneous fluorescence detection of two atomic states*, Opt. Lett. **34** (3), 347–349 (2009).